Imperfections: using defects to program designer matter

Meeussen, A.S.

5. Reshapeable groovy sheets

Abstract

Shape-morphing materials find applications in many areas of our lives, from controlled-drag surfaces to pop-up tents. However, designing them poses a challenge. We introduce a novel platform: thin materials with parallel undulations, or *groovy sheets*. Groovy sheets snap quickly and reversibly between multiple stable shapes under external manipulation. We show that individual snap-through events in each groove produce defects that lie at the heart of the sheets' elastic shape-morphing. Adjacent defects show short-range attraction which favours their alignment into chains, or scars, of defects. Scar lines have the ability to change the sheet's equilibrium shape; we show that these shapes fall into distinct categories, depending on the internal configuration of scar lines. Finally, we show that scarred sheets can be modelled as ruled surfaces, whose elastic behaviour can be captured by simple mean-field models. Our work provides the groundwork for using corrugated sheets to design and model shape-morphing materials.

5.1. Introduction

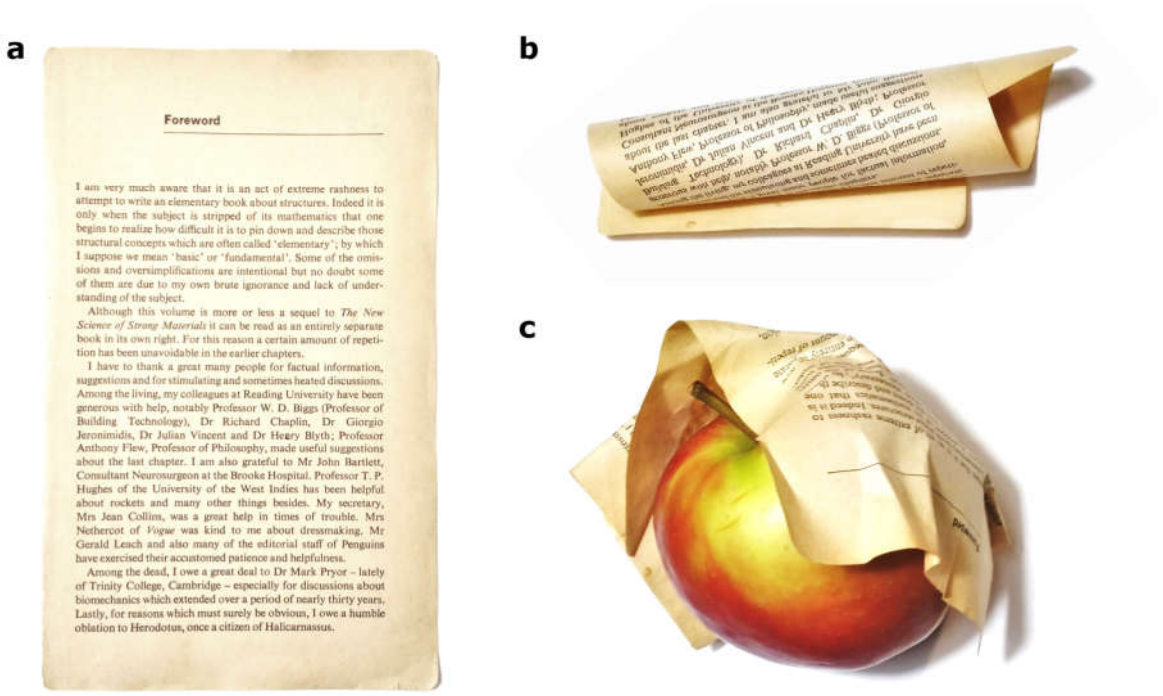

Fig. 5.1.: Thin structures reshape easily. a, A typical thin sheet: a book page, around the thickness of a human hair. **b,** The page bends and rolls smoothly, at low energy cost. **c,** Under the wrong conditions, the sheet crumples: there is no smooth way to wrap the sheet around a spherical apple. As a result, local stretching in the form of folding, dimpling and buckling takes over.

From unfurling leaves and snapping fly-traps to bendy straws and folded maps: shape-shifting materials, both natural and man-made, are useful and all around us. However, inventing, designing, and modelling reshapeable materials is challenging. In this chapter, we propose a novel approach: we make, measure, and model shape-morphing structures made from thin, corrugated, *groovy sheets*.

Why thin sheets? Because they deform easily[21]- think of crumpled paper[98–102], budding leaves[103,104], origami, and kirigami[8,46,64–66,105–107]. This makes them prime candidates to create materials that can deform from one shape to another. The reason behind a thin sheet's deformability (illustrated in Fig. 5.1a) is its dimensional contrast: it is much thinner than it is wide. This has mechanical consequences. Generally, sheets deform in two ways: they either *bend* or *stretch*[108]. Bending is easy to do, because the material's bending stiffness scales with the cube of its thickness (Fig. 5.1b). The thinner the sheet, the better it bends. On the other hand, the stretching stiffness scales linearly with how thick the material is, so stretching is hard. This is why rolling up a piece of paper is much easier than crumpling: crumples involve local stretching (focussed in patches, minimizing the energy cost) to create folds, bumps, and corners.

Thus, thin sheets do not just deform easily, but *interestingly*. Imagine wrapping a flat sheet around a sphere (Fig. 5.1c): it can't be done without crumpling. In spite of its cost, stretching is sometimes preferred over bending. Gauss' *Theorema Egregium* [108, 109] gives an intuitive explanation for this interesting behaviour. From his mathematical

point of view, the shape of a sheet can be described with two types of curvatures: mean (which measures how much a sheet bends), and Gaussian (which measures whether or not the sheet is intrinsically flat). Loosely, bending and stretching deformations correspond to changes in mean and Gaussian curvature respectively. Thus, there is a local competition between stretching and bending deformations, mediated by the sheet's curvature. Bending and stretching are geometrically coupled[110].

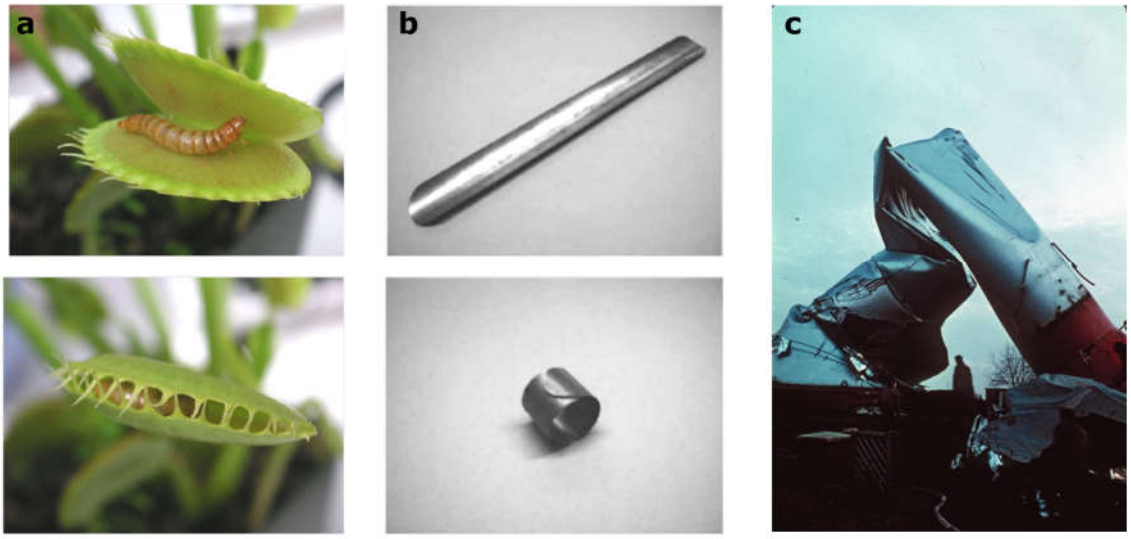

Fig. 5.2.: Thin structures can be multistable. **a,** Examples from the natural world: a Venus flytrap's leaves snap shut around its next meal. Image: Beatrice Murch (CC BY-SA 2.0). **b,** Man-made tape springs snap from straight to rolled. Image adapted from Ref. [111]. **c,** Unintentional bistability in a buckled water tank. Image: D. and W.D. Bushnell, shellbuckling.com (CC BY-NC-ND 3.0).

In short: thin sheets deform easily and interestingly. Both these features are hallmarks of the *geometric nonlinearity* that thin sheets naturally produce. And it is precisely such nonlinearity that allows structures to take on multiple stable shapes[112]. Consider the mechanical point of view: most structures live at rest, in a mechanical equilibrium. When left alone, they stay right where they are. Their elastic energy is at a local minimum. In order to create a shape-morphing material, the structure's energetic landscape (or, formally, its internal energy as a function of its configuration) must have multiple local minima. One way of getting multiple energetic wells is by ensuring that structural strains (deformations relative to the resting shape) depend non-linearly on the structure's internal configuration. Such geometric nonlinearity arises naturally in thin sheets[108,109], in two ways. First, they bend easily, and finite bending is nonlinear; and second, the geometry-mediated competition arises between stretching and bending leads to complex higher-order effects. In other words: thin sheets with surface patterns are good candidates for designing multistable materials[113–119], which has been recognized and researched both in natural[120–122] and man-made systems[12,65,123–128].

Unfortunately, nonlinear reshaping behaviour in thin structures is challenging to model[129–133]. Phenomena that we understand intuitively, from twisting ribbons[134–136] and poking volleyballs[137,138], to wrinkling skin[139] and fabric[140,141], are not easy to capture and predict with simple theories. Many innovations in the field of shape-morphing structures deal

with this issue by drawing inspiration from nature[4,104,142–144] (Fig. 5.2a), or focussing on easier-to-model small[111] or discrete systems, such as origami[39,105,106,145,146] (Fig. 5.2b). In addition, instabilities are traditionally seen as failure modes (a fair point for grain silos and aeroplane cabins), and engineering research is focussed on preventing[147] rather than using them (Fig. 5.2c).

In this work, we propose to harness rather than avoid the instabilities that naturally occur in thin sheets. We aim to create materials that can shape-shift in a robust, reversible, and fast way. To that end, we use thin sheets with a special corrugated geometry: *reshapeable groovy sheets*.

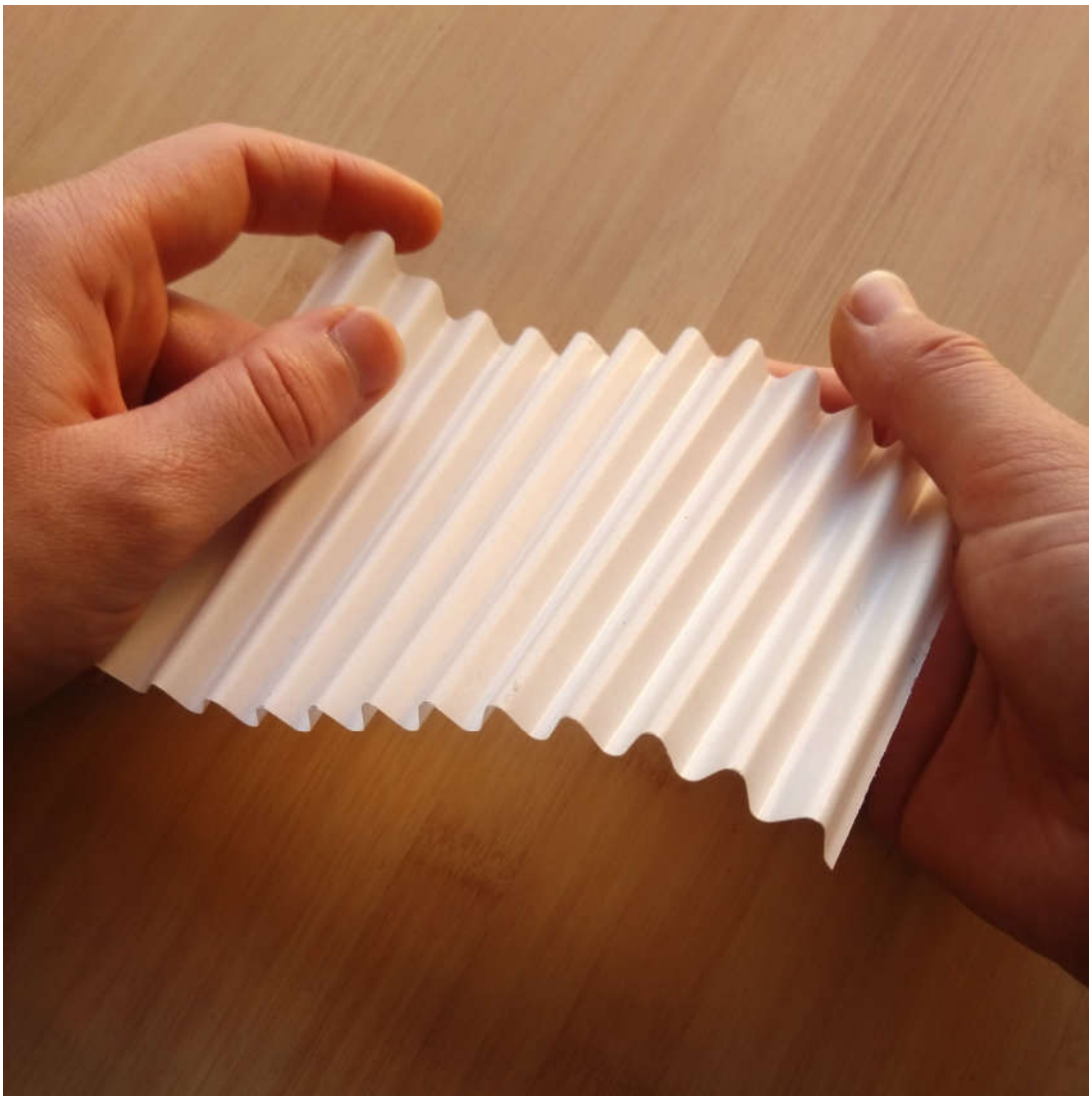

Fig. 5.3.: A groovy sheet. A thin, rubber-coated plastic sheet with thickness $0.075\ \mathrm{mm}$ is shown. The sheet has parallel corrugations, or grooves. The thickness is much smaller than the sheet's size and the groove wavelength.

Fig. 5.3 shows what a typical groovy sheet looks like. Its underlying material is thin and flat, much wider and longer than it is thick. Straight grooves (whose width and height are also much bigger than the thickness) run like parallel waves along one direction. While the example shown is of just the right size to be held in hand, their absolute size is not very important. As long as the material's thickness is much smaller than any other relevant lengths, we consider it a groovy sheet.

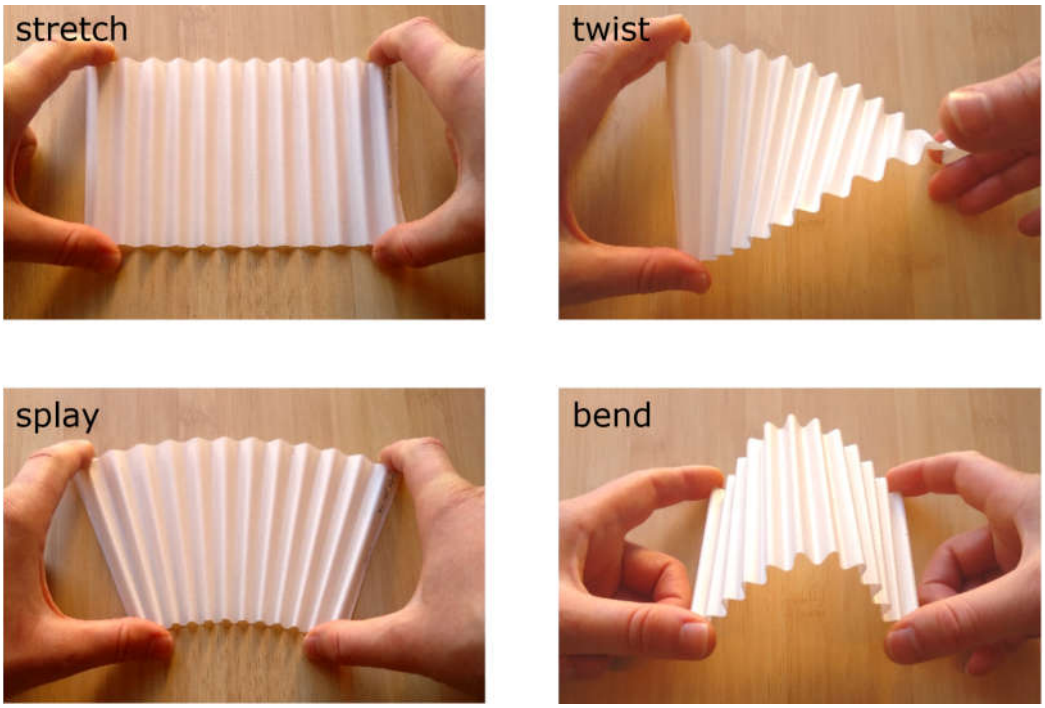

Fig. 5.4.: Groovy sheets deform easily. Left to right, top to bottom: a sheet can easily be stretched, bent, splayed, and twisted by pulling or rotating its sides uniformly. These deformations appear to dominate the sheet's mechanical behaviour.

Fig. 5.4 gives some intuition on how groovy sheets deform when they are manipulated. Stretching, twisting, splaying, and bending of the groovy sheet are easy to do. Interestingly, these deformation modes are dominated by *bending* of the underlying sheet material: overall sheet stretching does not require local material stretching.

Groovy sheets can do more than just bend and twist. Strange things happen when we apply the right boundary conditions, illustrated in Fig. 5.5. There, we pull on a groovy sheet by pinching it at two points at its edges. Initially, the sheet stretches as usual (Fig. 5.5a). But as we continue to pull, something unusual happens: the sheet's grooves *snap through* one by one, starting from the pinching points (reminiscent of the popping of a tape spring[117,148,149]). Small divots are formed in each snapped groove; we call these divots *snap-through defects* (Fig. 5.5b). As we stretch the sheet further, more and more grooves snap through, starting from the edge and into the bulk of the sheet (Fig. 5.5c). At a critical point, all remaining grooves snap through nearly simultaneously at high speed, creating a contiguous line of defects (Fig. 5.5d). Intriguingly, even when we stop pulling, the defects remain, and the sheet curves (Fig. 5.5e). Finally, when the sheet is

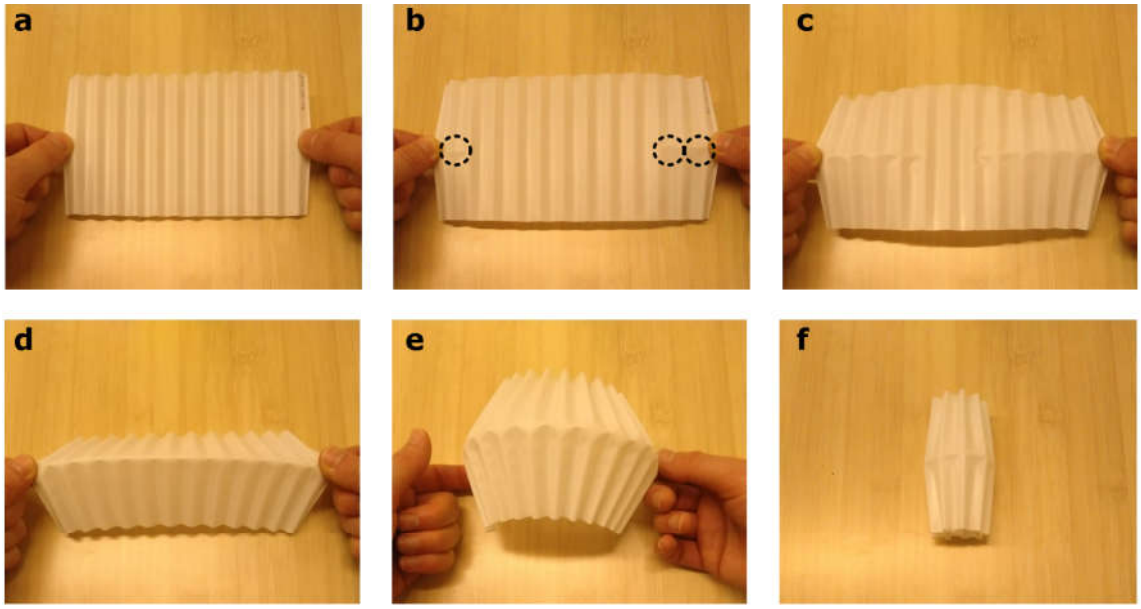

Fig. 5.5.: Groovy sheets reshape, if manipulated right. A sheet is pulled at two points (**a**). At first, the sheet stretches. Then, grooves near the pulling points pop into a new configuration with snap-through defects (**b**, circles). As the sheet is pulled farther, more defects appear slowly (**c**). At a critical point, the remaining grooves snap through rapidly, and defects form a chain (**d**). When the pulling force is released, defects remain and the sheet curves (**e**). Finally, the sheet is free and curls into a compact roll (**f**).

let go completely, it finds a new equilibrium shape: a compact roll (Fig. 5.5f). In other words: the sheet quickly snaps into a new, stable, rolled shape.

But this is not the end: groovy sheets can morph back and forth into much more complex shapes, as we show in Fig. 5.6. There, we show what happens to a groovy sheet (Fig. 5.6a) that is gently crumpled up (Fig. 5.6b,c). When the crumpling force is removed, the sheet has a disordered pattern of snap-through defects and a corresponding irregular shape (Fig. 5.6d). However, when the sheet is gently stretched (Fig. 5.6e), the defects unpop, and the sheet returns with negligible permanent deformation to its original, flat state (Fig. 5.6f). Groovy sheets morph quickly and reversibly into many different shapes, and these are exactly the kinds of features that could make them useful in real-life applications.

Morphing sheets could even find application across scales: crucially, all groovy sheets can shapeshift, whether they are big or small. Fig. 5.7 shows two extreme examples. In Fig. 5.7a, we see a commercial plastic corrugated roofing sheet of around 1 mm thick, its corrugations around 10 cm) wide. Two people, with some persistence, can pop the stiff plastic sheeting into a robust, twisted shape that withstands bumps, scrapes and drops. On the other hand, Fig. 5.7b showcases a small, twisted sheet made using a thin plastic coating that has been detached from corrugated craft paper in an acetone bath. The film is 0.015 mm thick, with grooves around 0.5 cm. Although the two sheets differ by almost a factor one hundred in size, they reshape the same way. The sheet's grooves govern shape-morphing, not its size.

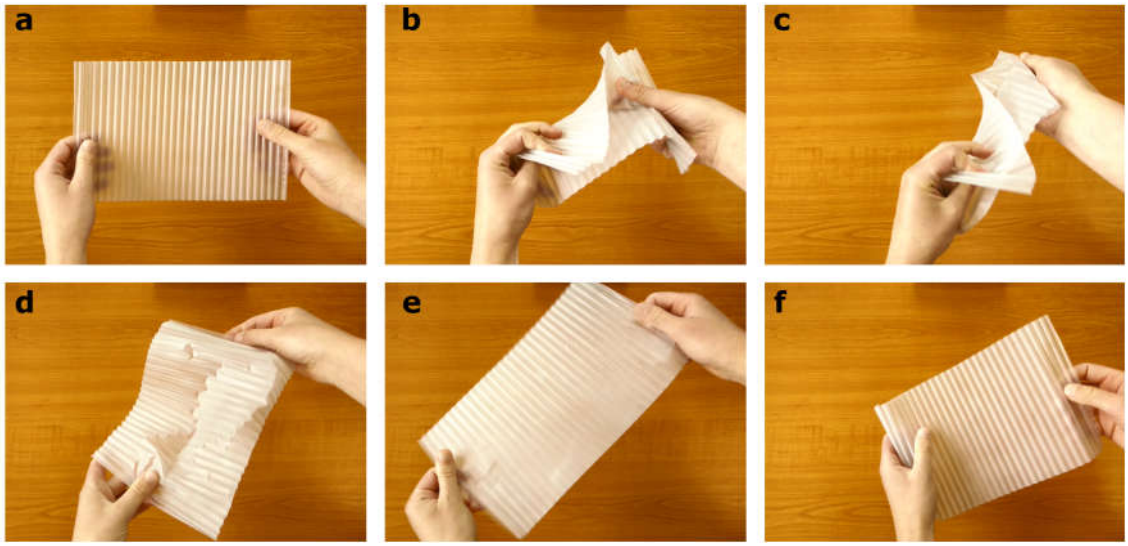

Fig. 5.6.: Groovy sheets reshape reversibly. A groovy sheet (**a**) is crumpled (**b**,**c**). Afterwards, the sheet shows a complex shape and snap-through defect pattern (**d**). Stretching the sheet unpops the defects (**e**) and reverts the sheet to its original flat state (**f**).

Over the course of four years, we have had the opportunity to present our reshaping groovy sheets to many people, both specialists and laypersons. Their response has been consistent. First, the sheet's popping behaviour proved to be evocative. Parallels were drawn to buckling in corrugated roofing, dimpling in pleated fabrics, and childhood memories of playing with packaging material. And second: there seems to be no record of using snapping groovy sheets to create shape-shifting materials.

Here, we address that gap. We explore, quantify, and model how groovy sheets reshape, and discuss prospects for geometry-controlled shape-morphing.

We first define the general shape and size of a groovy sheet in section 5.2, and discuss fabrication methods for plastic and rubber sheets on the centimetre scale. In order to quantify groovy sheet shapes, we introduce two imaging techniques in section 5.3, using both photographic projections as well as full 3D image scanning. Which shapes a groovy sheet can take on depends not only on its starting shape, but also on its (in-plane) elastic properties, which we describe both experimentally and theoretically in section 5.4. As discussed above, groovy sheets reshape due to the introduction of individual snap-through defects in their grooves. We explore the snapping of single defects in section 5.5. However, when more defects appear in the sheet, they start interacting (section 5.6): we will show that adjacent defects attract, which causes them to organize into scar lines of contiguous defects. Stable scar lines have the capacity to dramatically alter the three-dimensional shape of groovy sheets. We quantify this reshaping in the presence of scar lines in section 5.7, and present a hybrid model using both geometric and elastic models that explain groovy sheet's complex shapes. We review our findings in section 5.8, discuss the use of groovy sheets as a novel platform to create reshaping materials, and point out directions to both deepen our insight in and broaden the applications of reshapeable groovy sheets.

Fig. 5.7.: Groovy sheets of all sizes can reshape. a, A commercial plastic corrugated roofing sheet ($1\ \mathrm{mm}$ thick, with groove wavelengths around $10\ \mathrm{cm}$) is reshaped into a robust twisted configuration with the combined strength of two physicists. **b,** Plastic coating film, detached from corrugated craft paper. The film is $0.015\ \mathrm{mm}$ thick, with grooves around $0.5\ \mathrm{cm}$. Although the two sheets differ by a factor of almost one hundred in size, they reshape the same way. Modelling courtesy of Hadrien Bense.

5.2. Making groovy sheets

To study the behaviour of groovy sheets, real samples with well-defined geometric and elastic properties must be made. We present a geometric model and three experimental fabrication processes in sections 5.2.1 and 5.2.2 below, and show that thermoforming of polyethylene sheets inside a rigid mould produces suitable groovy sheets that support re-shaping behaviour.

5.2.1. Geometry

Groovy sheets can come in many shapes. Fig. 5.8 shows the parameters that govern the groove geometry. Specifically, a sheet with N grooves has an overall length L and width W. We assign a local coordinate frame that corresponds to directions orthogonal (ξ) and parallel (υ) to the grooves, and normal (ζ) to the surface (Fig. 5.8a). Zooming in on the groove geometry in Fig. 5.8b, the sheet has a uniform thickness t. The groove amplitude A, wavelength λ, and groove arc length s_λ determine the groove shape.

We assume that the grooves are well-approximated by cylindrical sections of radius of curvature R and opening angle θ, connected by flat facets of length l_{facet}. Relations between these shape parameters are given by the following equations:

$$A = 2R(1 - \cos\frac{\theta}{2}) + l_{\mathsf{facet}} \sin\frac{\theta}{2} \tag{5.1}$$

$$\lambda = 4R\sin\frac{\theta}{2} + 2l_{\mathsf{facet}}\cos\frac{\theta}{2} \tag{5.2}$$

$$s_\lambda = 2(l_{\mathsf{facet}} + \theta R) \tag{5.3}$$

$$\tan\frac{\theta}{2} = \frac{\lambda R + (A - 2R)l_{\mathsf{facet}}}{\frac{1}{2}\lambda l_{\mathsf{facet}} - 2(A - 2R)R} \tag{5.4}$$

$$l_{\mathsf{facet}} = \sqrt{A^2 - 4AR + \frac{\lambda^2}{4}}\ . \tag{5.5}$$

Note that the sheet shape is set by any three independent parameters, for example by the triplet $(R, \theta, l_{\mathsf{facet}})$.

In short, groovy sheets are thin surfaces, uniform along one material direction υ, but with alternating positive- and negative-curvature zones along the orthogonal direction ξ. Borrowing origami terminology, we refer to high- and low-curvature zones as *folds* and *facets* respectively.

5.2.2. Fabrication

To study groovy sheets, we must first make them. Below, we briefly discuss three fabrication methods and their drawbacks and benefits. We study heat-forming thin plastic films with a dynamic and a static method, and review a method to create thin rubber groovy sheets via spin-coating. We show that static heat-forming provides the best results to create reshapeable groovy sheets, and use our experimental findings to identify which groove shapes we can manufacture with this method.

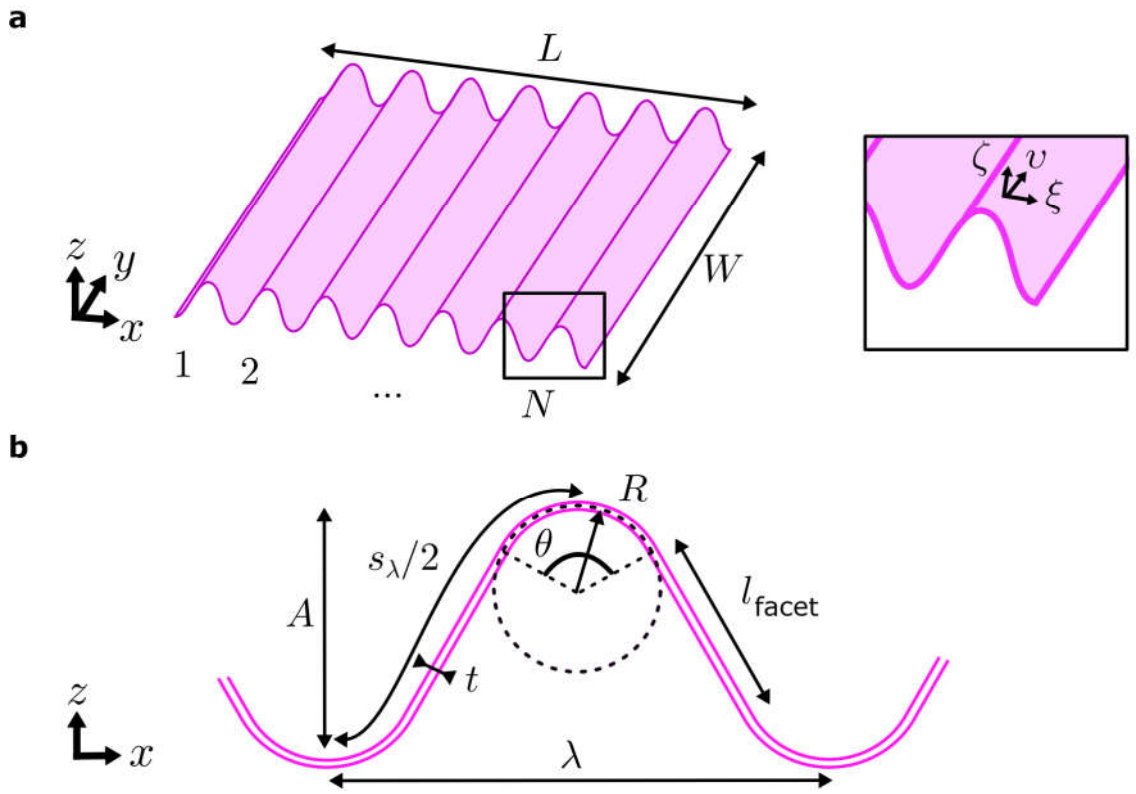

Fig. 5.8.: The shape of groovy sheets. **a**, A thin sheet of length L, width W, with N parallel grooves. Cartesian coordinates x, y, z are indicated. Inset: local sheet coordinates ξ, υ, ζ. **b**, Cross-section of a groove with thickness t, wavelength λ, amplitude A and arc length s_λ. We think of grooves as cylindrical sections with radius of curvature R and subtended angle θ, connected by flat facets of length l_{facet}.

Material choice

Making experimental groovy sheets starts with choosing a suitable material. We need a material that is easily formed into a thin sheet with grooves; that has a large range of elastic rather than plastic behaviour; and that is sufficiently stiff not to be influenced strongly by gravity. We consider biaxially-oriented polyethylene terephthalate (BoPET) film, which softens under heating and can be *thermoformed*, and polyvinyl siloxane (PVS) rubber, which can be *spin-cast* as a fluid.

Thermoforming plastic film

We discuss here how to fabricate samples by heat-forming plastic via two methods: a dynamic method, using counterrotating, heated gears; and a static method, using a compression mould and oven. We use biaxially-oriented polyethylene terephthalate (BoPET) as our base material: specifically, uncoated 'Mylar-A' films produced by Dupont Teijin[150] in a thickness range of 23 to 125 µm.

In order to create suitable groovy sheets out of BoPET film, the following material properties are important (Fig. 5.9). First, the temperature to which the material needs to be heated in order to effectively re-form the film is set by the glass transition temperature. Secondly, the importance of gravity is determined by the film's bending modulus, which is set by the structure's size, specific weight, and Young's modulus. Lastly, to what extent the film can be deformed without incurring permanent, plastic damage is set by the yield point at room temperature.

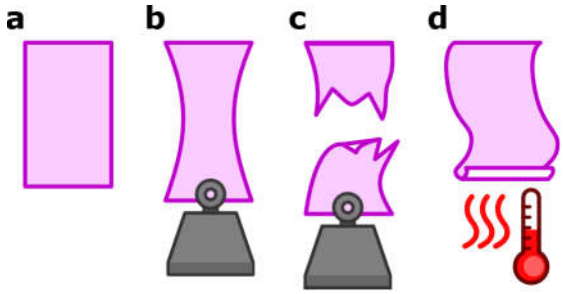

Fig. 5.9.: Important material properties for making groovy sheets. **a,** A piece of thermoplastic film has a stiffness (**b**), yield point (**c**), and glass transition temperature (**d**).

The reported average properties of Mylar-A BoPET[150] at 23 µm thickness suit our needs. First of all, the glass transition temperature of BoPET lies around 80 °C, while the melting temperature lies at 250 °C: the material can be formed in a conventional oven.

Second, the material's tensile modulus lies between 4.8 and 5 GPa in its two orthogonal directions. We experimentally confirm the Young's modulus, to be $E = 5 \pm 0.3$ GPa (appendix A.6). The high Young's modulus and low specific weight (1.39 gram/cm^3) of the material mean that thin sheets will be weakly affected by gravity. Consider how a sheet of length L, width W, thickness t, and density ρ deflects under gravity. When subjected to a gravitational force per unit length $f_g = tw\rho g$, where g is the gravitational constant, the sheet deforms. Euler-Bernoulli beam theory[151] tells us that the deflection has a typical length $d_g = C\frac{f_g L^4}{EI}$, where $I = \frac{Wt^3}{12}$ is the sheet's area moment of inertia. C is a numerical constant that depends on how the sheet is held, and is typically of magnitude $\mathcal{O}\left(10^{-2}\right)$ to $\mathcal{O}\left(10^{0}\right)$. We consider gravitational deflections to be small as long as $d_g \ll L$, and find a condition $\frac{C\rho g}{E} \ll \frac{t^2}{L^3}$ that must hold for gravity to have a

small influence. We define a dimensionless gravity number:

$$N_g = \frac{\rho g L^3}{E t^2} \ . \tag{5.6}$$

If N_g is much smaller than unity, gravity is negligible. An order-of-magnitude estimate for our sheets produces gravity numbers below $\mathcal{O}\left(10^{-1}\right)$ for thicknesses above 50 µm, indicating that gravity plays a minor role for sheets of sufficient thickness.

Lastly, BoPET's yield point at room temperature lies around a yield strain of 0.02 and corresponding yield stress of about 100 MPa, in line with experimental measurements of the yield strain and stress $\epsilon_y = 0.025 \pm 0.007$ and $\sigma_y = 96 \pm 5$ MPa respectively (appendix A.6). The material's yield strain is relatively low, and samples may be affected by plastic yielding. However, when the groove's radius of curvature R is much bigger than the sheet thickness t, plastic damage is expected to be minimal as long as $\frac{R}{t} \gtrsim 14$ (appendix A.7).

Thermoforming plastic sheets can be done in several ways. We first discuss a dynamic forming method using counterrotating gears, illustrated in Fig. 5.10a. The basic idea is that a PET film is guided between two counterrotating, heated gears, in order to shape it into a groovy sheet. To do this, two hollow elongated gears of around 20 cm length, machined from aluminium plate, are mounted inside a metal casing on parallel spindles with heating rods inserted in their centres. The gears, driven by an external high-torque motor, counterrotate. The heating rods are connected to a PID controller and a heat-sensitive camera, which allows the gear temperature to be controlled with an accuracy of around 5 °C. PET sheets are fed into the gear system via a slot in the casing, and emerge with a groovy shape.

To obtain a controlled groove geometry, the gears have a specific size (Fig. 5.10b): the gear diameter D lies at 23.5 mm, while the teeth have amplitude $A = 5.2$ mm, pitch $\lambda = 4.6$ mm, inner and outer radii of curvature $R_1 = 0.6$ mm and $R_2 = 1.3$ mm, and an adjustable separation distance d close to the sheet thickness, tens to hundreds of micrometers. The typical resulting groove shape is shown in Fig. 5.11. Samples are fabricated at an average feed-through speed of 1.5 ± 0.5 mm/s and a temperature of 90 ± 5 °C. While the sheets have a clearly visible groove profile, the amplitude is limited by a short forming time and a long cooling time; typical ratios of groove amplitude A to pitch λ lie around 0.3, with thicker sheets producing larger ratios. The forming time is limited by the gears' speed, which must be high enough to overcome the setup's frictional torque; and the cooling time is limited by a high gear temperature and the sheet's specific heat, which causes the grooves to sag outside the confines of the gears before hardening. Thus, while the dynamic forming method is fast, it is not suitable for making grooves with large amplitudes.

Besides the dynamic method above, static thermoforming can also be done using heated moulds as shown in Fig. 5.12a. Here, a PET film is placed on a corrugated mould of around 30 by 30 cm, machined from aluminium plate. Matching inserts are used to push the film into each corrugation, and are fastened on the mould with screws. The entire assembly is placed into a commercial oven and heated for one to two hours. After cooling for several hours, the thermoformed groovy sheet can be removed from the mould.

The mould's geometry sets the size of the grooves (Fig. 5.12b): the mould's corruga-

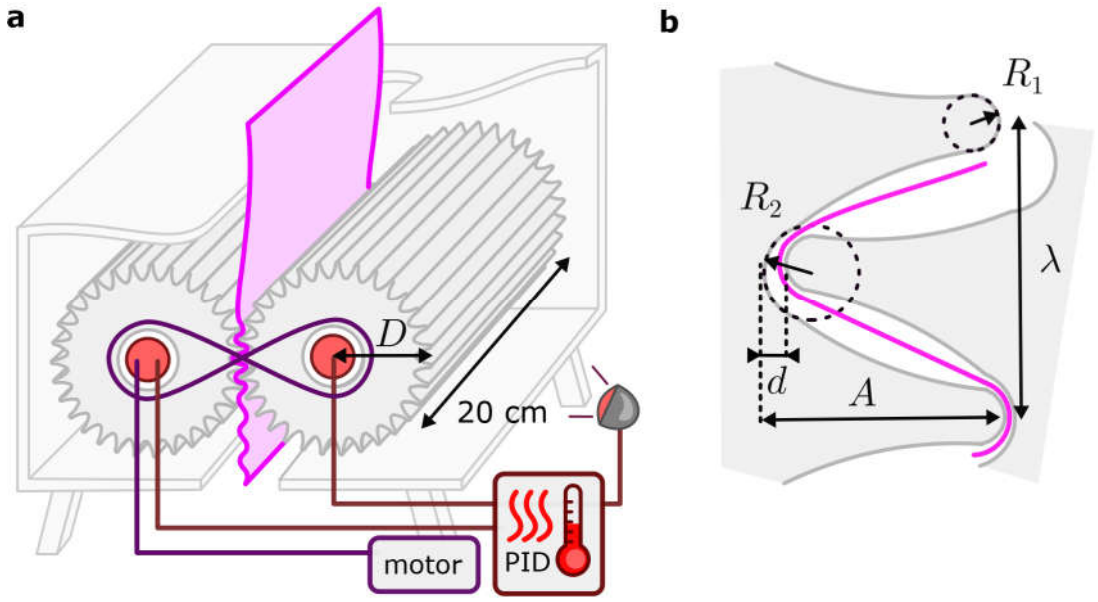

Fig. 5.10.: Dynamic thermoforming with heated gears. **a**, A schematic presentation of the setup. Two aluminium gears (grey), $20\ \mathrm{cm}$ long and with diameter D, are mounted on parallel spindles. One spindle is rotated by an external motor; a serpentine belt passively drives the second spindle. A heating rod (red) is inserted into the hollow centre of each gear. The gears are kept at temperature via a heat-sensitive camera connected to a PID controller. The gears are mounted inside a metallic casing. Flat plastic film (pink) is fed into the gears via a slot in the casing, and emerges with plastically deformed grooves. **b**, Gear geometry. Tooth amplitude A, tooth pitch λ, inner and outer radii R_1 and R_2, and gear spacing d are shown (values: see main text). The sides of each tooth are concave to ensure smooth rotation. An inserted sheet (pink line) deforms accordingly.

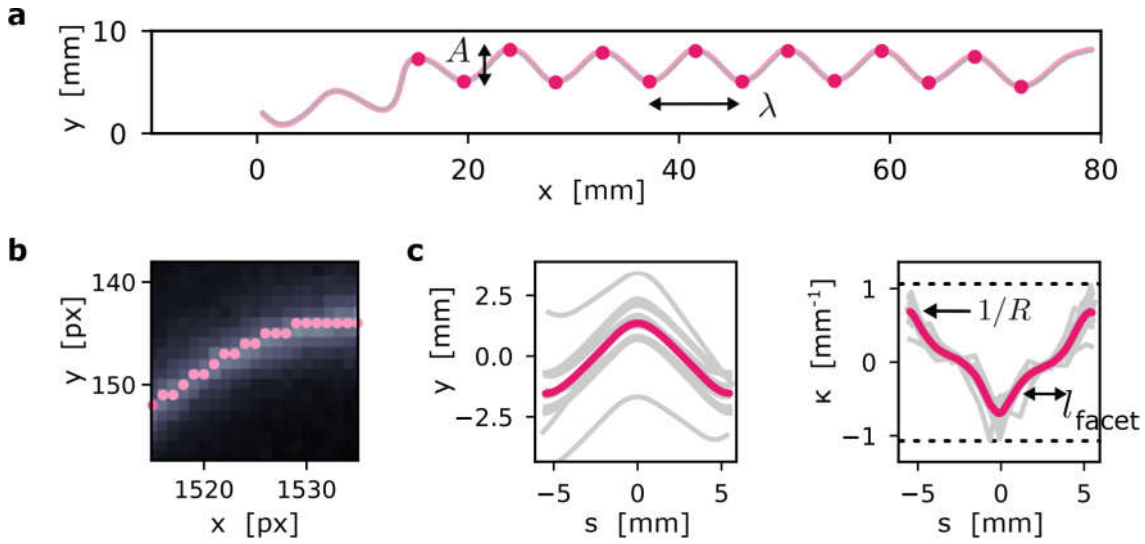

Fig. 5.11.: Typical shape of gear-thermoformed sheets. **a**, The post-forming shape of a $50\ \mu\mathrm{m}$-thick sheet (grey line), fed through the machine shown in Fig. 5.10. The location of the groove centres (pink dots) is used to calculate an average amplitude $A = 2.9 \pm 0.3\ \mathrm{mm}$ and wavelength $\lambda = 8.8 \pm\ 0.3\mathrm{mm}$. **b** Zoom-in of a CCD-camera image of the sheet's side (greyscale). The sheet profile (pink dots) is obtained from the image with a custom Python program. **c** Left: averaging over the grooves (grey lines) produces a mean groove height y (pink line) as a function of path length s, which can be used to calculate an average local curvature κ (right, pink line). The average maximum radius of curvature $R = 1.4 \pm 0.2\ \mathrm{mm}$ lies near the average radius of curvature $1/2(R_1 + R_2) = 1.05\ \mathrm{mm}$ of the gears' teeth (black dashed line). The curvature flattens to zero along the grooves' facets, as expected. The typical facet length lies around $R = 3\ \mathrm{mm}$.

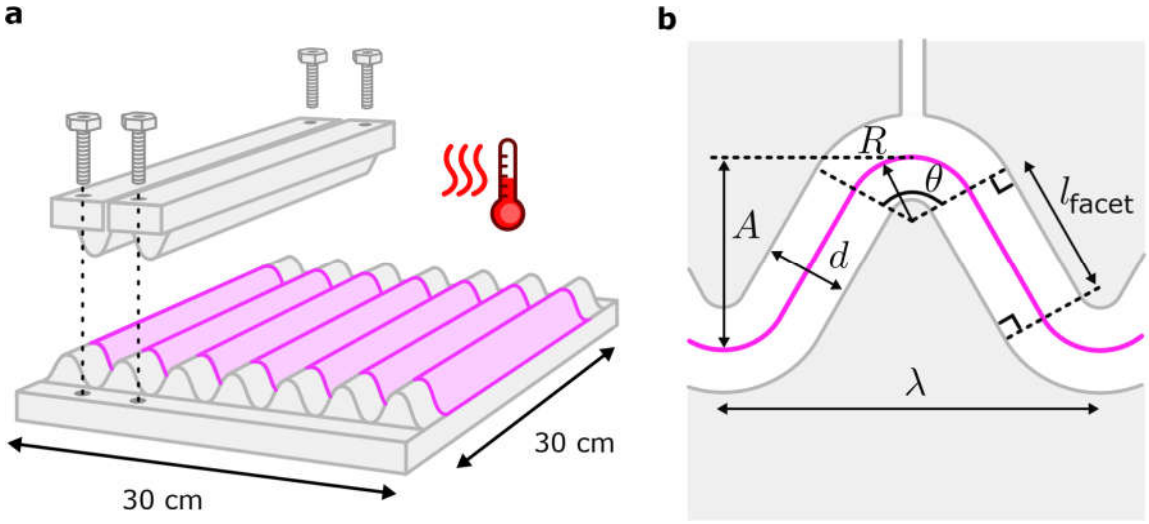

Fig. 5.12.: Static thermoforming with a heated mould. **a**, Schematic illustration of the process. Flat plastic film (pink) is placed on an aluminium mould (grey) with machined grooves. Rods with a complementary shape push the film into each groove and are fastened on the mould with screws. The effective forming surface is 30 cm in each direction. The mould is heated in a commercial oven to thermoform the confined film. **b**, Mould groove geometry. Amplitude A, wavelength λ, mean radius R, curve angle θ, facet length l_{facet} and mould spacing d to accommodate the film's finite thickness are shown. The film's mid-surface (pink line) is indicated.

tions have amplitude $A = 6.812$ mm, wavelength $\lambda = 7.437$ mm, mean radius of curvature $R = 1.5$ mm, groove angle $\theta = 160$ °, facet length $l = 4.4$ mm, and a spacing $d = 50$ µm between the mould and the inserts. We fabricate samples by thermoforming sheets in the mould for an average of 1.5 h at 120 °C and cooling for at least 2 h to allow the assembly to cool below PET's glass transition temperature at 80 °C. The typical groove shape is illustrated in Fig. 5.13. The resulting sheets have a clear groove profile, and achieve a higher ratio of groove amplitude versus pitch than the dynamic method above at a typical ratio of $A/\lambda \approx 0.5$. In addition, the statically formed sheet have less shape variation across the grooves (compare Figs. 5.11c and 5.13c). Thus, while the static forming method is slow, it produces consistently shaped grooves with large amplitudes.

Spin-coating rubber

Groovy sheets can be made by letting liquid rubber cure on a corrugated mould, as we show below. We use polyvinyl siloxane (PVS) rubber, a silicone elastomer that is formed from two liquid polymer compounds via a platinum-based addition reaction. Specifically, we use 'Elite Double' PVS rubber produced by Zhermack[152] of Shore hardness 22 to 32, corresponding to Young's moduli between 0.8 and 1.24 MPa[153].

We fabricate thin groovy sheets out of PVS by spin-coating the liquid rubber on 3D-printed moulds (Fig. 5.14a; for geometry, see Fig. 5.12). We use a simple setup, consisting of a platform mounted on a rotating motor running at (several) hundred RPM[154]. The rubber-coated mould is placed at the edge of the platform while the liquid rubber cures over a timespan of several minutes. A centrifugal force spreads the rubber across the mould's surface. This method produces groovy sheets with an average thickness of

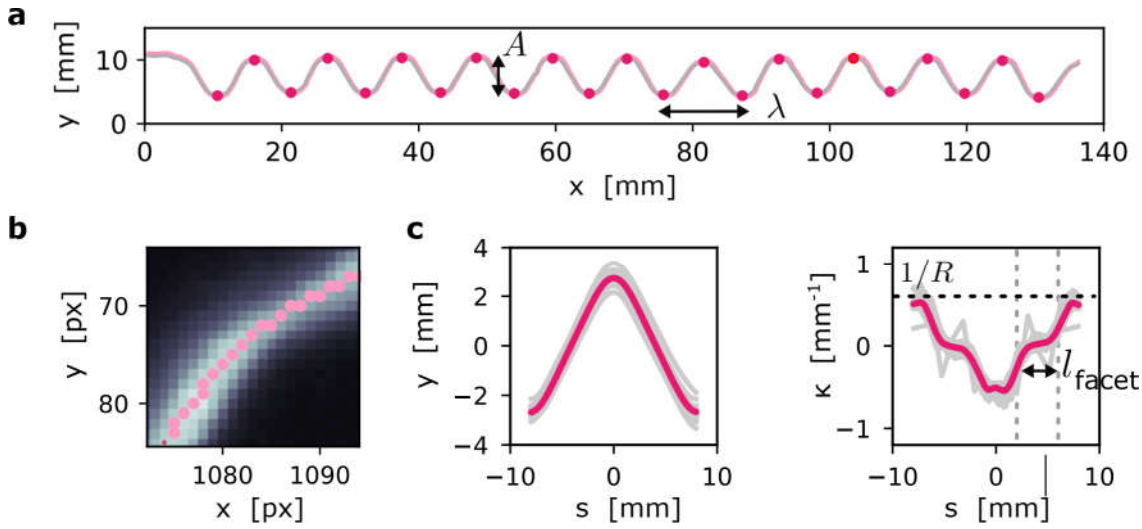

Fig. 5.13.: Typical geometry of mould-thermoformed sheets. **a**, Cross-section of a 75 µm-thick sheet after forming in the mould setup shown in Fig. 5.12a (grey line). Automatically detected groove positions (pink dots) yield an average amplitude and pitch $A = 5.4 \pm 0.3$ mm and $\lambda = 10.9 \pm 0.3$mm. **b**, Zoom-in of a CCD image (greyscale) and detected groove pixels (pink dots). **c**, The groove height as a function of arc length s along the sheet (left) is used to calculate the local curvature κ (right). The average radius of curvature of the fold, $R = 2 \pm 0.2$ mm, lies close to the mould's corrugation design (black dashed lines); the facet size l_{facet} matches well with their target length (grey dashed lines).

several hundreds of microns, with variations of tens of microns between upward- and downward-curving grooves[154].

While PVS rubber has a much larger elastic regime than plastic sheet material, its low Young's modulus compared to its specific weight (somewhat larger than that of water) makes rubber groovy sheets sensitive to gravity. For comparison, the gravity number of PVS compared to BoPET sheets (Eq. 5.6) is larger by three orders of magnitude: PVS groovy sheets must be suspended in a density-matched medium to counteract the effects of gravity.

Crucially, as Fig. 5.14b shows, rubber groovy sheets suspended in a solution of water and table salt exhibit multistability. They support defects and can be reshaped, implying that neither plasticity and residual stresses or strains nor a constant thickness are necessary to induce multistability in groovy sheets.

Conclusion

We have explored three distinct methods to fabricate groovy sheets: dynamic thermoforming of PET film; static thermoforming of PET film; and spin-coating silicone rubber.

Summarizing this section's findings, we find that thin plastic film has a high Young's modulus and small specific weight, which reduces the impact of gravity. Commercially produced film is widely available in a range of well-controlled thicknesses. While plastic has a relatively low yield point, a large ratio between groove radius of curvature and

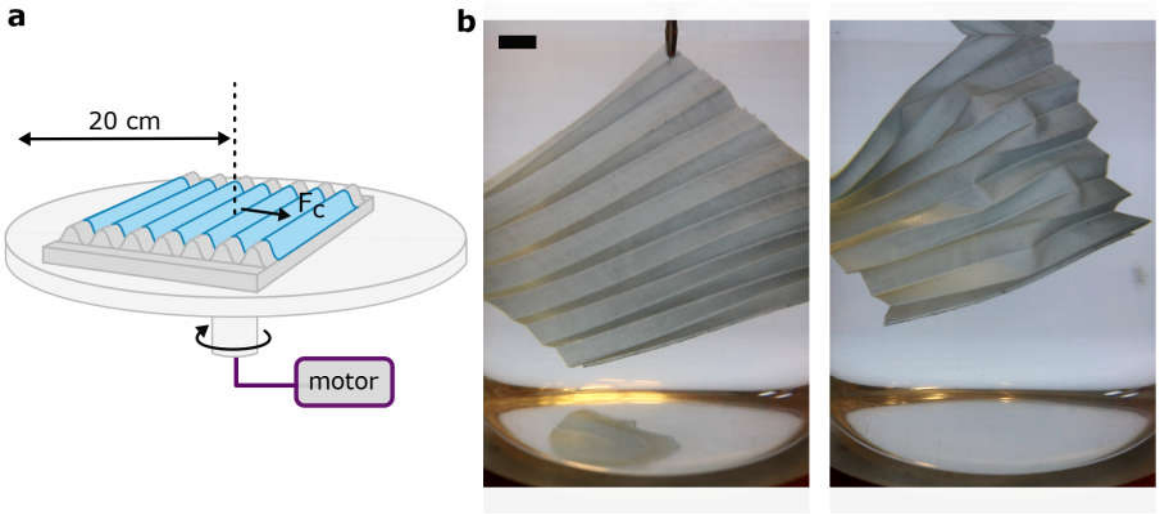

Fig. 5.14.: Spin-coating rubber groovy sheets. **a**, Schematic spin-coating setup. Liquid rubber (blue) is poured on a corrugated mould (dark grey) that is mounted on a motorized rotating platform (light grey). The rotation induces a centrifugal force F_c that spreads the liquid across the mould as it cures over several minutes. **b**, Example of a spin-coated rubber groovy sheet, suspended in an approximately density-matched solution of water and table salt (left). The sheet supports stable pop-through defects (right), suggesting that the reshaping of groovy sheets is in principle an elastic process. Scale bar: 1 cm.

sheet thickness will reduce the impact of plastic yielding. With static thermoforming, we may use temperature and forming time to vary the groove shape within a small range. In addition, bistability in groovy sheets occurs only for a range of groove geometries, as we discuss in more detail below; typically, the material's thickness must be much smaller than the groove's other length scales. The small thickness of plastic film means that the grooves, and our samples, remain of a suitable size for laboratory experiments. Static thermoforming, where a thin plastic sheet is confined in a heated metal mould, therefore meets the project's needs best.

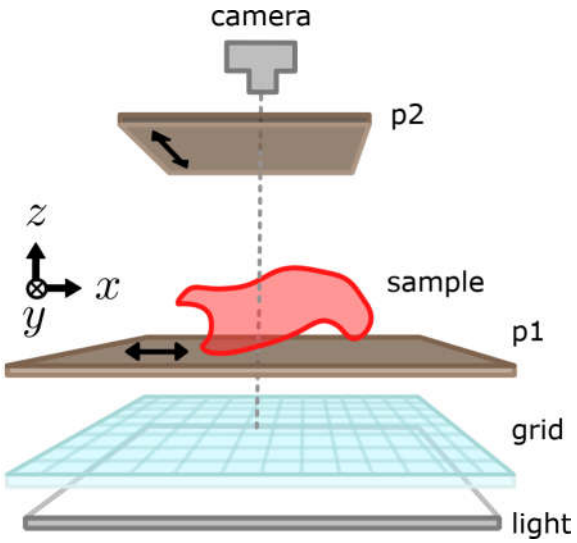

Fig. 5.15.: Photography setup for deformed groovy sheets. Images of a groovy sheet are taken by a Canon EOS 750D camera mounted over the sample. An LED light source backlights an alignment grid etched onto a transparent acrylic sheet (blue). A linearly polarising sheet (p1) is placed on the grid, and the transparent, birefringent BoPET sample is placed on top (red). A second linear polariser (p2) ensures that the light sample is contrasted by a dark background in the image recorded by the camera.

5.3. Measuring groovy sheet shapes

Groovy sheets deform in intricate ways, and their complex shapes must be quantified carefully. We use two imaging methods for shape measurements, which we discuss below. Section 5.3.1 lays out how we use photography to extract 3D shape information from a projected 2D image; and section 5.3.2 treats a 3D-scanning method, where we analyse groovy sheet shapes by projecting phase-shifted fringe patterns on them.

5.3.1. 2D photography

Groovy sheets can deform to cylindrical and helical shapes that are symmetric and regular. Their overall features can be captured by analysing 2D projections of a deformed sheet. We record such 2D images with a Canon EOS 750D camera at a resolution of 22 px/cm behind a linear polariser (see Fig. 5.15) mounted over a flat transparent surface, back-lit with LED lights and covered with a second linearly polarizing sheet. Samples are aligned manually on the surface, aided by a semi-transparent sheet with regular grid lines. Representative examples are shown in Fig 5.16; characteristic shape measures such as cylinder diameters (Fig 5.16a-b) or twisting angles (Fig 5.16c) can be extracted from these images with custom-built Python scripts as reported in section 5.7.

5.3.2. 3D imaging

In order to record the full three-dimensional shapes of our groovy sheets, we use an imaging method based on phase shifts in projected fringe pattern[155–157]. We review the 3D

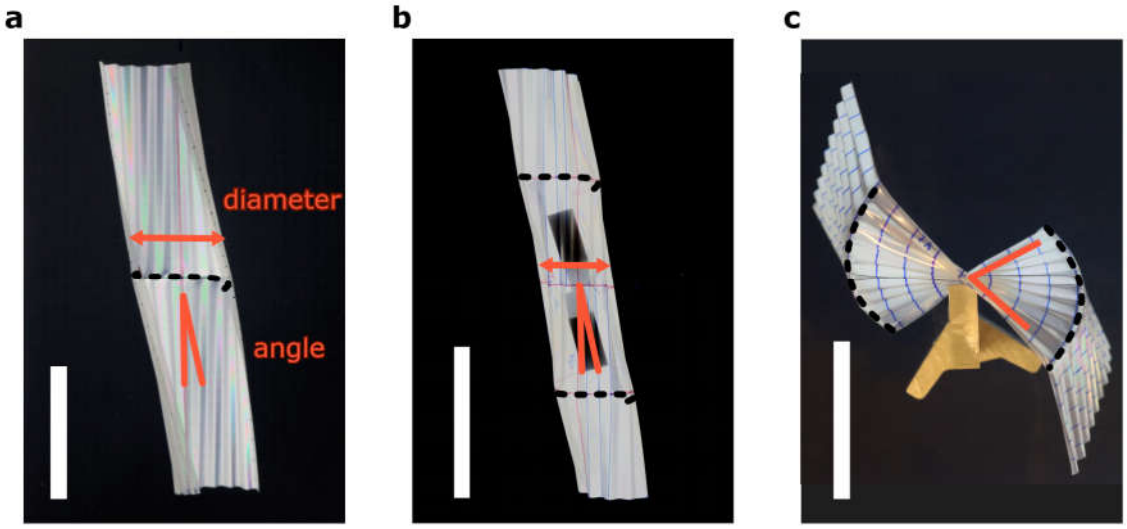

Fig. 5.16.: Typical 2D images of groovy sheets with one or two scars. a, A groovy sheet deformed into a twisted cylindrical shape (white) by the presence of a scar (dashed line) has a diameter and twist angle (red markers) that will be measured with an automated script in section 5.7. **b,** Two scars (dashed lines) on the same side of a groovy sheet produce a cylindrical, twisted shape with a measurable diameter and twist angle. **c,** Top view of a sheet with two scars on opposite sides. The helix-like surface with side lobes has a twist angle that will be measured manually in section 5.7. Scale bars: 5 cm.

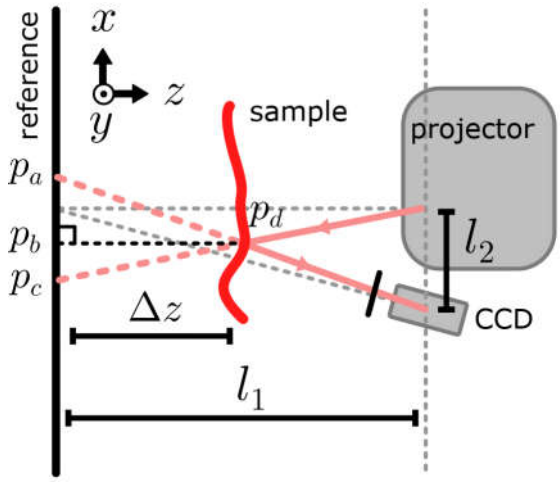

Fig. 5.17.: Schematic top view of the 3D imaging setup. A projector (top right) projects a sinusoidal fringe pattern on the reference plane (left) at a distance l_1. The projector's optical axis (grey dashed line) is orthogonal to the reference. A CCD camera (bottom right) captures the fringe pattern, after being placed at distances l_1 from the reference plane and l_2 from the projector. The camera's optical axis is indicated (grey dashed line). The imaging coordinates x, y, z are shown (top left). Placing a sample in front of the reference plane (red line) distorts the captured fringe pattern. The original and distorted pattern's phase shift between points p_a and p_d may then be used to calculate the sample's height profile $\Delta z = p_c - p_b$ (see main text) via trigonometric relations.

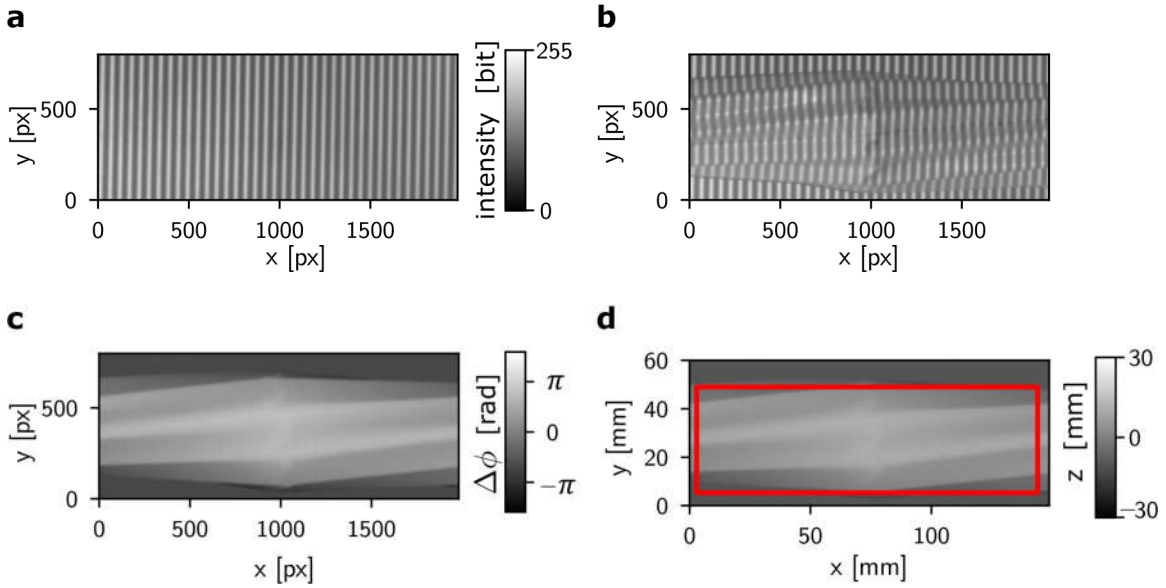

Fig. 5.18.: Image reconstruction to extract a 3D shape from a set of 2D images. **a,** A reference image of a projected sinusoidal intensity profile, recorded using the scanning setup of Fig. 5.18. Scale bar: light intensity (bit). **b,** Typical data image, in which the intensity profile is distorted by the presence of a groovy sheet with a central scar. Scale bar: see **a.** **c,** Phase difference $\Delta\phi$ (colour bar) of the distorted intensity profile, extracted from four doublets of reference and data images. Each doublet uses the same projected intensity profile, but is phase-shifted by $[0, \pi/4, \pi/4, \pi/4]$ respectively. **d,** Axes are rescaled to obtain width y, length x, and height z (colour bar) of the scanned surface. The approximate region of interest (red outline) is identified via a custom edge detection algorithm.

setup, image reconstruction, and typical results here.

A schematic view of the 3D imaging setup is shown in Fig. 5.17. We use an Epson EMP-X3 projector to project images of a sinusoidal fringe pattern on a blank, flat reference surface at 110 cm distance. A Basler acA2040-25gm camera, fitted with a Kowa lens of focal distance 75 cm, is positioned next to the projector at a distance of 15 cm from the projector and 110 cm from the reference surface. The fringe pattern has a wavelength of 52.7 px. The spatial resolution of the setup is 0.075 mm per pixel, which allows us to resolve the groove shape to a good degree of detail.

We now briefly describe how to obtain 3D shapes with this imaging setup, in line with the methods described in Refs. [155–157]. Basically, we project a sinusoidal fringe pattern on the reference surface and record it with a camera. The planar intensity profile of the sinusoidal pattern is given by

$$I^0_{\Delta\psi}(\boldsymbol{r}) = a_k e^{i\boldsymbol{k}\cdot(\boldsymbol{r}+\Delta\psi)} \ , \tag{5.7}$$

where $\Delta\psi$ is the pattern's phase offset. When an object is placed in front of the reference surface, the projected fringe pattern is distorted (red line in Fig. 5.17). The object creates a height offset $\Delta z(\boldsymbol{r})$. The distorted sinusoidal pattern can be described via

$$I_{\Delta\psi}(\boldsymbol{r}) = a_k e^{i\boldsymbol{k}\cdot(\boldsymbol{r}-\boldsymbol{u}(\boldsymbol{r}))+\Delta\psi} \ , \tag{5.8}$$

where $\boldsymbol{u}(\boldsymbol{r})$ is the in-plane pattern distortion (e.g. $p_d - p_a$ in Fig. 5.17). The height offset

$\Delta z(\boldsymbol{r})$ is then reconstructed from the reference and distorted fringe images by comparing their respective phase maps. To obtain difference between the two phase maps, we take four variations of the projected fringe pattern with distinct phase offsets $\Delta\psi \in [0, \pi/2, \pi, 3\pi/2]$. The phase difference $\Delta\phi$ between the recorded reference and distorted patterns can then be calculated, based on a linearisation of the intensity distortion:

$$\Delta\phi = \phi(p_d) - \phi^0(p_a) \tag{5.9}$$

where

$$\phi^0 = \arctan \frac{I^0_{3\pi/2} - I^0_{\pi/2}}{I^0_\pi - I^0_0} \tag{5.10}$$

$$\phi = \arctan \frac{I_{3\pi/2} - I_{\pi/2}}{I_\pi - I_0} \tag{5.11}$$

$$\tag{5.12}$$

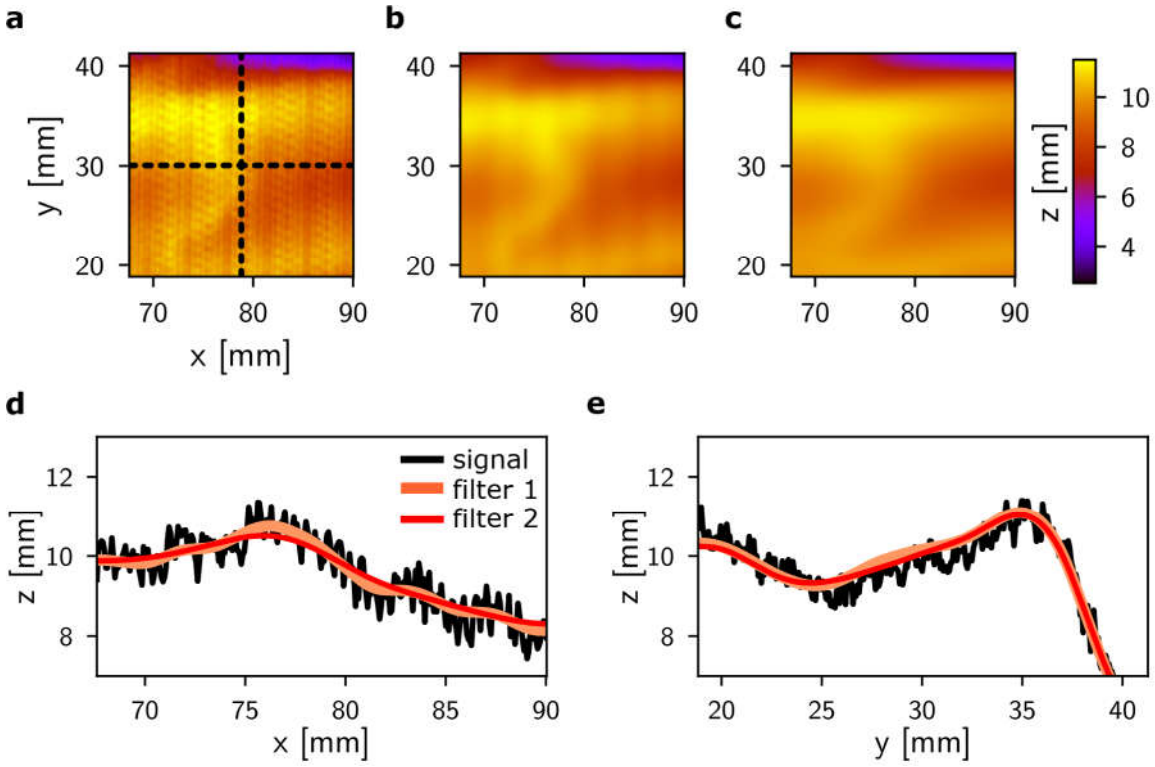

Fig. 5.19.: Noise reduction by low-pass filtering. **a,** Representative image of a noisy height profile (colour bar) of a groovy sheet near a defect. Residual noise from both the beamer's limited resolution as well as the fringe pattern's deviation from a perfect sine can be seen. **b,** Smoothing with a 2D low-pass Gaussian filter (legend: filter 1) to remove resolution noise from the signal. **c,** Sine-deviation noise is reduced with a second 1D low-pass Gaussian filter (legend: filter 2). **d,** Cross section of height profile corresponding to horizontal dashed line in **a**. Data passed through filter 1 still shows sine deviation noise, while data passed through filter 2 does not (legend). **e,** Height profile along vertical dashed line in **a**. Both filters show reduction of resolution-limited noise. Shifting of the profile is due to the two-dimensional smoothing of filter 1.

In turn, the phase difference is related to the height offset via the following geometric

relation, which assumes our setup behaves as an optically linear system:

$$p_a - p_c = \frac{\lambda}{2\pi}\Delta\phi \tag{5.13}$$

$$\Delta z(\boldsymbol{r}) = \frac{(p_a - p_c)l_1}{(p_a - p_c) + l_2} \ , \tag{5.14}$$

where p_a, p_c are shown in Fig. 5.17, and λ is the fringe spacing on the reference plane. In short: projecting phase-shifted fringe profiles on groovy sheets allows us to reconstruct their three-dimensional shape using a limited number of recorded images.

The steps of the reconstruction procedure are illustrated in Fig. 5.18, where panel 5.18a shows an example of a sinusoidal intensity profile projected on a flat reference surface. The presence of a reshaped groovy sheet sporting a central scar distorts the pattern (Fig. 5.18b). With Eqs. 5.7-5.10 above, the phase profile of the groovy sheet is found (Fig. 5.18c). Finally, the sheet's height profile is calculated via Eq. 5.10, and custom Python scripts detect the region that contains relevant data (Fig. 5.18d).

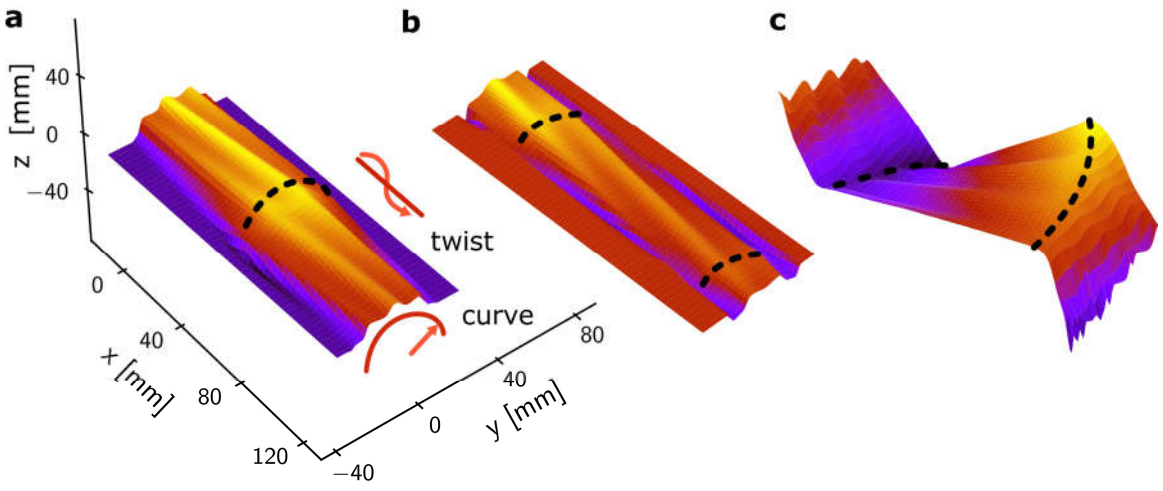

Fig. 5.20.: Typical sections of 3D-scanned groovy sheets. **a,** A groovy sheet deformed into a twisted cylindrical shape by the presence of a scar (dashed line). Grooves and defects can be detected, as well as the cylinder diameter and twist angle (red markers). Colours indicate height z qualitatively. **b,** Two scars (dashed lines) on the same side of a groovy sheet produce similar twisting cylinders. **c,** Top view of a sheet with two scars on opposite sides. Full details of the surface can be used to quantify the exact shape of the central, helicoidal portion.

Fig. 5.19a shows a small section of a 3D height profile; the recorded signal shows high-frequency noise, which we reduce with low-pass filtering. The high-frequency noise arises from two main sources. First, the beamer's projection resolution is limited, which shows up as high-frequency noise. We tackle this issue via Gaussian smoothing with a standard deviation of 10 pixels (corresponding to 0.75 mm on the sample) parallel to the fringes (Fig. 5.19b). Second, the projected fringe pattern is not completely sinusoidal, which induces noise orthogonal to the fringes at high frequencies. We improve this noise with Gaussian smoothing orthogonal to the fringes, with a standard deviation of half the fringe wavelength (corresponding to 2 mm on the sample, Fig. 5.19c). While low-pass filtering reduces the scanning accuracy, the typical length scales of the sheet's important

features (on the order of the groove size, 10 mm) lie above the filtered lengths and are preserved (Fig. 5.19d-e).

In short, 3D scanning allows us to measure the shape of groovy sheets. Fig. 5.20 shows representative examples of 3D scans of cylindrical and twisted shapes that sheets take on in the presence of one (Fig. 5.20a) or two scar lines (Fig. 5.20b-c); these 3D scans contain more information than the corresponding 2D projections shown in Fig. 5.16. Shape measures such as curvatures and twisting angles, but also defect positions, groove trajectories, and twisting angles can be measured in detail, as we will report in section 5.7.

5.4. In-plane elasticity of groovy sheets

5.4.1. Groovy sheets are not symmetric

Groovy sheets have an orthotropic geometry. That means the elastic response in both in-plane directions, along the grooves and across the grooves, is very different (Fig. 5.21). Along the grooves (Fig. 5.21a), the sheet is stiff: its behaviour is governed by stretching of the underlying film material, and its Young's modulus determines the stretchiness. Across the grooves (Fig. 5.21b), the response is soft with a sudden stiffening behaviour: this deformation is dominated by low-stiffness bending that flattens the grooves before the sheet's material is stretched. This type of soft-to-hard transition is typical for many biological tissues, and helps prevent instabilities (such as aneurysms in blood vessels)[158]. By contrast, in our groovy sheets, we find that this particular stress-strain behaviour creates a multistable energy landscape.

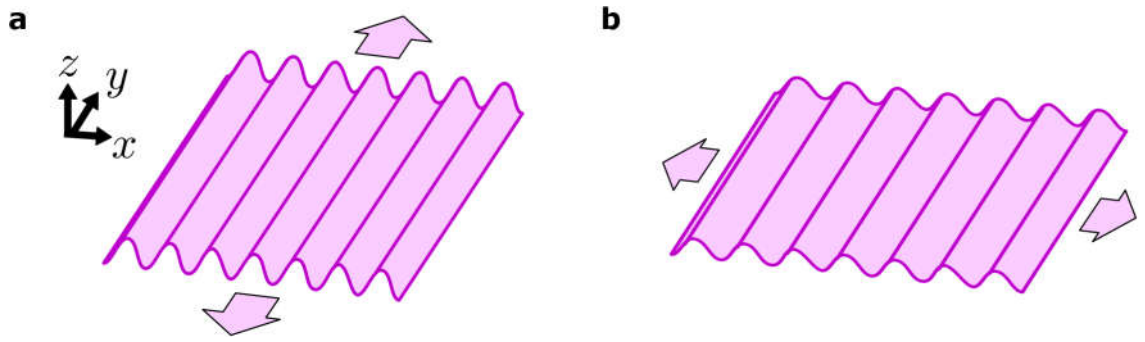

Fig. 5.21.: Groovy sheets are not symmetric under stretching. **a,** Stretching along the grooves (direction $\hat{y}$) results in elongation of the underlying material; this typically costs a lot of energy. **b,** Pulling across the grooves (direction $\hat{x}$) results in bending of the sheet and flattening of the grooves. This deformation mode requires less energy.

In the following sections, we quantify the in-plane elasticity of groovy sheets. We perform experiments and simulations to study the dependence of their response on the groove geometry. In section 5.4.2, we start by estimating the sheet stiffness parallel to the grooves, and contrast this with the experimentally measured stiffness across the grooves in section 5.4.3. Via comparison to a simple discrete model as well as numerical simulations (section 5.4.4), we find a predictive model for a sheet's stiffness. Notably, we find an *effective* stiffness, based on a simple rescaling, that predicts the response of sheets across groove geometries. Finally, we use our findings to create a simple 3D model built from discrete springs (section 5.4.5) whose geometry and stiffness mimics the elastic properties of real groovy sheets. Crucially, the 3D model also mimics the reshaping behaviour of real groovy sheets. Our findings showcase the crucial connection between geometry and energy in our groovy sheets, and show that their shape-morphing behaviour is elastic and reversible.

5.4.2. Stiffness along the grooves

When a groovy sheet is stretched by a uniform force F_y applied along the grooves (Fig. 5.21a), the underlying sheet material must stretch by an amount u_y. We estimate the stretching stiffness as follows, assuming Hookean behaviour and small strains below the material's yield point (see appendix A.6):

$$F_y = \frac{ENts_\lambda}{W} u_y \ , \tag{5.15}$$

where E is the material's Young's modulus, W the N the number of grooves, and s_λ the arc length of a groove (see Fig. 5.8). The relation above shows that the sheet stiffness along the grooves, $\frac{ENs_\lambda}{W}$, is set by the material's Young's modulus- unlike the sheet's behaviour in the orthogonal direction.

5.4.3. Stiffness across the grooves

Experimental measurements show that extending sheets across their grooves with a uniform force does not stretch the underlying material immediately; the grooves flatten our first (Fig. 5.21b). Our experimental setup is shown schematically in Fig. 5.22a: a corrugated sheet, mounted in two clamps, is extended by a displacement u while its response force F is measured (see appendix A.8). The experimental force-displacement curves shown in Fig. 5.22b-c shows the sheet's soft-to-stiff behaviour: at the onset of extension, deformations are bending-dominated and need little force (regime I). Once the sheet is fully flattened out, stretching deformations take over and the force-displacement curve rises rapidly, proportionally to the underlying material's Young's modulus (regime II).

5.4.4. Modelling stiffness

To understand the sheet's behaviour under stretching across its grooves, we present two models here: a discrete simplified one, and a continuum model. While the discrete model helps us understand the qualitative behaviour of the sheet, we will show that the continuum model allows us to predict the experimentally found sheet stiffness quantitatively; surprisingly, this prediction turns out to be largely independent of the sheet's detailed groove shape.

We first discuss a groovy sheet model made with discrete building blocks (Fig. 5.23a). The two-dimensional structure consists of $2N$ bars with rest length s^0 and Hookean stretching stiffness k_s, connected in an accordion-like pattern by torsional springs of rest angle ϕ^0 and stiffness k_t. This creates a sheet-like structure with N grooves. Deviations from the rest length and angle are penalized with a stretching energy $\mathcal{E}_s = \frac{1}{2}k_s\Delta s^2$ and a torsional energy $\mathcal{E}_t = \frac{1}{2}k_t\Delta\phi^2$. The accordion's overall rest length is given by $L = 2Ns\cos\frac{\phi}{2}$, and extensions $u = L - L^0$ of the structure are measured from the rest length $L^0 = 2Ns^0\cos\frac{\phi^0}{2}$. The force F needed to extend the accordion by a distance u can then be calculated via variation of the structure's Lagrangian $\mathcal{L}$:

$$\mathcal{L} = -2N\frac{1}{2}k_t(\phi-\phi_0)^2 - 2N\frac{1}{2}k_s(s-s^0)^2 + F\left(u - 2N(s\cos\frac{\phi}{2} - s^0\cos\frac{\phi^0}{2})\right) \ . \tag{5.16}$$

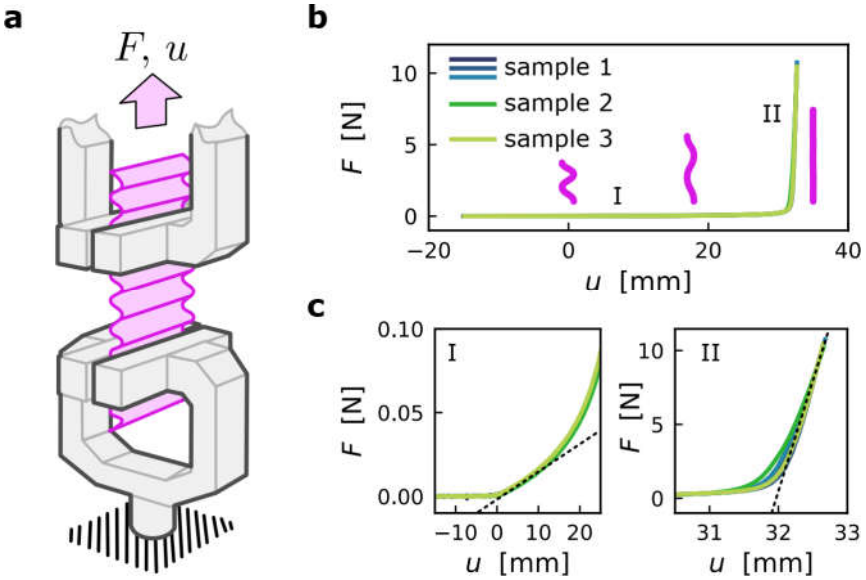

Fig. 5.22.: Experimental measurement of a groovy sheet's stiffness under tension. a, A corrugated BoPET sample with $N = 18$ grooves of thickness $t = 23$ µm, width $W = 3$ cm, total relaxed length 160.5 mm and total flattened length 192.5 mm is mounted between the clamps of an Instron universal testing machine. Displacement u of the upper clamp produces a force F that is measured by a load cell. **b,** Top: reproducible force-displacement curves of three distinct sheets (samples 1-3, see legend), stretched over 33 mm. Insets illustrate the deformed sheet (pink lines). Two regimes, I and II, can be distinguished. **c,** In regime I (left), grooves bend and flatten at low force. In regime II (right), the sheet stretches at high force. Slopes correspond to a distinct stretching stiffness in both regimes (dashed lines).

While there is no analytical expression for the force $F(u)$ for all values of u, it is possible to divide the response into three regimes: bending-dominated at small displacements, stretching-dominated at large displacements, and a mixed response in a narrow crossover regime at intermediate displacements (see appendix A.8 for details).

We briefly review the force response in the regimes of small, intermediate, and large displacements. First, at small values of u, we find

$$F = 2k_t \frac{\Delta\phi}{s^0 \sin\frac{\phi}{2}} \tag{5.17}$$

$$= -\frac{8Nk_t}{(S^0)^2 - (L^0)^2} u + \mathcal{O}\left(u^2\right) \ , \tag{5.18}$$

where $S^0 = 2Ns^0$ and $L^0 = 2Ns^0 \cos\frac{\phi^0}{2}$ are the lengths of the accordion in its flattened and rest states, respectively. Evidently, the force response in this regime depends only on the torsional hinges, and the accordion has an effective stiffness $-\frac{8Nk_t}{(S^0)^2-(L^0)^2}$ to displacements in a small linear regime. However, we can obtain a governing relation for the sheet's elastic behaviour in a much larger regime:

$$\mathcal{W} = \int_0^u F \mathrm{d}u' = -\int_{\phi^0}^{\phi} Ns^0 \sin\frac{\phi'}{2} F \mathrm{d}\phi' = \frac{1}{2}(2Nk_t)\Delta\phi^2 \ . \tag{5.19}$$

Here, $\mathcal{W}$ is the work performed on the sheet during its extension. In the bending-

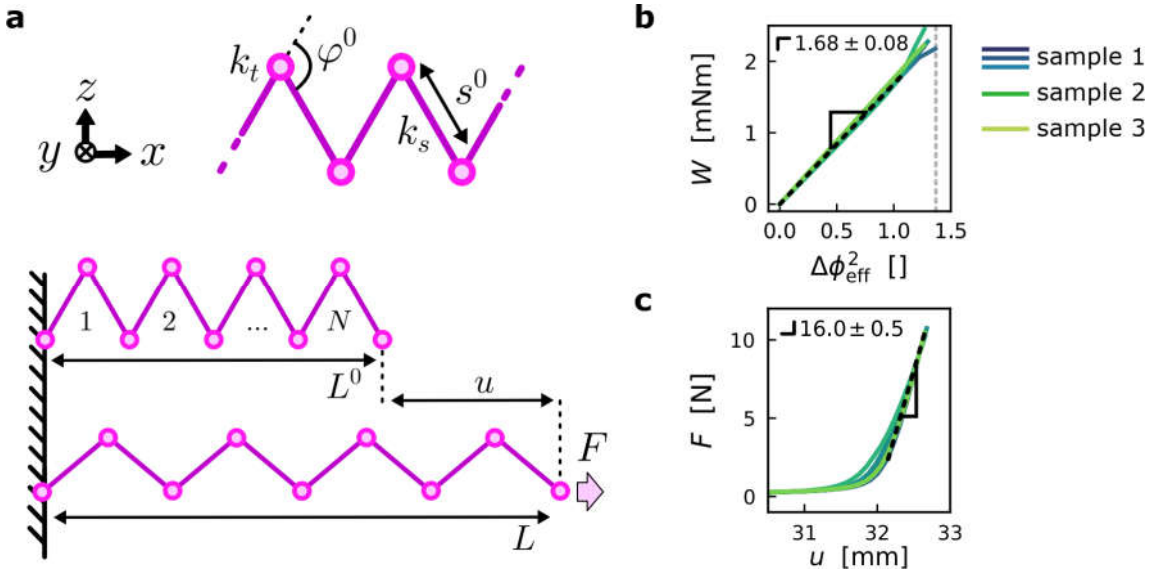

Fig. 5.23.: Discrete model for the extension of a groovy sheet. a, Top: stiff bars with length s^0 and stretching stiffness k_s (purple lines) are connected by soft torsional springs with a rest angle ϕ^0 and torsional stiffness k_t (pink circles) in an accordion pattern. Bottom: a structure with $2N$ bars and N grooves has rest length L^0. Extension by a displacement u to new length L requires a force F. **b,**

dominated regime, it has a purely quadratic dependence on the angle change $\Delta\phi$, with a corresponding stiffness of $2Nk_t$. Since the contrast between bending and stretching stiffness is large, this quadratic relation holds in a large regime of extensions. Secondly, in the crossover regime, the accordion is nearly flattened and the bars start stretching; the force is due to a mixture of hinge bending and bar stretching, and has no analytical form. Finally, when displacements are larger than $S^0 - L^0$, stretching of the bars must take place. In that case, the force reads

$$F = \frac{k_s}{2N}(u + L^0 - S^0) \ , \tag{5.20}$$

which equation shows that the accordion's stiffness $\frac{k_s}{2N}$ in the final regime comes purely from stretching of the bars. These findings match our experimental results, which also show a splitting into a soft, bending-dominated and a stiff, stretching-dominated regime.

We now investigate whether the stiffness parameters of the accordion model, k_s and k_t, can be derived from the geometry of real samples. Using the data of Fig. 5.22 and Eqs. 5.19 and 5.20, we first estimate experimental values of k_t and k_s. In Fig. 5.23b, we present the work $\mathcal{W}$ performed on the sample versus the square of the effective angular change $\Delta\phi_{\text{eff}} = \phi_{\text{eff}} - \phi^0{}_{\text{eff}}$, defined via $\phi_{\text{eff}} = 2\arccos\frac{L^0+u}{S^0}$: the relation is linear to good approximation. In Fig. 5.23c shows the force F versus extension u in the sheet-stretching regime. We find $Nk_t = 1.68 \pm 0.08$ mN m and $\frac{k_s}{2N} = 16.0 \pm 0.5$ N/mm for samples with $N = 18$ grooves, resulting in the following experimental stiffnesses:

$$k_t = 93 \pm 4 \text{ µN m} \tag{5.21}$$

$$k_s = 576 \pm 18 \text{ N/mm} \ . \tag{5.22}$$

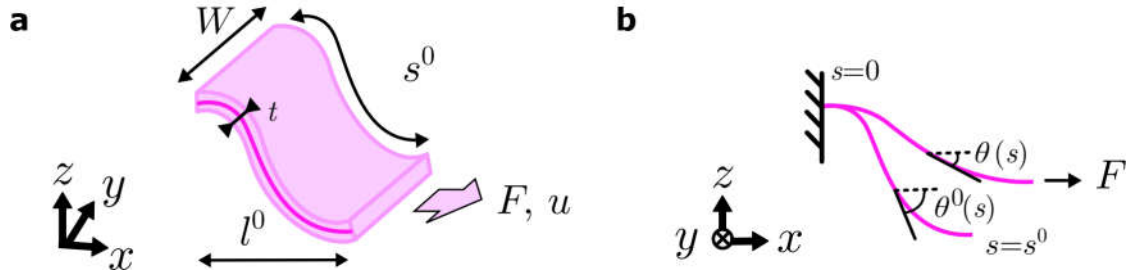

Fig. 5.24.: Elastica model of half a groove. **a,** The groove section has thickness t, width W, arc length s^0, and projected length l^0. **b,** The section's centroid, which determines its shape, is described by the angle θ^0 between the centroid's tangent and the $\hat{x}$-axis as a function of arc length s. Under a force F along the applied uniformly at the sheet's edge, the centroid deforms to $\theta(s)$.

The question remains how these values are related to the experimental samples' shape. We estimate the magnitude of the torsional and stretching stiffnesses of a real groovy sheet, assuming all bending takes place in the groove's fold (its curved section, see 5.2.1), while stretching takes place across the entire groove. Our experimental samples have a Young's modulus $E = 5 \pm 0.3$ GPa (see appendix A.6), width $W = 30$ mm, thickness $t = 23$ µm, flattened length $S^0 = 192.5$ mm, curved groove length $R\theta = 2 \pm 1$ mm, and number of grooves $N = 18$. We first estimate k_t of the groove fold using Winkler-Bach theory[159]. A curved sheet section of thickness t, depth W, and Young's modulus E, pre-bent to a radius of curvature R and subtending an angle θ, has a torsional stiffness

$$k_t = \frac{EWt^3}{12R\theta} \tag{5.23}$$

$$\approx 105 \pm 50 \text{ µN m} , \tag{5.24}$$

in the limit of reasonably small thickness, $\frac{t}{R\theta} < 1$. Secondly, we estimate k_t using linear elasticity. The stretching stiffness of half a flattened groove (corresponding to a single accordion bar) is, to first order,

$$k_s = \frac{EWt}{S^0/(2N)} \tag{5.25}$$

$$\approx 650 \pm 50 \text{ N/mm} . \tag{5.26}$$

While the shape-derived values for model parameters k_s and k_t match the experimentally measured values, this is mostly due to their large error margin. The accordion structure is a good toy model to understand a groovy sheet's stretching response, but it does not help us to quantitatively predict its stiffness; we need a different model for that.

We now discuss a predictive continuum model for groovy sheets. Previous work has shown that the entire groove deforms during stretching[160], and our assumption in the accordion structure above that hinging takes place near the fold may not be correct. We take this into account in a more realistic elastica model. We show below that the mechanics of these elastica grooves depends only weakly on the details of the groove's geometry.

The elastica geometry is shown in Fig. 5.24, which shows half a groove under a stretching force F and extension u. In the elastica framework, the angle profile $\theta(s)$ of the sheet

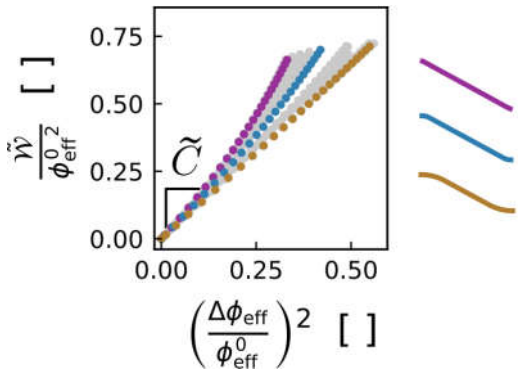

Fig. 5.25.: The mechanical response of sheets with various shapes can be rescaled to collapse on a curve. The dimensionless work $\tilde{\mathcal{W}}$ performed on a sheet section during stretching (Fig. 5.24) is shown as a function of the effective angle change $\Delta\phi_{\mathrm{eff}} = \phi_{\mathrm{eff}} - \phi^0_{\mathrm{eff}}$, where $\phi_{\mathrm{eff}} = 2\arccos\frac{l^0+u}{s^0}$. Both axes are rescaled by $(\Delta\phi^0_{\mathrm{eff}})^2$. The relation at small deformations is linear, with a slope $\tilde{C}$. Data for a broad range of groove shapes are shown (grey); several shape examples are highlighted in colour (see legend).

unit under an applied force F must minimize the sheet's bending-energy Lagrangian $\mathcal{L}$[108]:

$$\mathcal{L} = \frac{1}{2}D\int_0^{S^0}\left(\theta_s(s) - \theta^0_s(s)\right)^2 \mathrm{d}s - F\left[u - \int_0^{S^0}\left(\cos\theta(s) - \cos\theta^0(s)\right)\mathrm{d}s\right] \quad , \tag{5.27}$$

where $D = \frac{Et^3W}{12(1-\nu^2)}$ is the sheet's bending stiffness and ν its Poisson ratio. Angle profiles that minimize the energy obey the elastica equation

$$\theta_{ss}(s) - \theta^0_{ss}(s) - \frac{F}{D}\sin\theta(s) = 0 \ . \tag{5.28}$$

Numerical solutions found using the Mathematica software suite[161] yield the force-displacement response for grooves of widely varying geometries (see appendix A.8). Notably, the response across geometries can be rescaled to a master curve with fair accuracy, as shown in Fig. 5.25. There, we show the relation between the adimensional work $\tilde{\mathcal{W}} = \mathcal{W}s^0/D$ performed on the groove, and the square of the effective angle change $\Delta\phi_{\mathrm{eff}} = \phi_{\mathrm{eff}} - \phi^0_{\mathrm{eff}}$, where $\phi_{\mathrm{eff}} = 2\arccos\frac{l^0+u}{s^0}$ Both quantities are rescaled by the square of the rest angle ϕ^0. The data show that the relation between the plotted quantities is linear to good approximation, especially at small angle changes. In addition, the curves for widely varying groove shapes overlap to a fair degree. Defining an effective linear slope $\tilde{C}$ so that $\tilde{\mathcal{W}} = C\Delta\phi^2_{\mathrm{eff}}$, we find that its values lie between limiting values $1.25 < \tilde{C} < 1.5$ for *any* groove geometry (see appendix A.8). The relation between the slope $\tilde{C}$ and the experimentally measured torsional stiffness k_t is then found by combining our elastica result and Eq. 5.19:

$$\mathcal{W} = \frac{1}{2}k_t\Delta\phi^2_{\mathrm{eff}} \tag{5.29}$$

$$\tilde{\mathcal{W}} = \tilde{C}\Delta\phi^2_{\mathrm{eff}} \tag{5.30}$$

$$k_t = 2\tilde{C}\frac{EWt^3}{12(1-\nu^2)s^0} \tag{5.31}$$

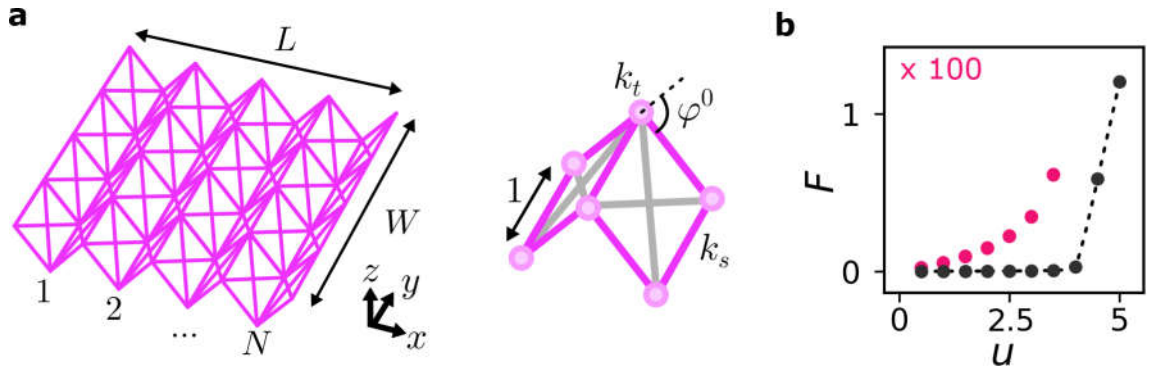

Fig. 5.26.: 3D simulation of groovy sheets. a, Left: discrete 3D model of a groovy sheet with N grooves, length L, and width W. Right: zoom-in of the model's unit cell. Springs with stiffness k_s and length 1 (purple lines) are connected in a square by torsional hinges (pink circles) of stiffness k_t and rest angles ϕ^0 along $\hat{\boldsymbol{x}}$ and 0 along $\hat{\boldsymbol{y}}$. Cross-braces springs (grey lines) of length $\sqrt{2}$ and resistance $0.1k_s$ stiffen the cell. **b,** Force F exerted by the structure under uniform extension u along $\hat{\boldsymbol{x}}$ across the grooves (compare Fig. 5.22). Data were obtained for a structure with $W = 9$, $N = 4$, $\phi^0 = 2.1$ rad, $k_s = 1$ and $k_t = 10^{-4}$ via a gradient descent algorithm. The force shows a soft hinge-dominated regime (red data points, y-scale magnified 100x) and a stiff stretch-dominated regime (black data points).

Substituting our sample's properties in Eq. 5.31, we find

$$k_t = 94 \pm 14 \text{ µN m} , \tag{5.32}$$

regardless of the exact groove geometry; comparing this value to our experimental measurement $k_t = 93 \pm 4$ µN m, we find an excellent agreement between our general elastica model and the real samples.

With the above models, we have explored the behaviour of groovy sheets under stretching across their grooves. Most significantly, we have shown that the sheet's initial response (that is, groove flattening) is dominated by a torsional stiffness that we can predict quantitatively within a small error margin, without needing detailed knowledge of the groove geometry.

5.4.5. A 3D sheet simulation

We now showcase a simple 3D model to simulate the reshaping behaviour of groovy sheets. In section 5.4.4, we showed that abstract models are useful tools to study the (qualitative) mechanics of groovy sheets. These models are easy to manipulate: quantities that are difficult to measure in experiments (for example, the total elastic energy contained in a deformed sheet) can be extracted straightforwardly. Here, we build on our results in the sections above to create a model mesh that mimics groovy sheet's in-plane stretching mechanics. We show that the model mesh matches the behaviour of a real groovy sheet to a good degree. Most importantly, we find that the modelled groovy sheet can sustain defects, and reshapes like a real sheet when a scar line of defects is introduced.

The 3D model mesh is shown in Fig. 5.26a, where the mesh unit cell is highlighted. Like the accordion model that we considered in Fig. 5.23, the mesh is built up out of linear springs of unit length and stretching stiffness $k_s = 1$, connected by torsional springs

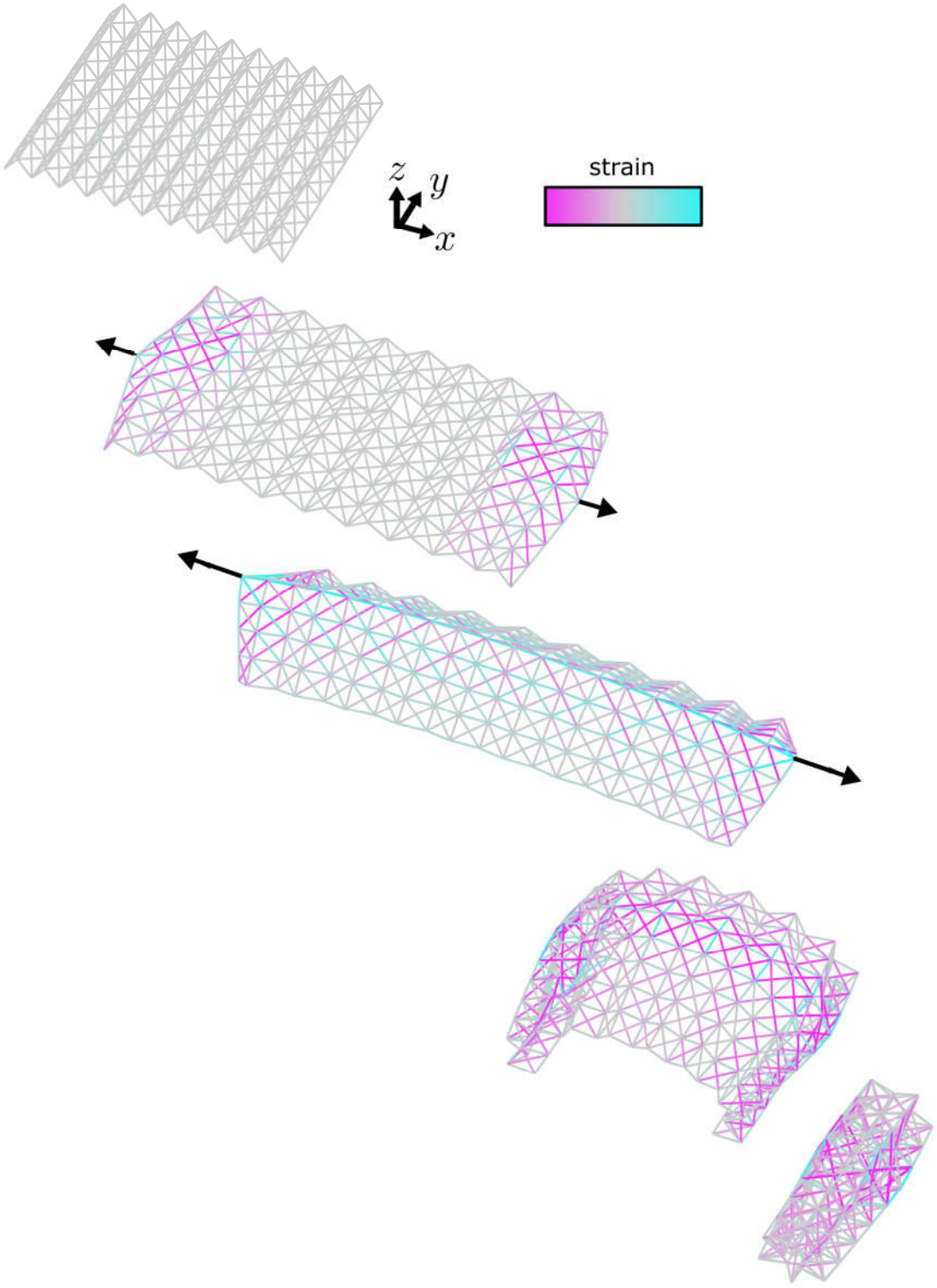

Fig. 5.27.: Simulated groovy sheets reshape via defects. Top to bottom: a modelled sheet with parameters $W = 9$, $N = 10$, $\phi^0 = 2.1$ rad, $k_s = 1$ and $k_t = 10^{-4}$ is extended by pulling at two nodes at its edges (black arrows). Defects snap through in the edge grooves and produce a local strain (colour bar). Further extension snaps the entire sheet and creates a scar line of adjacent defects. Subsequent relaxation lets the sheet curl up to a cylindrical equilibrium state with residual elastic energy.

with rest angle $\phi^0 = 2.1$ rad and hinging stiffness $k_t = 10^{-4}$ along the $\hat{\boldsymbol{x}}$-direction. Note here that we have chosen a (dimensionless) ratio between hinging and stretching stiffness $\frac{k_t}{(s^0)^2 k_s} \mathcal{O}(1e-4)$ similar to what we find in our experimental samples (see e.g. 5.21-5.22), in order to mimic real structures. Along the $\hat{\boldsymbol{y}}$-direction, neighbouring accordions are connected by additional linear springs as well as torsional springs with rest angle 0 rad. Cross-bracing springs are added with a stiffness $0.1k_s$ to mimic a real sheet's resistance to in-plane shearing (see appendix A.8). The model can be actuated by displacing its connecting nodes and letting the structure relax to equilibrium via a gradient descent method (appendix A.8).

We now show that the model's mechanics qualitatively match those of a real groovy sheet. First, Fig. 5.26b shows the force-extension curve of a mesh model under uniform stretching across its grooves. Like the experimental curves shown in Fig. 5.22, the force response shows two regimes: the first regime is dominated by hinge bending and the second by spring stretching. Secondly, Fig. 5.27 shows the mesh model's response under stretching at two point contacts on opposite sides of the sheet. The model mimics the behaviour of real sheets well (see section 5.1): initially, the entire mesh stretches out; at a critical strain, defects are formed at the sheet's edges; and finally, a scar line of aligned defects is created. When the scarred sheet is released to relax freely, it curls up into a cylindrical shape as expected.

In conclusion: our simple 3D mesh qualitatively matches the reshaping behaviour of a real groovy sheet. We will use this result to investigate energetic interactions between defects later, in section 5.6. Notably, the 3D model's success shows that groovy sheet's ability to sustain defects does not depend on pre-strain, pre-stress, or plasticity: it is a purely elastic effect.

5.5. Bistability of grooves

In section 5.1, we showed that defects pop in groovy sheets if they are stretched at two points along their two opposite edges. Here, we show that single defects can also be created by pushing down on a groove. We study their formation by experimentally popping through single grooves in their centres, and recording their force response and local shape (section 5.5.1). In section 5.5.1, we review previous research on similar structures to understand the origins of the stability of snapped-through grooves, and study the stabilizing effect of the groove's flat facets. Finally, section 5.5.2 investigates the introduction of a single defect at any position in a large groovy sheet. We show that the sheet's size influences when defects are stable, suggesting that defects do not only rely on local, but also on long-range deformations. We study these long-range effects as a function of sheet size, and show that single defects are *not* stable above a certain critical groove length, suggesting that the aspect ratio of grooves is a limiting factor in the design of shape-morphing groovy sheets.

5.5.1. Making single defects

Re-shaping a groovy sheet means snapping defects into it, for example via stretching (see section 5.1). But while snapping lots of defects at once by stretching the sheet is effective, it is also uncontrolled. Here, we show that defects can be popped through in a controlled way by indenting a groove from the top. We examine how the indentation force varies with the indentation depth, and find that the popping (and un-popping) of defects is a multi-step process that involves several snap-through events.

To study the force needed to pop a groove, we use the experimental setup shown in Fig. 5.28a. A groovy sheet is placed on two stiff support, 50 mm apart, under its central groove. The assembly is placed in an Instron 4900-series universal testing machine (UTM), modified to work horizontally. An indenter is fastened on the centre of the groovy sheet with a small ball magnet. The indenter is mounted in the UTM and attached to its translation stage and a 10 N-rated 2530-series load cell. Forces F on the indenter are measured as it moves by a displacement between $u = -0.5$ and 5 mm from the starting position at a speed of 0.1 mm/s. Moving the indenter far enough pops the groove.

Fig. 5.28b shows a typical force-displacement curve of a popping and un-popping sheet, with two distinct snap-through events (stars) in the popping stage. Data shown were obtained for a sample with $N = 5$ grooves, created with the mould-thermoforming method shown in section 5.2.2. The sheet has width $W = 100 \pm 5$ mm and thickness $t = 75$ µm. During the initial indentation (Fig. 5.28, upper curve), the force rises steeply as expected for any material, but then flattens off and becomes irregular. At a critical indentation depth, two audible snap-through events happen in short succession, and result in a popped groove with a defect. Performing the same experiment with the groovy, popped sheet reversed in the setup allows us to measure the un-popping force (Fig. 5.28b, lower curve). Comparing the popping and un-popping energies by calculating the area under the two curves, we find that popping costs 1.7mN m and un-popping 0.1mN m. In other words, the popped sheet's energy is 1.6mN m, and the barrier for reversal is more than

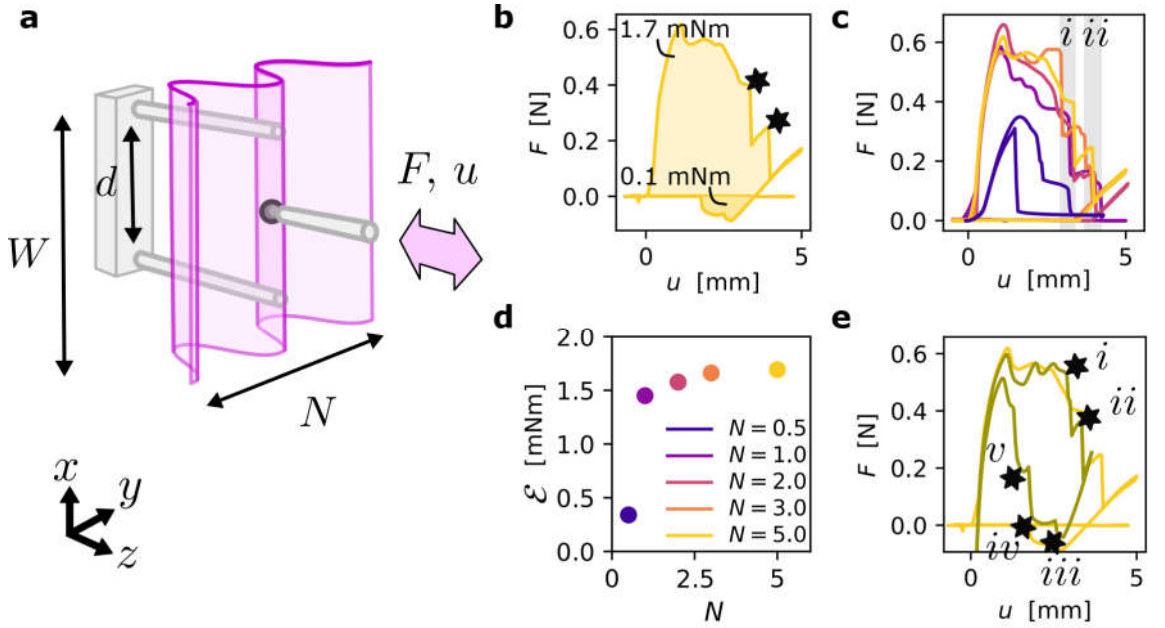

Fig. 5.28.: Popping a single defect. **a,** Experimental setup. An indenter (light grey) is stuck to the centre of a sheet (pink) with N grooves and width $W = 100 \pm 5\mathrm{mm}$ by a magnet (dark grey). The indented groove is held by two supports at distance $d = 50$ mm. Forces F generated by moving the indenter by a displacement u are measured by a universal testing machine. **b,** Force-displacement curve measured while popping (upper) and un-popping (lower) a sheet with $N = 5$ grooves. The onset is smooth, corresponding to slow indentation of the groove. Popping is complete after two audible snap-through events (stars) and $1.7\mathrm{mN\,m}$ of work has been done: releasing the indenter brings the force below zero. Un-popping the defect costs $0.1\mathrm{mN\,m}$. **c,** Popping of sheets with decreasing numbers of grooves: $N = 5$ to $N = 1/2$. Snap-through events i and ii (grey areas) and stable defects are seen for $N = 1$ to 5. At $N = 1/2$ (dark blue curve), the onset force is smaller, and the popped state snaps back. **d,** Work done during indentation, measured as the area under the force-displacement curves in (**c**), for $N = 5$ to $N = 1/2$. The work initially increases with N, then saturates. **e,** Force curve (green) measured when a sheet with 5 grooves is held by a magnet on each support. Forces are measured over the full range of displacements (free curve in yellow shown for comparison). Two snap-through events are seen while popping ($i - ii$), and three while un-popping ($iii - v$).

ten times as small: the bistable state lies in a fairly shallow energy well.

We investigate the importance of the number of grooves, N, in Fig. 5.28c-d. There, we show force curves for sheets of width $W = 100 \pm 5$ mm, but with different numbers of grooves: $N = 1/2$ to $N = 5$. Interestingly, there is no obvious quantitative difference between sheets with one or five grooves, or any number in between. The initial stiffness of all measured samples is similar; the curves show two snap-through events while popping, as expected (areas *i* and *ii* in Fig. 5.28c); and the final, popped state of the sheets is stable (that is, the force exerted by the indenter dips below zero). By contrast, the half-groove $N = 1/2$ is softer, needs a much smaller indentation force to snap through, and it is not stable in its popped state. These results imply that the influence of the number of grooves is only significant for very small values of N. This idea is supported by the results shown in Fig. 5.28d, where we show the work done on each sample during cyclic loading by measuring the areas under their force-displacement curves. The work done on a sample with $N = 1/2$ grooves is much smaller than the work done on samples with larger numbers of grooves. In addition, the work depends only weakly on the number of grooves, saturating to a plateau value as N grows. Thus, the behaviour of the popped central groove appears to only depend on its nearest-neighbour grooves.

To build an intuition for the snap-through events that happen inside the groove, we measure both the popping and un-popping response of a sheet with $N = 5$ grooves (Fig. 5.28c). We slightly modify the setup for these measurements: two extra magnets are used to attach the sheet to the two supports, which allows us to measure forces when the indenter pulls as well as pushes the sheet. The experimental force curve shows that indentation of the sheet produces two snap-through events (which we call *i* and *ii*) before the groove is popped through; during un-popping, pulling on the groove snaps the structure through three times (events *iii*, *iv*, and *v*).

Fig. 5.29 explores what happens to the local shape of a groove during popping and un-popping. Fig. 5.29a shows the experimental setup, while in Fig. 5.29b, we show qualitative sketches of the local mean curvature near the indenter as it is pushed and pulled. Blue and pink lines indicate positive and negative mean curvature, respectively (mountains and valleys, see legend). The sketches, based on observations, indicate that patterns of mean curvature in the groove are fairly regular and consistent across samples. Interestingly, snap-through events appear to be related to symmetry-breaking transitions in the curvature patterns. Snap-through transitions *i* and *ii*, which create a stable popped defect, both occur by annealing small regions of high negative curvature with adjacent valley grooves. Transition *iii*, which happens when the defect is un-popped, switches the defect's shape from a regular diamond to an asymmetric chevron. Finally, transitions *iv* and *v* create local regions of high negative curvature by detachment from the neighbouring valley grooves: they are the counterparts of transitions *i* and *ii*.

In short: defects in groovy sheets can be controllably popped in from the top. Our measurements show that defects do not feel much of the sheet beyond their neighbouring grooves; that they are created via multi-step snap-through events that are related to changes in the local groove curvature; and that defects live in a fairly shallow energy well, compared to their creation barrier.

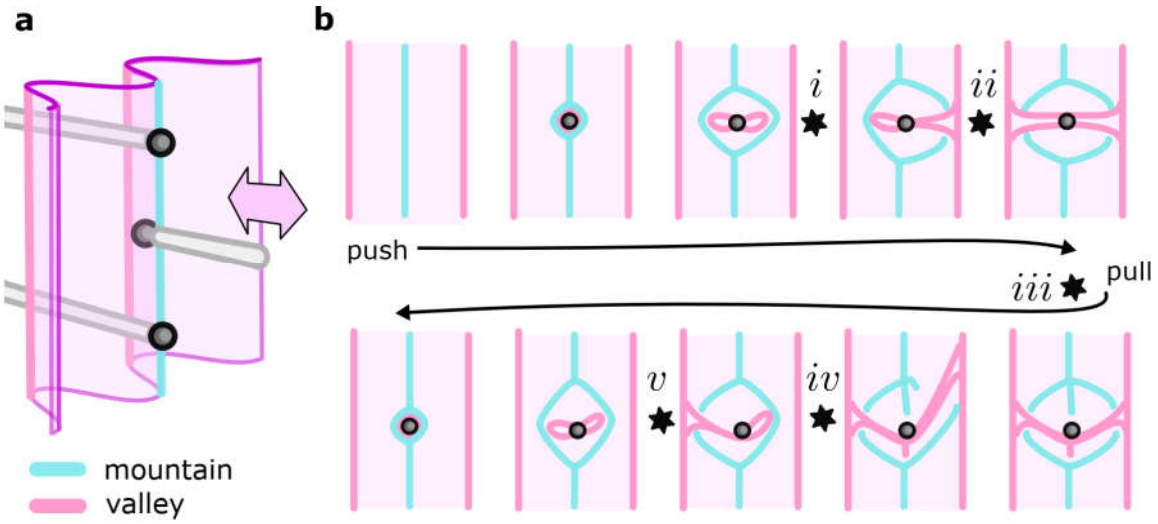

Fig. 5.29.: Local shape of a groove while snapping. **a,** Experimental setup as in Fig. 5.28, with the sheet being held by a magnet (dark grey) on each support. The indenter is pushed to pop a defect, and pulled to un-pop it. **b,** Sketches of the groove's mean curvature (blue and pink lines for mountains and valleys, see legend) during snap-through events $i - v$ shown in Fig. 5.28c. Top: pushing the groove produces a local mean curvature pattern. Regions of high mean curvature snap and disappear by annealing with a nearby valley groove (i and ii), resulting in a symmetric defect. Bottom: pulling the groove breaks the defect's symmetry (iii). Regions of high local curvature detach from neighbouring valley grooves in two snap-through steps (iv, v).

5.5.2. Sheet size dependence

In section 5.5.1 above, we showed that a defect can be popped into the centre of a sheet. For the particular sheet shape studied, we saw that this central defect is stable when the sheet has at least one groove. In addition, adding more grooves to the sheet did not significantly change the force needed to create a defect, implying that across the grooves (in the y-direction shown in Fig. 5.28a), interactions are weak: defects do not feel the neighbouring grooves much.

Here, we investigate the other direction: how do defects respond to their environment along the grooves (the x-direction in Fig. 5.28a)? We address this issue by studying the stability of single defects as a function of two variable sets, illustrated in Fig. 5.30a: the sheet size, set by the number of grooves N and the sheet width W; and the defect's position, set by its distance from the sheet's edges in terms of the number of grooves n and the edge width w.

As we show below, our findings confirm that the number of grooves does not impact defect stability much- except when defects are close to the sheet's edge. By contrast, the sheet width is very important: defects are sensitive to the length of the groove in which they live, and they are only stable if this length is neither too small, nor too large, but exactly right.

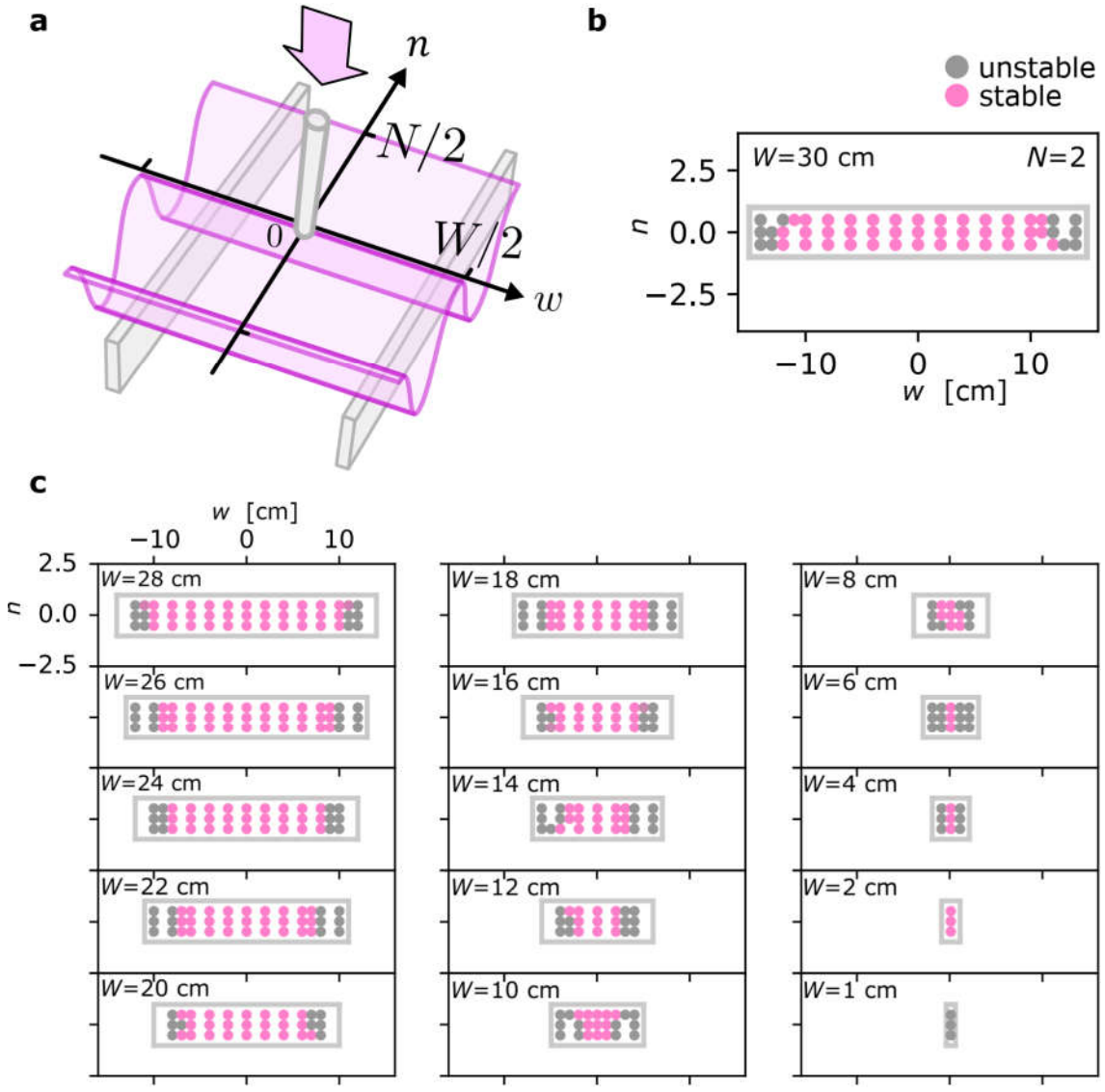

Fig. 5.30.: Probing stability of defect in a sheet. a, A sheet with N grooves, width W and thickness $t = 75\ \mu\mathrm{m}$ (pink) is placed on two supports (grey). The sheet is manually popped through with an indenter at various distances n across and w along the grooves away from the centre at $(w, n) = (0, 0)$. **b,** Stability of popped defects for a sheet with $N = 2$ and $W = 30\ \mathrm{cm}$. The sheet outline is indicated (grey box) in the (n, w)-coordinate frame. Pink and grey dots (legend) indicate where defects are stable and unstable, respectively. **c,** Stability results for $N = 2$ grooves and progressively shorter widths W are shown (scale: top left). Data were obtained by cutting to size and probing of a single sample. Only defects near the lateral edges are not stable.

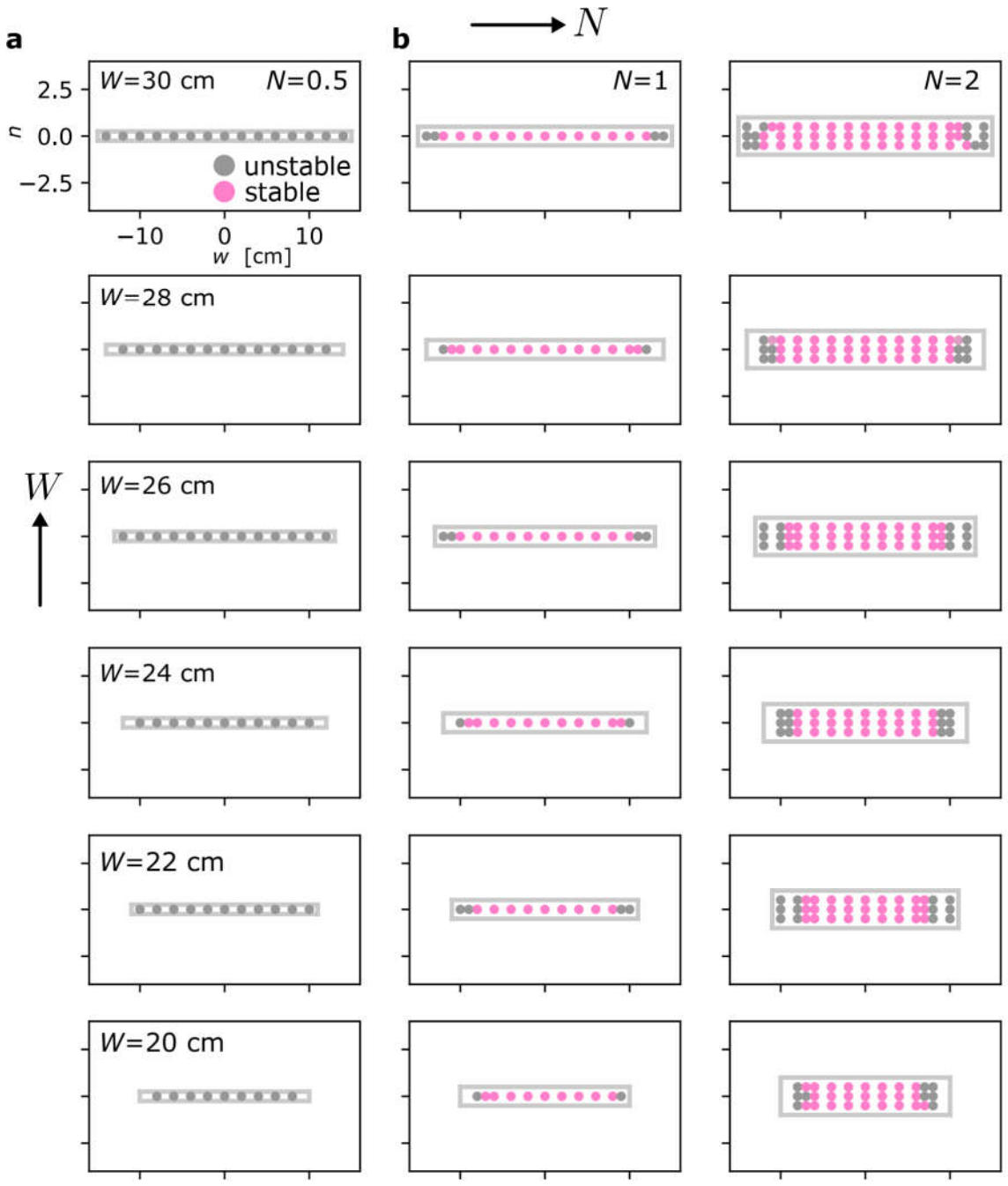

Fig. 5.31.: Defect stability depends on sheet size and location. Maps of defect stability are shown for sheets of systematically varied width W and number of grooves N. Top left: the sheet outline is indicated (grey box) in the (n, w)-coordinate frame. Pink and grey dots (legend) indicate where defects are stable and unstable, respectively. Scale is identical for each panel. Data in each column correspond to a distinct sample with $N \in [0.5, 1, 2, 3, 5, 7]$ grooves that is cut down progressively to a smaller width $W \in [30, 28, ..., 20]$ cm. **a,** Defects in narrow sheets with half a groove, $N = 0.5$, are unstable. **b,** For $N = 1, 2$, only defects near the lateral edges are unstable.

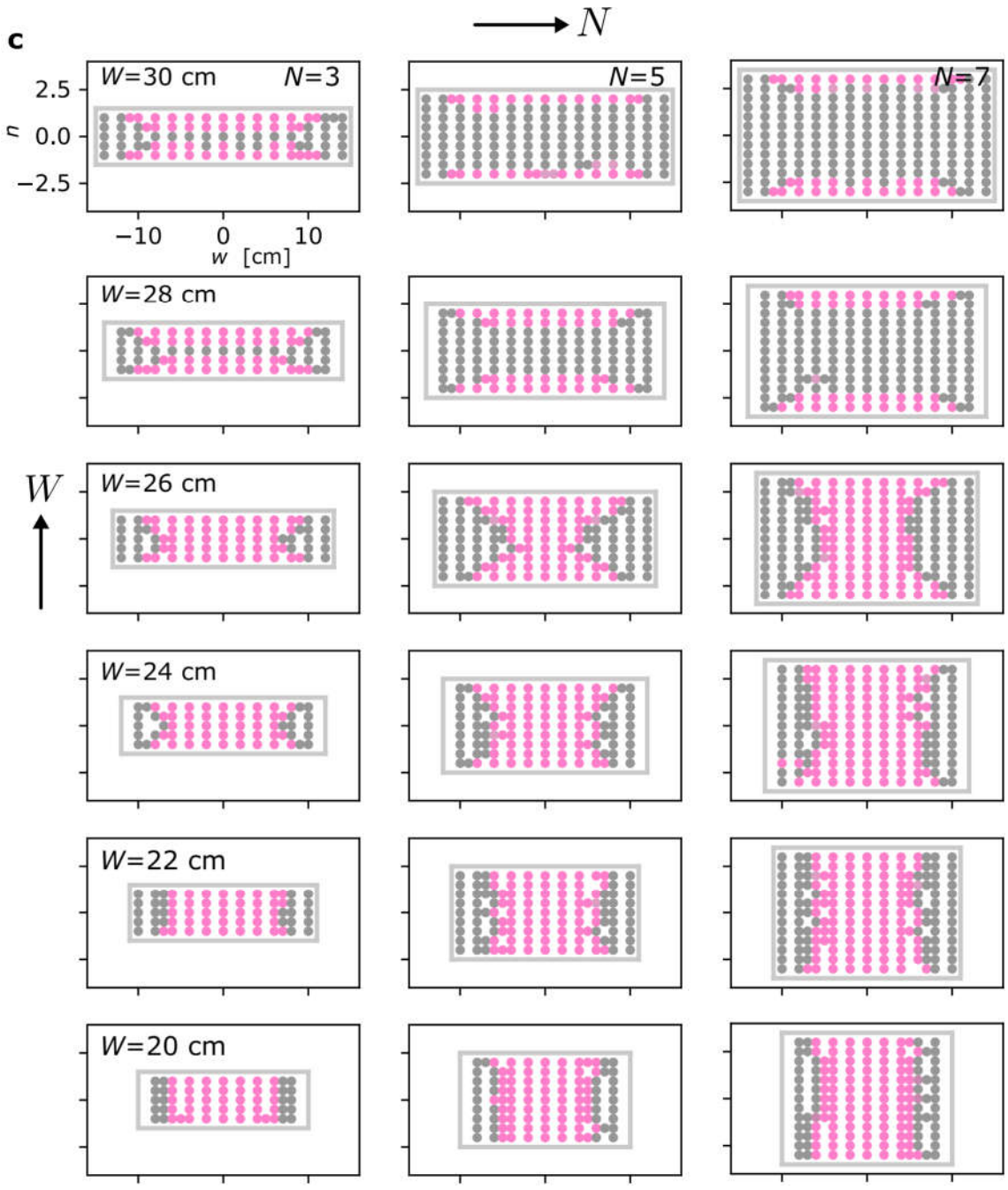

Fig. 5.31.: (continued) Defect stability depends on sheet size and location. **c,** For $N = 3$ and upward, defects near the lateral edges are unstable. In addition, sheets with a large width $W \geq 28$ cm show unusual behaviour: defects near the sheet centre are unstable. This difference between sheets with few and many grooves disappears, after a transition regime, at width $W \leq 22$ cm.

In Fig. 5.30a, we show our strategy to probe the stability of defects in a sheet of size N by W as a function of its position. The sheet is placed on two supports and a thin indenter is used to push the sheet down manually until no more snap-through events occur; the indenter's location is measured by distances n and w away from the sheet's centre. Fig. 5.30b shows typical stability results for a sheet of thickness $t = 75$ µm, $N = 2$ grooves, and width $W = 30$ cm. A top view of the sheet is shown, its edges indicated by

a grey outline. Dots on the sheet surface correspond to probed points: pink dots indicate that a stable defect has been created there, while grey dots indicate unstable points. Here, we take 'stable' to mean that a pop-through defect has been created successfully at this location, at least once, with a minimal lifetime of 10 seconds to account for viscous effects. Note that this definition includes points that may have been probed multiple times, producing a stable defect only once; our results may thus include false positives. Regardless, our results show a good consistency, as we show in Fig. 5.30c, where we show stability results of the sheet in Fig. 5.30b as it is gradually cut down to smaller and smaller widths W. Across the measurements shown, defects close to the lateral edges are unstable, while those near the centre are stable.

However, not every sheet supports stable defects near their centre, as we illustrate in Fig. 5.31. There, we show a grid of stability results for sheets with $N \in [0.5, 1, 2, 3, 5, 7]$ grooves (columns) that are gradually cut down to widths $W \in [30, 28, 26, 24, 22, 20]$ cm (rows). We first note that the stability results for each sheet are up-down and left-right symmetric to a good degree, consistent with our expectation that the sheet's geometry is uniform across each sample. The stability results fall into three classes, depending on the number of grooves; they are shown in panels 5.31a, b and c. First, Fig. 5.31a shows that sheets that are very narrow (only half a groove long, $N = 0.5$) do not support stable defects. While they can undergo snap-through transitions, they pop back to their starting shape, consistent with our mechanically controlled experiments in Fig. 5.28. Second, Fig. 5.31b indicates that defects in moderately narrow sheets (1 or 2 grooves long) are stable, except if they are too close to the lateral edges. Third, Fig. 5.31c illustrates that sheets with a larger number of grooves ($N = 3$, 5 and 7) show distinct behaviour. When such sheets are wide enough (above $W = 28$ cm), stable defects are only found where they are both far away from the sheet's lateral edges *and* close to the vertical edges. When the sheets are cut down to sufficiently small widths (below $W = 22$ cm), their behaviour reverts to the familiar pattern of defects that are only unstable near the lateral edges. In between these two widths, an area of stable defects near the sheet's centre appears in a typical hourglass-like shape that widens to a rectangular area at decreasing width W. Thus, the stability of defects in a sheet varies strongly with the sheet size and the defect location.

We condense the large amount of data in Fig. 5.31 in Fig. 5.32. We focus on the stability of defects at each sheet's centre (Fig. 5.32a, central cross), and on the width of the unstable regime near a sheet's lateral edges (Fig. 5.32a, arrows), which we call the unstable edge width u_w; u_w varies with the sheet's size, and with the minimal distance of a groove to the sheet's vertical edges, n_{edge}. Fig. 5.32b shows a stability diagram that shows whether or not a defect, created in the centre of a sheet with width W and number of grooves N, is stable (legend). Based on these results, we conclude that sheets can only support stable defects near their centre if they have enough grooves (here, $N > 0.5$) and are neither too narrow nor too wide ($1 < W < 28$ cm for this particular groove geometry).

Fig. 5.32c finally explores the unstable edges of our sheets: we show the unstable edge width u_w as a function of sheet width W for sheets with increasing numbers of grooves (left to right). u_w is measured for each groove of a given sheet, and colour-coded by the minimal distance of the groove to the sheet's vertical edges, n_{edge} (legend). Error bars correspond to the minimal and maximal measured values of u_w. Three features stand out: first, at small sheet widths, w_u grows proportionally to W. Second, at intermediate

sheet widths $W \approx 8$ cm, u_w plateaus to a constant value for grooves that are near the sheet's vertical edges. Finally, at large sheet widths, u_w increases with W (corresponding to the hourglass-shaped stability regimes in Fig. 5.31c); the magnitude of the increase is larger for grooves that are farther away from the sheet edge, but this trend seems to saturate beyond $n_{\text{edge}} = 2$. In essence, these results give us a design guideline for using sheets to make shape-shifting materials: sheets show *consistent* single-defect stability behaviour across their surface if they have a high enough number of grooves (here, $N > 3$) and their width lies in a goldilocks zone that is neither too small ($W \gtrsim 8$ cm), nor too large ($W \lesssim 20$ cm), but just right.

In summary: the stability of a single defect depends on the size of the surrounding groovy sheet. Specifically, the sheet width is important, more so than the number of grooves. The sheet energetics are complex, which gives rise to stable defects only in an intermediate range of sheet widths. This result has design consequences: sheets that are too big or too small may not support defects and may not be capable of shape-morphing-unless defects stabilize each other by *interacting* together.

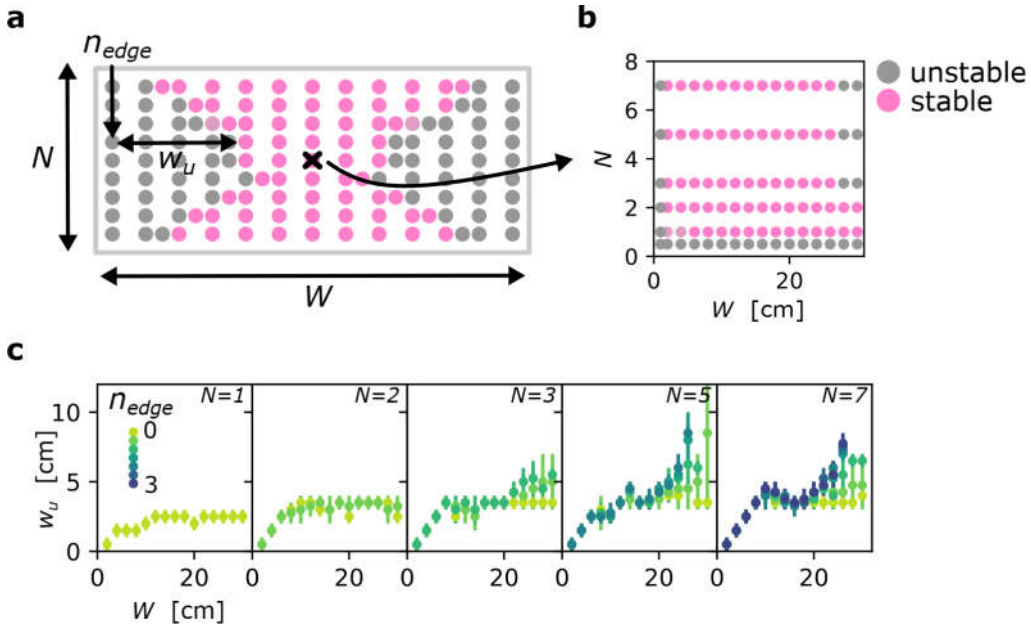

Fig. 5.32.: Stability of defects close to and far from the sheet edges. a, In a sheet of size N by W, defects are not stable if they are close to the lateral edges (legend: see **b**). We quantify an unstable edge width w_u that varies with the smallest distance to the edge along the grooves, n_{edge} (black arrows). The stability of defects at the centre (black cross) depends unambiguously on sheet size. **b,** Stability of central defects (legend) as a function of sheet size. Defects are unstable for sheets that are less than one groove long; defects are also unstable for sheets of too small or too large a width W. **c,** Unstable edge width w_u as a function of sheet width W is shown. Colours indicate the distance to the nearest edge along the grooves n_{edge} (legend). Data were obtained for sheets of various groove numbers N (left to right). The data show three effects. First, at small sheet size W, w_u increases proportionally with W. Second, w_u stabilizes to a plateau for grooves that are within 1 groove distance from the edge, $n_{\text{edge}} \leq 1$. Third, w_u increases from its plateau value for grooves farther away from the edge, $n_{\text{edge}} \geq 1.5$; the magnitude of the increase depends weakly on n_{edge}, appearing to saturate beyond $n_{\text{edge}} \approx 2$.

5.6. Interactions between defects

In this section, we explore interactions between multiple defects in a groovy sheet. Recall that in section 5.1, we observed the formation of straight *scar lines*. The fact that defects in adjacent grooves align in such scars provides strong evidence for the existence of interactions. First, scars are seen to run reasonably straight across the sheet, suggesting that defects in neighbouring grooves attract; second, the fact that scars are stable in rather large sheets, while individual defects are not (see section 5.5 above), further suggests a crucial role for interactions. We therefore probe the interaction of defect pairs, first experimentally (section 5.6.1) and then theoretically (section 5.6.2). To interpret our results, we study how defects affect a sheet's shape: interactions between defect pairs must ultimately be mediated elastically, via geometrical deformations. Based on experimental curvature measurements, we give an intuitive geometric explanation for the observed interactions and organization of defects in a groovy sheet (section 5.6.3).

5.6.1. Defects interact with their nearest neighbours

To explore the interactions between nearby defects, we first turn to qualitative experiments.

Our experiments start by creating a defect in the centre of a groovy sheet, using a small indenter. Importantly, defects are *mobile*: it may be moved along the groove at a low energy cost due to the high degree of structural symmetry along the groove direction. That is: barring edge effects, a defect produces a constant deformation (and thus strain energy) field, no matter where it is placed in the groove. Thus, in the ideal case, a defect is not prevented from moving by any *elastic* energy barrier: it is a Goldstone mode of the groovy sheet[162]. However, in practise, edge effects, dissipative losses and geometric irregularities tend to create small energetic barriers that cause defects to be pinned at certain preferred positions.

We use the central defect's mobility and pinning properties to probe defect interactions. A second defect is created in a nearby groove and allowed to glide freely to find a stable (possibly pinned) position. From this stable configuration, the second defect is moved relative to the central defect by applying a small guiding force with an indenter. When the guiding force is removed, the mobility of the second defect gives some information on how the pair interacts. We explore three scenarios for defects whose cores are close together: separated by 1/2, 1 and 2 grooves along x. (Fig. 5.33).

We start in Fig. 5.33a with two *positive* defects: they are made in the crests of two adjacent grooves, at a separation of $n = 1$ groove along $\hat{\boldsymbol{x}}$. Scar lines are made from chains of just such equal-parity defects, each separated by a single groove from its nearest neighbours. Fig. 5.33a-*i* shows the starting configuration. Two defects are made in a sheet of thickness $t = 50$ µm, width $W \approx 10$ cm and $N > 10$, fabricated with the corrugating method described in section 5.2.2. The sheet is visualized between crossed polarisers (see Fig. 5.15), which yields a colour pattern that depends on the sheet's local curvature and orientation. The defect pair is stable at a mutual distance $d \approx 0$ along $\hat{\boldsymbol{y}}$. One defect is moved to a small separation d (*ii*, black arrow), after which it spontaneously moves to an even larger stable distance d (red arrow). This repulsive motion is observed to be repeatable, though the stable distance varies somewhat. When the defects are brought

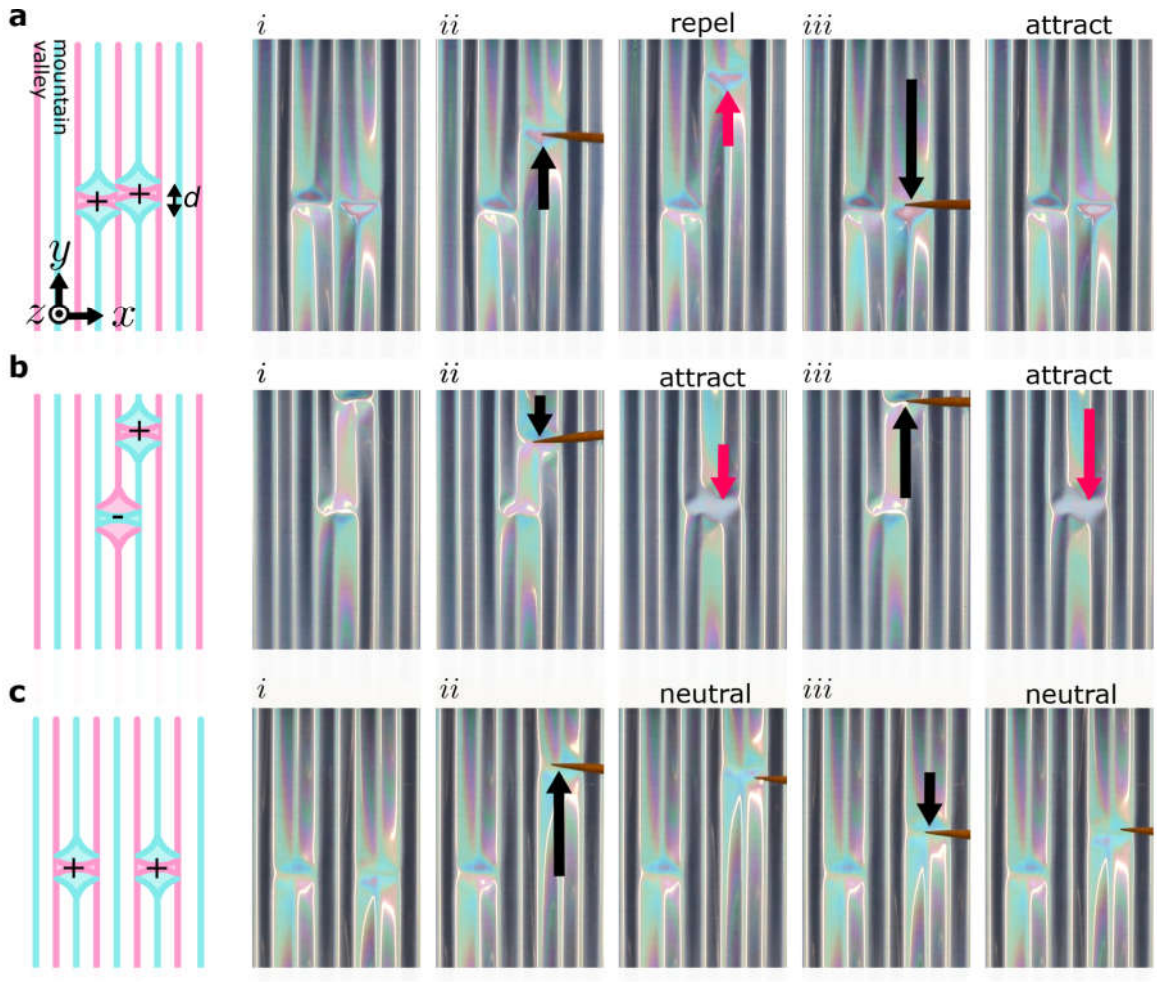

Fig. 5.33.: Defects feel their neighbours. **a,** Two positive (++) defects are introduced in the mountain folds of two neighbouring grooves (schematic, left) in a sheet with thickness $t = 50$ µm (photos, i) created with the moulding method of section 5.2.2. Moving one defect away from its neighbour with a small indenter (ii, black arrow) causes the defect to move farther spontaneously (red arrow). Joining the defects together (iii) creates a stable complex. **b,** A positive and negative (+-) defect are created in the mountain and the valley fold of one groove (i). Moving one defect toward its neighbour (ii) causes a spontaneous coalescence into a stable complex. This behaviour reproduces under repeated separation (iii). **c,** Two defects, whose cores are separated by two full grooves (i). Moving one defect does not result in spontaneous motion (ii, iii).

back together to $d \approx 0$, they remain stable (iii): there is a short-range attraction. Note that the defect's size is comparable to the groove wavelength λ (Fig. 5.8b). In terms of this typical size, the range of attraction between equal-parity defects lies below $d \approx \lambda$, while the repulsive effect is lost beyond $d \approx 4\lambda$, where defects come to rest.

Fig. 5.33b shows two defects made at a separation $n = 1/2$ along x. One *negative* defect is created in the valley of a groove, while the neighbouring crest sports a *positive* defect. Initially, the defects are stable at a distance $d \approx 4\lambda$ (i). When the positive defect is brought closer to its companion (ii), it moves spontaneously anneal into a defect complex with a separation $d \approx 0$. Forcibly separating the defects back to $d \approx 4\lambda$ does not prevent the complex from re-forming (iii), indicating that pinning effects may be responsible for the defects' initial stability in i. Thus, opposite-parity defects experience

a fairly wide range of attraction, at least up to $d \approx 4\lambda$.

Finally, we explore how defects interact when their cores are separated by two full grooves (Fig. 5.33c). A pair of equal-parity defects is created at a separation $n = 2$ along $\hat{\boldsymbol{x}}$ and a distance $d = 0$ along $\hat{\boldsymbol{y}}$ (i). Varying the defect distance does not lead to significant motion(ii, iii): there is no discernible interaction between the pair, implying that interactions between defects that are not directly adjacent are comparatively small.

The experiments in Fig. 5.33 show that defects in directly adjacent grooves interact with one another significantly. Their interaction is attractive at small distances compared to the groove wavelength. These findings are general: they reproduce across samples created with the fabrication methods shown in section 5.2.2. It is precisely this attraction between defects that allows for the creation of scar lines consisting of locked-in defect chains.

5.6.2. Defects attract and repel

The interaction between defects explored in Fig. 5.33 should be governed by defect-induced deformations of the groovy sheet, which cost work to create. While this elastic energy is challenging to measure experimentally, the simple computational model introduced in section 5.4.5 allows us to estimate the collective energy of a defect pair.

Fig. 5.34 shows our strategy. A small section of our model network is illustrated in Fig. 5.34a; a sheet with two grooves and its coordinate system are shown. The network consists of stiff Hookean springs (grey lines) with stretching stiffness $k_s = 1$, connected by soft torsional harmonic springs of stiffness $k_t = 1 \cdot 10^{-4}$ (see section 5.4.5). Lengths are measured by the model's cell spacing, l, which we set to unity. To get a sense of scale: elastic energies $\mathcal{E}$ in this system are thus measured in dimensionless units, where $\mathcal{E} = 1$ corresponds to the energy needed to stretch a single spring to twice its original length. This model allows us to estimate how much energy it costs to create defects; it is especially useful for comparing the energies of different defect configurations, such as a pair of equal-parity defects at various mutual distances.

In line with our experimental findings (recall Fig. 5.33), we study the energetics of a pair of equal-parity defects at various mutual distances (Fig. 5.34b). Starting from a sheet with $N = 2$ grooves and length $W = 20$, we introduce a defect at a position $d/2$ away from the sheet centre. The total elastic energy of the sheet, $\mathcal{E}_+$, can be calculated from the structure's deformed geometry. A second defect is then made at a distance d with respect to the first defect, ensuring that the defects are as symmetrically spaced as possible (see appendix A.10 for details). The total elastic energy of the sheet with its two positive defects, $\mathcal{E}_{++}$, is then calculated as a function of defect distance d.

The resulting energy curve is shown in Fig. 5.34c, as well as a reference curve for the energy $\sum \mathcal{E}_+$ needed to create either defect on its own. Several features stand out here, and we discuss them from large to small distances d. First, defects whose spacing is close to W are not stable, and no computational data could be obtained there. This is consistent with our experimental findings in section 5.5.2, where it was shown that defects cannot be created too close to a groove's lateral edges. Secondly, the total energy

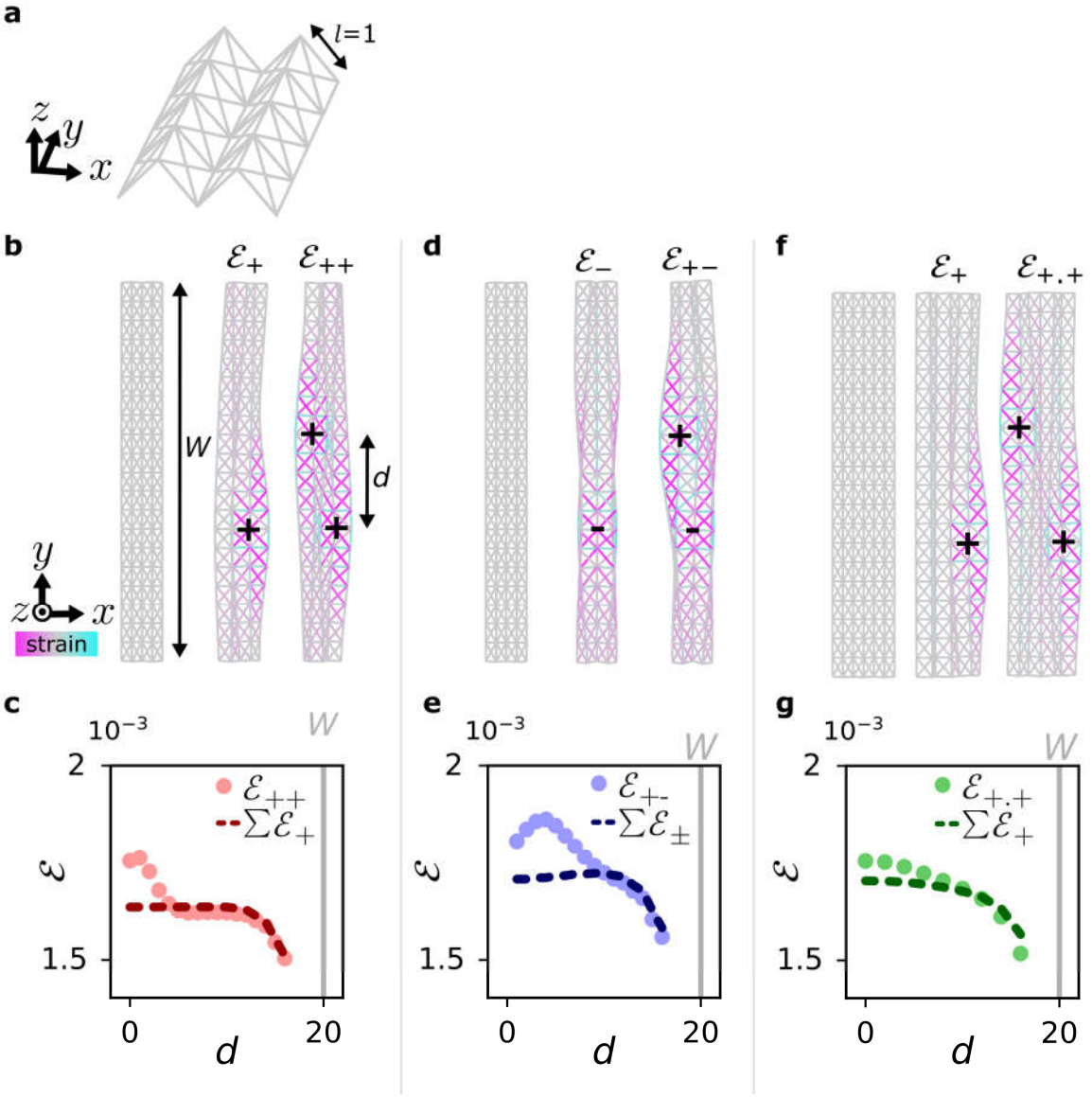

Fig. 5.34.: Defect interaction energies calculated with a computational model. **a,** Computational model of a groovy sheet, made with Hookean springs (grey bars) connected by torsional hinges. Sizes are measured in units of cell size $l = 1$. **b,** A sheet of of width $W = 20$ and $N = 2$ grooves (left) supports a positive defect (middle, marker) at distance $d/2$ from the sheet centre at an elastic energy cost $\mathcal{E}_+$. A second positive defect (right, marker) creates an equal-parity defect pair with spacing d at total energy cost $\mathcal{E}_{++}$. Strain in the network's springs is indicated for clarity (colour bar). **c,** Total energy $\mathcal{E}_{++}$ of the defect pair as a function of distance d (red circles). Baseline energy $\sum\mathcal{E}_+$ needed to create defects individually is shown for reference (red dashed line). **d,** A sheet (left) supports a negative defect in its central valley fold at energy $\mathcal{E}_-$ (middle). A positive defect in a neighbouring mountain fold at distance d increases stored energy to $\mathcal{E}_{+-}$ (right). **e,** Defect pair energy $\mathcal{E}_{+-}$ is shown, as well as the baseline $\sum\mathcal{E}_\pm$ (legend). **f,** Two positive defects separated by a groove are made in a sheet with $N = 3$ grooves (left to right) at total energy cost $\mathcal{E}_{+.+}$ **g,** Defect pair energy $\mathcal{E}_{+.+}$ and baseline $\sum\mathcal{E}_+$ (legend).

increases gradually as d shrinks, until an approximate plateau is reached at $15 \gtrsim d \gtrsim 5$. In this regime, the energy of the defect pair is nearly the same as the summed energies of the individual defects. Third, $\mathcal{E}_{++}$ increases between $5 \gtrsim d \gtrsim 1$, indicating a short-

range repulsion. Finally and crucially, the energy shows a small dip at $d \lesssim 1$. While our results are limited by the model's finite lattice spacing, these results are consistent with the experiments in section 5.6.1. That is, equal-parity defects attract at very short length scales compared to the typical groove width ($d < l$); they repel at intermediate distances($l < d < 5l$); and their interaction becomes very low after that ($d > 5l$), implying that in practise, secondary energetic effects (geometric irregularities, dissipation, and similar) may lead to defect pinning there.

We now investigate the long-range attraction of a defect pair with opposite parity with the strategy outlined above (Fig. 5.34d). The resulting energy $\mathcal{E}_{+-}$ and a reference curve $\sum \mathcal{E}_{\pm}$ as a function of defect distance d is shown in Fig. 5.34e. Interestingly, the energetic trend is similar to the positive-pair energy of Fig. 5.34c, indicating a loss of stability for defects too close to the groove's lateral edges, a lack of interaction at large distances, an intermediate-range repulsion, and short-range attraction. However, there are three differences. First, no plateau is visible, which we attribute to the finite width W of the sheet; however, the pair energy $\mathcal{E}_{+-}$ is nearly equal to the summed energy of individual defects, $\sum \mathcal{E}_{\pm}$, for $d \lesssim 12$. Second, the overall energy $\mathcal{E}_{+-}$ is higher than $\mathcal{E}_{++}$, which is due to the larger amount of (deformed) sheet material flanking the negative defect compared to the positive defects. Most importantly, consistent with the experiments in section 5.6.1, the regions of attraction and repulsion between the opposite-parity defects are much larger ($d \lesssim 4$ and $4 \lesssim d \lesssim 12$, respectively) than those between two equal-parity defects.

Finally, Fig. 5.34f-g explores how defects interact when they are separated by a full groove. A pair of equal-parity defects is created at an energy cost $\mathcal{E}_{+.+}$, which exhibits a small increase in energy at smaller values of d, indicating a repulsive effect. However, the energetic increase is significantly lower than for directly adjacent defects. Repulsive effects between spaced-out defects are thus comparatively small; here, too, secondary energetic effects can produce defect pinning in real groovy sheets.

In summary: our simple computational model shows that defects sense one another significantly only if they are separated by less than one full groove. We found that an equal-parity defect pair attracts at very small distances (compared to the typical groove size); repels at intermediate separations; and does not interact beyond that. A pair of opposite defects shows a similar interaction, but the pair senses each other over a larger range. Most importantly, both defect pairs exhibit short-range attraction. Thus, it is energetically favourable for a set of adjacent stable defects in a groovy sheet to align, which explains why defects form scar lines.

5.6.3. Interactions via curvature

Our simple computational model shows that defects interact. Given the simple ingredients of the model (elastic elements arranged in an accordion geometry), these interactions must be a product of geometrical effects that occur when defects are close together. However, the model's discreteness does not allow for an in-depth study of defect-induced deformations. Here, we turn instead to the 3D geometry of real sheets to study the geometric origins of defect interactions.

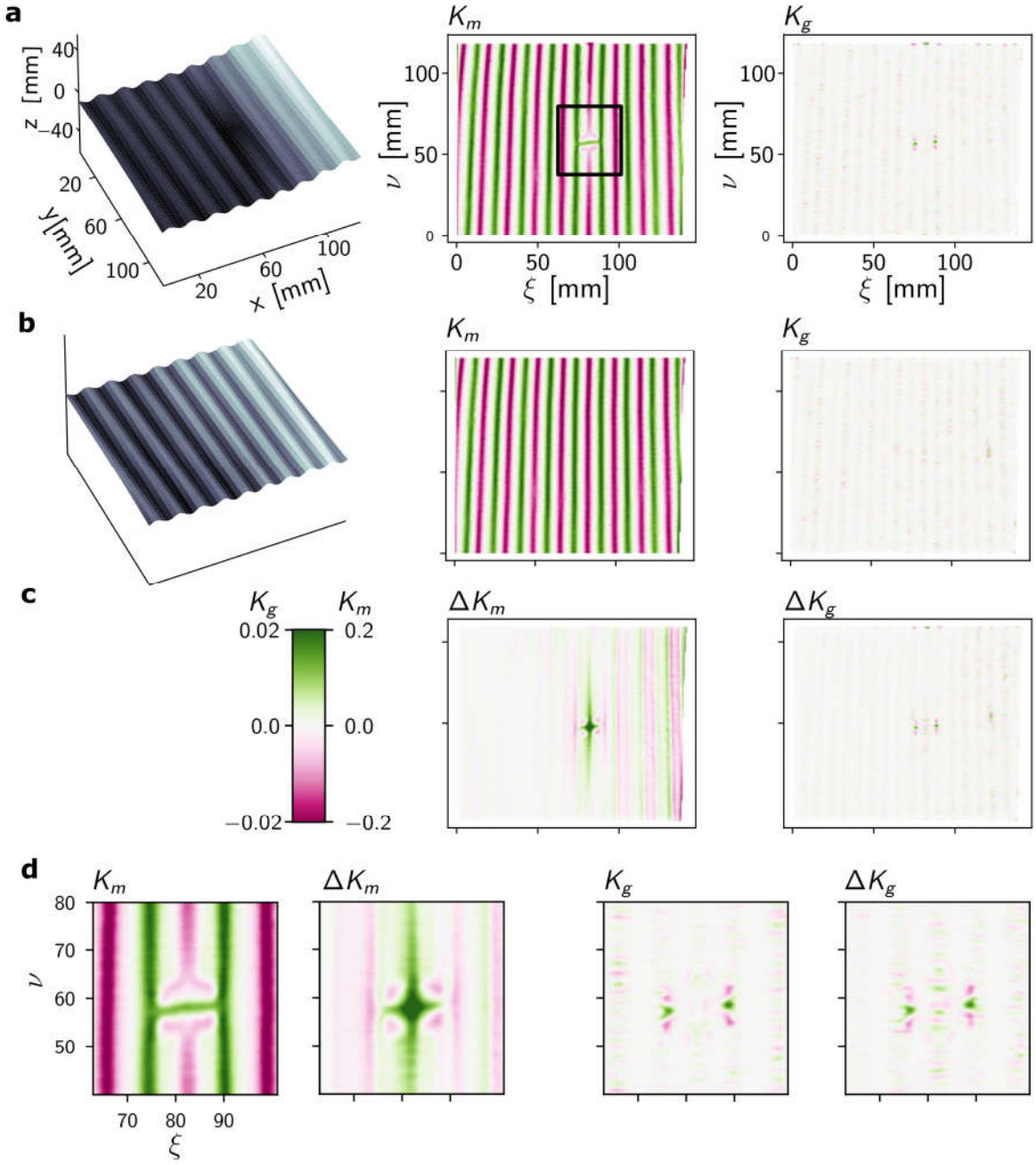

Fig. 5.35.: Defects affect both mean and Gaussian sheet curvature. a, Mean and Gaussian curvatures K_m and K_g (middle, right) in a groovy sheet with thickness 75 µm, width $W = 13$ cm, and $N = 10$ grooves (left; greyscale matches height z). Curvatures, obtained by numerical differentiation of the height profile, are shown as a function of local surface coordinates ν and ξ (colour bar). **b,** Mean and Gaussian curvatures (middle, right) in a groovy sheet with no defects (left). **c,** Difference between mean and Gaussian curvatures, ΔK_m and ΔK_g, of groovy sheets with and without a defect. Long-range changes in mean curvature, as well as localized changes in Gaussian curvature are seen. **d,** Zoom-in of curvatures and curvature differences in the presence of a defect (black box in **a**).

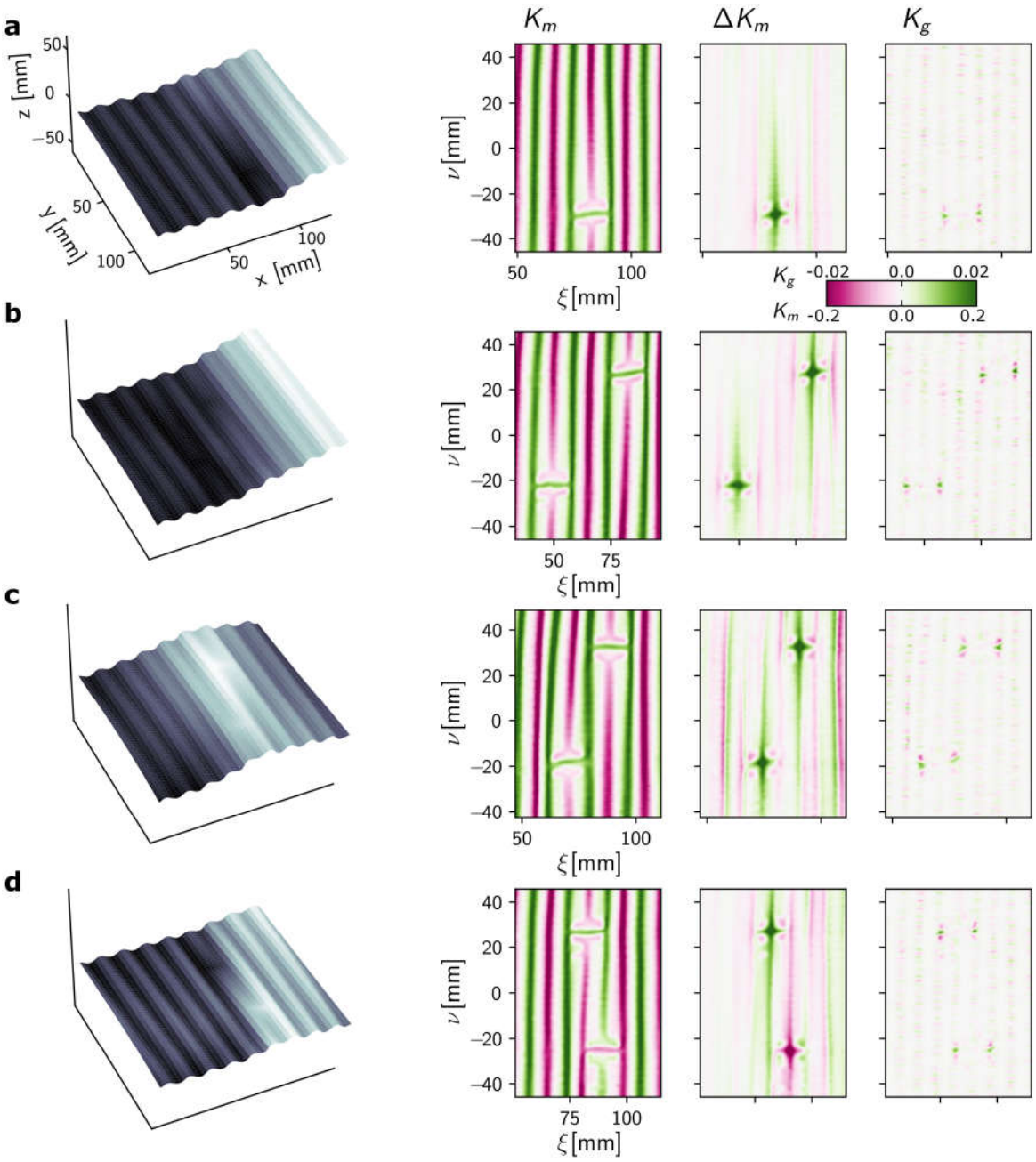

Fig. 5.36.: Defects pairs at large distances do not interact. **a,** Mean curvature K_m, deviation ΔK_m and Gaussian curvatures K_g and K_g (right) in a groovy sheet sporting one defect. Sheet details as in Fig. 5.35. Curvatures are shown as a function of local surface coordinates ν and ξ (colour bar). **b,** Mean and Gaussian curvatures in a groovy sheet with equal-parity defect pair at a core separation of two grooves along xi and at distance 5 cm along ν. **c,** Equal-parity defect pair at distance 5 cm and core separation of one groove. **d,** Opposite-parity defect pair at half a groove core separation and 5 cm distance. Curvature patterns for pairs do not differ from those of single-defects.

The energetics of real groovy sheets are governed by bending and stretching deformations, which we quantify as follows. Bending deformations produce a *mean curvature* $\mathbf{K}_m$. For example, a sheet rolled into a cylinder with radius a goes from zero mean curvature to $\mathbf{K}_m = a$. Thin sheets resist such deformations with a typical bending stiffness $k_{\text{bend}} = \frac{Et^3}{12(1-\nu^2)}$ [108]. Contrariwise, local stretching deformations produce a *Gaussian cur-*

vature $\mathbf{K}_g$ that may be positive or negative. Typical examples of such local stretching is dimpling of a flat sheet into a spherical shell (from zero to positive Gaussian curvature) or into a saddle-shaped section (from zero to negative Gaussian curvature). Changes in Gaussian curvature are resisted by the sheet with a stiffness $k_{\text{stretch}} = \frac{Et}{12(1+\nu)}$ [108]. The different thickness-dependence of the bending and stretching stiffnesses show that stretching is more energetically costly than bending for thin sheets. As a consequence, in thin sheets, stretching deformations are often much more localized than bending—crumpling in paper being a typical example—though exceptions do exist[163–166]. On a practical note: *uniform* stretching deformations do not produce either mean or Gaussian curvature; however, given the high energy cost of uniform stretching and the lack of its experimental observation in groovy sheets with defects, we do not consider it here. Together, the mean and Gaussian curvatures describe how a (groovy) sheet curves in space, and how it deforms in the presence of defects.

Thus, measuring a groovy sheet's curvature with 3-D scans (section 5.3.2) allows us to understand where defect-induced bending and stretching deformations take place. Below, we compare how these deformation distributions look for different defect pair arrangements. Our data suggest that defect pairs experience long-range interactions mediated by bending deformations, while stretching deformations play an important role at close quarters. We propose that stretching deformations are responsible for the short-range attraction between equal-parity defect pairs, explaining the formation and stability of scar lines of contiguous defects in groovy sheets.

To study the geometric interactions between defects, we first look at a reference scenario: a groovy sheet with one defect. Fig. 5.35a shows the height profile of a sheet with $N = 10$ grooves, width $W = 13$ cm and thickness $t = 75$ µm, produced using static thermoforming (section 5.2.2). A single defect has been popped into the sheet, away from its edges. The mean and Gaussian curvatures, K_m and K_g, are calculated from the scanned height profile $z(x, y)$ by calculating its discrete derivatives (section A.11). Via comparison with the curvature of a sheet with no defects (Fig. 5.35b), the differences in Gaussian and mean curvatures, ΔK_m and ΔK_g, are calculated across the sheet surface and shown in Fig. 5.35c. The following features stand out. First, the defect affects mean curvature along its groove (direction ν) over several centimetres; a larger span than across its groove (direction ξ), where differences in mean curvature become indistinguishable from noise over the span of about one groove. This limited effect of defects beyond their nearest neighbours is consistent with our experimental and computational results in the previous sections. Second, the Gaussian curvature shows a focussed peak around the defect location. While the Gaussian curvature's spatial pattern reproduces across many samples, its measured magnitude fluctuates significantly. We attribute these fluctuations to the use of squares of higher-order discrete derivatives during its calculation. Thus, we should compare its spatial distribution rather than its magnitude between different measurements. Inspecting the curvature more closely via the zoom-in in (Fig. 5.35d), we see that the defect produces a regular, reflection-symmetric change in mean and Gaussian curvature.

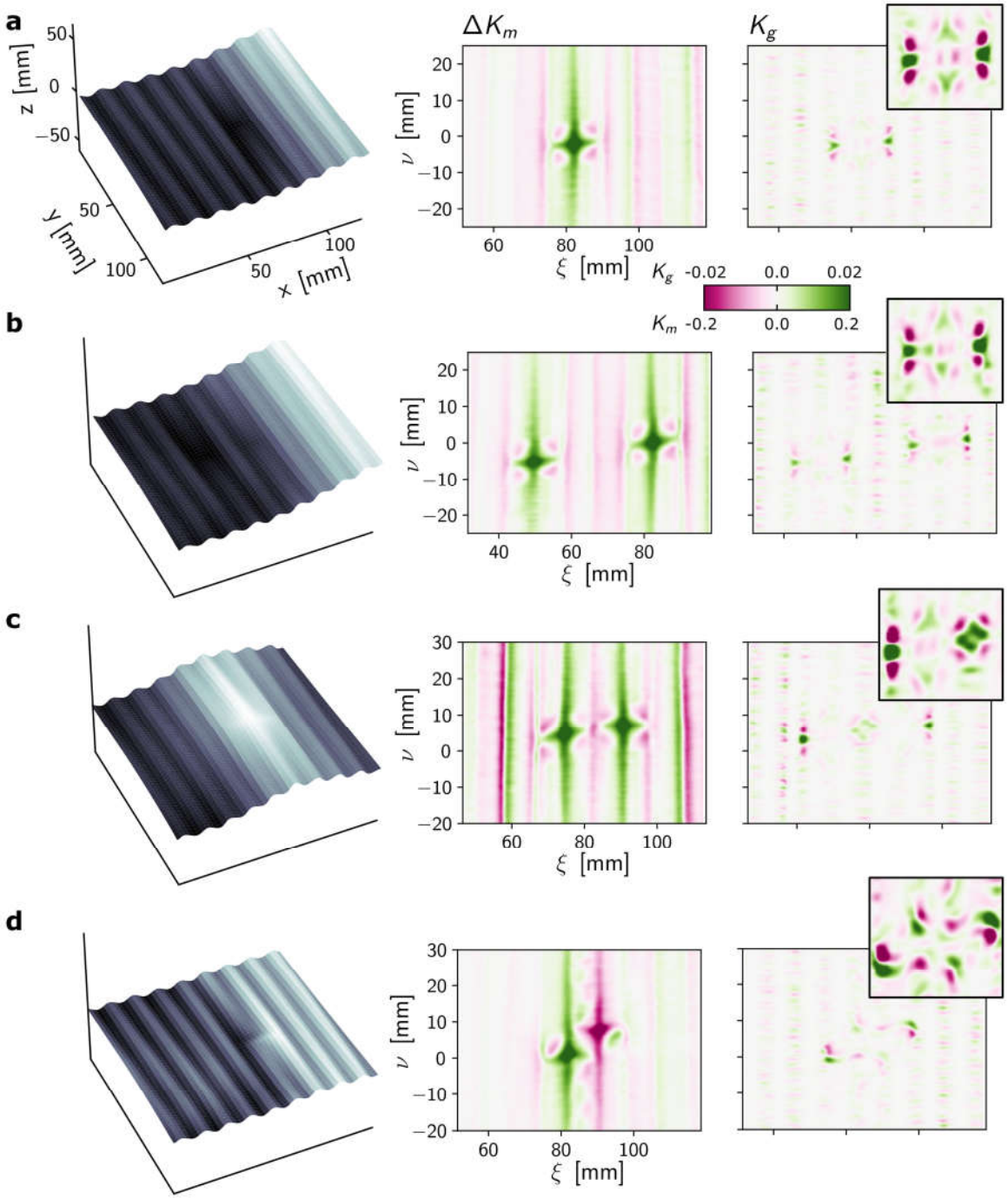

Fig. 5.37.: Defects pairs at small distances interact. **a,** Mean curvature change and Gaussian curvature, ΔK_m and K_g (middle, right), correspond to bending and stretching deformations in a groovy sheet with one defect. Sheet details as in Fig. 5.35. Inset: colour-saturated zoom-in of defect locus to highlight K_g distribution. **b,** Bending and stretching deformations for an adjacent, equal-parity defect pair at a distance of 0 cm along ν (and two grooves core separation along ξ). Deformation fields match those of isolated defects. **c,** Deformations for an adjacent equal-parity defect pair at a core separation of one groove. Bending and stretching between the pair does not match single-defect deformations. **d,** Deformations for an adjacent opposite-parity defect pair at half a groove core separation. Bending and stretching around the pair differs significantly compared to a single defect.

Most notably, differences in mean curvature are centred on the defect's core groove, while differences in Gaussian curvature show up as small, alternately positive and negative stretching patches in the grooves directly *next* to the defect. We now investigate whether these off-centre stretching deformations could be responsible for inter-defect interactions. We first look at various defect pairs at a large distances, and show that their curvature distributions look similar to those of isolated defects. By contrast, we then show that the curvature distribution for defect pairs at small distances differs significantly.

Fig. 5.36 shows curvature distributions of a sheet sporting defect pairs at a large mutual distance d along sheet direction ν. For reference, Fig. 5.36a shows a sheet with a single defect; its mean curvature K_m; its mean curvature deviation ΔK_m with respect to the undeformed sheet; and its Gaussian curvature K_g. Fig. 5.36b–d show the same curvature measures for three defect pairs. In order, we show: an equal-parity defect pair whose cores are separated by two grooves; an equal-parity defect pair at a core separation of one groove; and finally, an opposite-parity defect pair separated by half a groove. Inspection of K_g and ΔK_m shows that each defect produces a local curvature distribution that is qualitatively indistinguishable from that of a single defect, supporting our experimental and numerical observations that defects at large separations do not interact.

However, the curvature behaves differently when defects are close together, as illustrated in Fig. 5.37. Here, too, Fig. 5.37a shows a groovy sheet with a single central defect for reference; the sheet's bending and stretching deformations (ΔK_m and K_g) away from its initial state are included. Zoomed-in insets of Gaussian curvatures near the defect locus are shown; the colour map for these insets is chosen with tighter limits for larger visual contrast, highlighting the different curvature distributions. High-frequency noise is observed in the Gaussian curvature along direction ν, which we attribute to scanning errors (the noise matches the scan fringe frequency of 1.6 mm, see section 5.3.2).

Fig. 5.37b shows an equal-parity defect pair with a core separation of two grooves. Interestingly, the sheet deformations around each defect appear similar to those of isolated defects, consistent with our previous observation that such defect pairs do not interact strongly.

Fig. 5.37c also shows an equal-parity defect pair, with a smaller core separation of one groove. Here, the deformation field around the defects is different: the mean curvature of the groove right between the defect pair changes significantly, signalling local groove flattening. In addition, the defects' Gaussian curvature peaks at the central groove merge into a complex in a diamond pattern, where the amount of curvature appears to be less than for independent defects. Thus, while bending deformations appear to increase, stretching deformations may be reduced. We hypothesize that the competition between increased bending and reduced stretching in the samples studied here results in a net energetic benefit when the two defects are aligned.

Finally, we consider an opposite-parity defect pair with a core separation of half a groove in Fig. 5.37d. The defects' bending and stretching deformations show rather different distributions compared to isolated defects. Two features stand out. First, the opposing bending deformations of the two defects (quantified by ΔK_m) appear to be 'slotted' into place in a way that preserves their bending distribution symmetry. By inspection, increasing the defects' mutual distance breaks this symmetry, suggesting an

increased bending energy cost at larger distances. Second, the stretching distribution (K_g) of the two defects merges into a complex. Notably, the stretching pattern of one defect's core merges with the off-centre stretching of the other. Separating the defects thus requires the creation of more stretching patches, at an energetic penalty. Both features are consistent with the mid- and short-range attraction (mediated here via bending and stretching, respectively) that was observed experimentally and computationally.

The groovy-sheet deformation fields studied above show that interactions between defects are mediated by bending and stretching, visible as changes in mean and Gaussian curvature. Defects produce bending deformations at medium range across and along grooves, respectively (compared to the typical groove size). By contrast, stretching deformations are highly localized within half a groove from the defect's core. This means that bending-mediated interactions play a role over medium-range distances, while stretching-mediated interactions become significant if the defect pair's cores are close together. While the exact merging of defect's deformation fields at short distances may be complex, the outcome is simple: defect pairs in adjacent grooves show short-range attraction. In summary: defects attract at close range, and this interaction allows scar lines of adjacent, equal-parity defects to be formed in large sheets.

5.7. Shaping groovy sheets with scar lines

Defects in groovy sheets organize to form scar lines, as we discussed above. In the previous sections, we showed that short-range, geometrically-driven attraction between defects lies at the heart of scar line formation. Here, we explore the natural next question: *how do scar lines reshape groovy sheets?*

Figure 5.38 revisits some of the complex groovy sheet shapes first shown in section 5.1. While Fig. 5.38a–c showcase samples with intricate shapes due to their various scar line configurations—short and long, diagonal and straight—Fig. 5.38d shows our starting point: a groovy sheet with a single central scar line, orthogonal to its grooves. The resulting shape appears geometrically straightforward: the sheet is rolled up into a cylindrical shape, distended near the scar line. In other words: isolated scar lines orthogonal to the sheet's grooves lead to geometrically simple shapes.

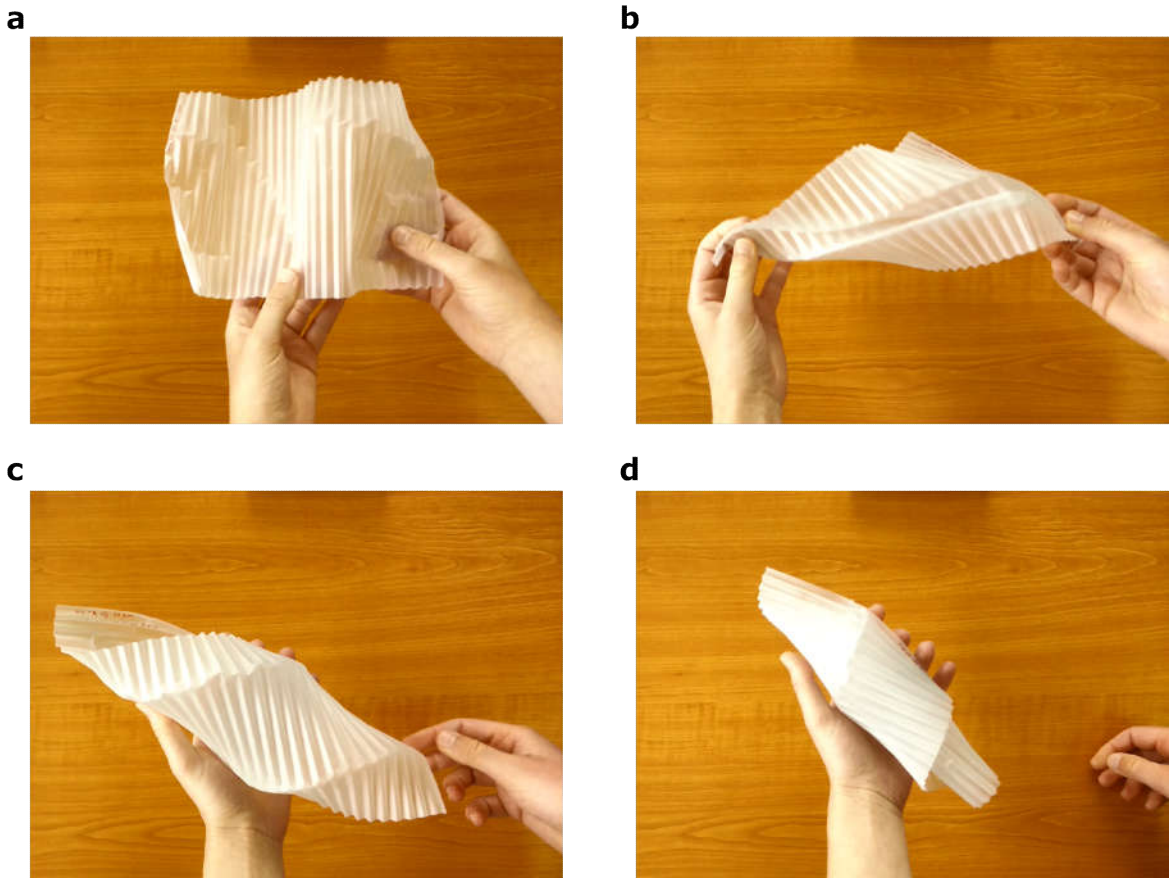

Fig. 5.38.: Scars reshape groovy sheets. Several scar configurations of a groovy sheet (100 µm thick, fabricated using the dynamic forming method described in section 5.2.2) are illustrated. **a,** A multitude of small scar lines, each spanning several grooves, produce a rough landscape with hills and dips. **b,** Three alternating scar lines create a slit surface. **c,** Spiralling shape formed via two equal-parity scar lines. **d,** A single scar line forces the sheet to roll up.

In this section, we therefore systematically study the reshaping effect of scar lines, starting with a single scar in section 5.7.1. We discuss a geometric argument that shows

why a scar line produces a rolled sheet shape, and show experimental data to support this. In addition, we show that small sheets (with a small width W) roll, while larger sheets undergo a symmetry-breaking transition that produces both a figurative and literal twist in the sheet shape. We argue in section 5.7.2 that a sheet section with a single scar line can be viewed as a puzzle piece: different configurations of scar lines can be obtained by tiling and connecting such puzzle pieces. We show that simple geometric arguments are not always sufficient to predict the resulting sheet shapes, especially when parallel scar lines are present. The shaping effect of multiple parallel scar lines is subsequently explored in section 5.7.3, where we present sheet shapes resulting from two scar lines. We show experimentally that the sheet shapes fall into two distinct categories: twisted cylinders and helicoids, whose detailed geometry is dominated mostly by the distance between scar lines. Finally, we conclude in section 5.7.4 by briefly discussing a way to model groovy sheet shapes as ruled surfaces.

5.7.1. A single scar

Here, we study the shaping effect of a single scar line. To keep things simple, we stick to scar lines placed centrally in a groovy sheet, orthogonal to its grooves. Fig. 5.38d above illustrates what happens next: the scarred sheet reshapes into a roll. To explain this behaviour, we first consider the effect that a defect has on a single groove, and then discuss how to tile defected grooves together to form a groovy sheet with a single scar line in Fig. 5.39. After this purely geometric consideration, we then measure actual rolled sheet shapes experimentally in Fig. 5.40. We will show that the rolling radius increases with the sheet's size, and present geometric arguments for this behaviour in Fig. 5.41; in addition, large sheets show twisting as well as rolling, which we capture qualitatively in a simple energetic model in Fig. 5.42. Together, our findings show that scarred sheets roll and twist; and that the amount of rolling and twisting depends on the sheet's initial geometry, as well as its elastic behaviour.

We start in Fig. 5.39 with a purely geometric model of a scarred sheet. First, Fig. 5.39a-b shows a single groove in which a defect is popped. The defect locally flattens the groove's natural curvature, and folds the groove orthogonal to the flattening direction. Thus, while the groove's footprint (the polygon spanned by its corners) is initially rectangular, the defect causes the rectangle to stretch and fold along its midline. As a result, the groove's footprint becomes a *trapezoidal fold* that consists of two isosceles trapezoids that meet at their bases at a shallow angle (Fig. 5.39b). The trapezoidal fold's geometry is set by its base length and base angle, as well as its folding angle. There is a unique way to tile our trapezoidal folds in space without distorting them, as shown in Fig. 5.39c: they can be stacked together into a rolled shape by mirroring the folds in the plane spanned by their edge points (pink dots in Fig. 5.39c). This suggest that the scarred sheet's rolling is, to first order, governed purely by geometry.

In practise, rolling of groovy sheets in the presence of a single scar line is observed consistently across a wide range of groove geometries and sheet sizes, although sheets do not support single scar lines at widths that are either too small or too large (reminiscent of our findings in section 5.5.2). Notably, we expect the precise geometry of the roll—its radius of curvature—to depend on the elastic behaviour of the sheet: after all, there is a competition between groove flattening and folding at the defect locus, and a competition

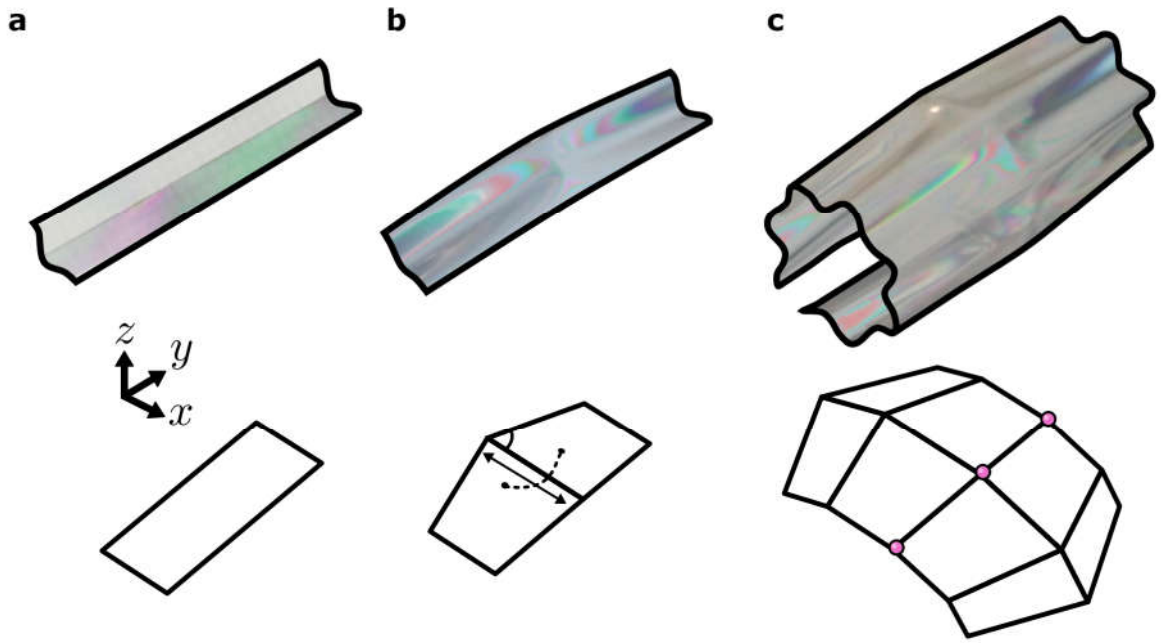

Fig. 5.39.: Geometry of a single scar line. **a,** A single groove (top, cropped and outlined image of a real sheet viewed between crossed polarisers) has a rectangular footprint (bottom). **b,** A defect stretches and bends the groove. Its footprint now consists of two opposing trapezoids at a mutual angle (dashed arc): a trapezoidal fold. Its geometry is set by the base length and angle of the trapezoids (arrow, solid arc). **c,** Tiling grooves with defects corresponds to tiling trapezoidal folds. There is a unique configuration, obtained by mirroring folds in the plane spanned by their edge points (pink dots), that does not distort the folds. This configuration produces a rolled structure.

between bending and twisting deformations away from the scar line. Thus, while the geometric picture is a useful qualitative tool to explain rolling, experiments are needed to quantify the exact sheet shape.

The exact rolling shape of groovy sheets can indeed be measured experimentally with photography and 3D scanning (recall sections **??-??**, and Figs. 5.16 and Figs. 5.20 in particular). We report our shape measurements in Fig. 5.40. Besides helping quantify sheet rolling, the data show that wide sheets twist as well as roll, as we will discuss below.

First, Fig. 5.40a illustrates the sheets' experimental parameters: thickness $t = 75$ µm, $N = 10$ grooves, and a variable total width $W \in [2, 30]$ cm. Scar lines are introduced in the centre of the sheet at a distance $W_f = W/2$ from the free edges. We explore two sheet types with deep and shallow grooves, fabricated using static and dynamic thermoforming respectively (see section 5.2.2). The deep grooves have wavelength $\lambda = 12.7 \pm 0.5$ mm, amplitude $A = 4.3 \pm 0.5$ mm, arc length $s_\lambda = 16 \pm 0.5$ mm, maximal radius of curvature $r = 2.2 \pm 0.3$ mm, and fold angle $\theta = 1.65 \pm 0.1$ rad. By contrast, the shallow grooves have wavelength $\lambda = 7.9 \pm 0.5$ mm, amplitude $A = 2.6 \pm 0.5$ mm, arc length $s_\lambda = 10 \pm 0.5$ mm, maximal radius of curvature $r = 1.4 \pm 0.1$ mm, and fold angle $\theta = 1.55 \pm 0.1$ rad.

In Fig. 5.40b, we present 3D-scanned shapes of two rolled groovy sheets with deep grooves: one narrow ($W = 6$ cm), and one wide (W=29 cm). While the short sheet shows a classical rolled shape, the longer sheet has an additional twist: the sheet forms a cylindrical roll, while its grooves twist at a small angle around the cylinder's axis. We quantify the rolling by the sheet's radius of curvature R_{scar} measured at the scar line, and the amount of twisting by the groove angle defined in Fig. 5.40b. Fig. 5.40c shows these two shape measures as a function of edge distance W_f. Two trends stand out here: first, the radius of curvature appears to be non-zero at $W_f = 0$, and increases with W_f until a plateau value is reached. The radius of curvature is of the same order of magnitude as the groove size. Second, the groove angle is negligible for a large range of edge distances W_f, until an abrupt bifurcation takes place. After this bifurcation, the groove's twisting angle jumps to a nearly constant positive (left-twisting) or negative (right-twisting) value. We have observed that the twisted roll can be flipped from right-to left-twisting by applying a small torque to the sheet's edges.

To study the effect of groove geometry, we study shallow-grooved as well as deep-grooved sheets. Typical images of a short and long sheet with shallow grooves are shown in Fig. 5.40d, similar to the 3D scans of Fig. 5.40b. The rolling radius at the scar as well as the groove angle are extracted using a custom Python script; Fig. 5.40e shows the results as a function of varying edge width W_f. Similar to the deep-grooved sheet, the radius of curvature is of the same order of magnitude as the groove size, and increases with W_f; in addition, a sudden twisting transition is seen as W_f increases beyond a critical value. We note that edge width at which the twisting transition takes place is different for the two groove shapes: shallower grooves twist at shorter widths.

Our experiments show that scarred sheets roll, and undergo a twisting bifurcation. We discuss below why these two reshaping effects take place.

First, we explore why the sheet's rolling radius varies with the sheet size in Fig. 5.41. For clarity, we again show the rolling radius of a deep-grooved sheet as a function of

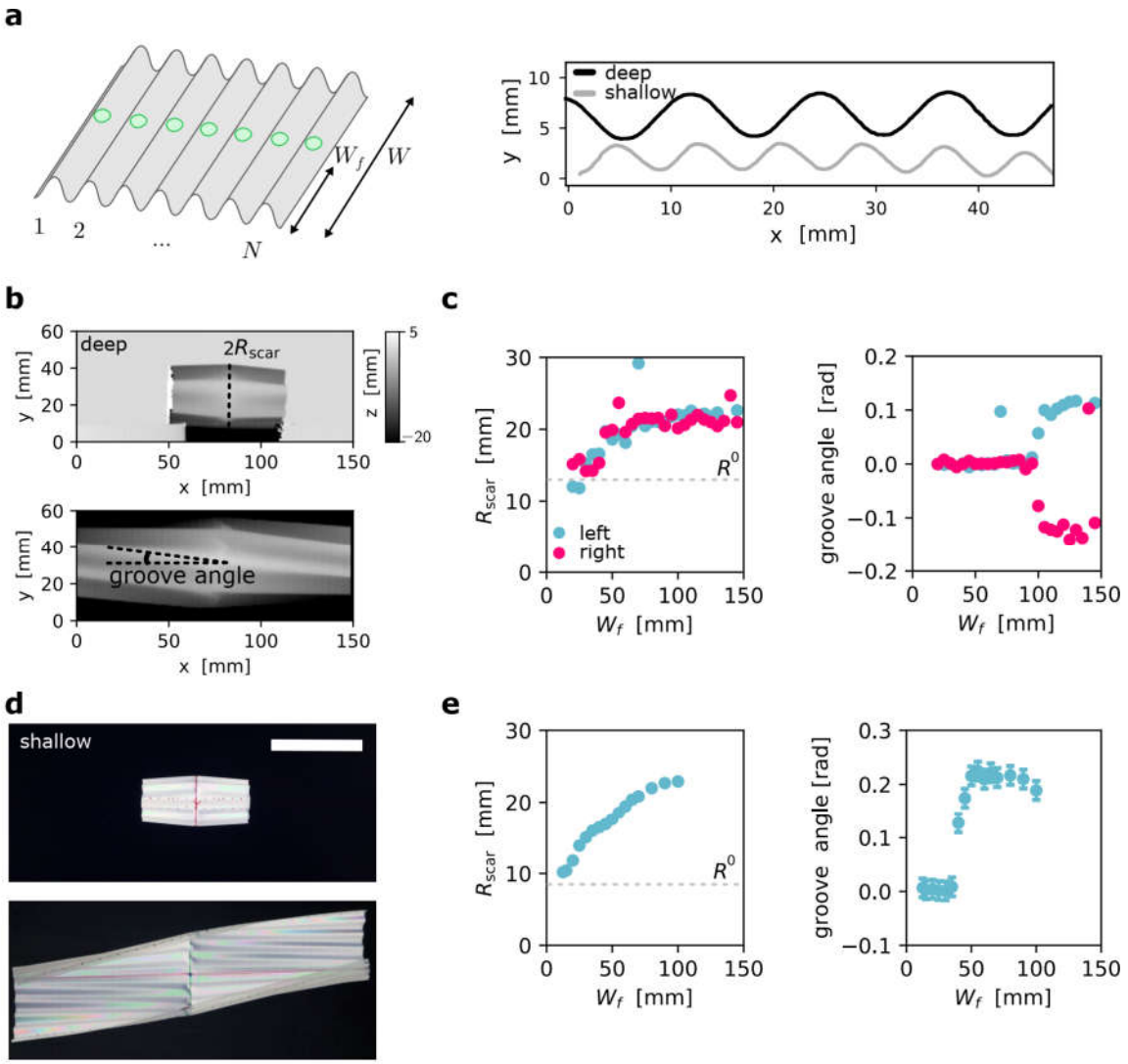

Fig. 5.40.: Detailed shaping effect of a single scar line. a, A single scar line (blue dots) is introduced in a groovy sheet of length L, N grooves, and width W. The scar line lies in the middle of the sheet, at distance W_f to both free edges. Right: experimental sheet profiles for shallow and deep grooves **b,** 3D scans of a sheet with a single scar, thickness $t = 75\ \mu\mathrm{m}$, and $N = 10$ deep grooves, fabricated with static thermoforming (colour bar indicates height). Top: $W_f = 3 \pm 0.3$ cm, bottom:$W_f = 14.5 \pm 0.3$ cm (only central portion near the scar is shown). The sheet rolls up, and twists at large W_f. **c,** 3D shape measures of the scarred sheet. Left: radius of curvature measured at the scar locus, R_{scar}, as a function of free edge width W_f. Right: angle between groove direction and rolling axis. Colours (legend) indicate whether sample was prepared with bias toward left- or right-twisting. **d,** 2D photography of a sheet with a single scar, thickness $t = 75\ \mu\mathrm{m}$, and $N = 10$ shallow grooves, fabricated with dynamic thermoforming. Scale bar: 5 cm. **e,** 2D shape measures of the scarred sheet. Left: scar radius of curvature R_{scar} for varying free edge width W_f. Right: angle between groove direction and rolling axis.

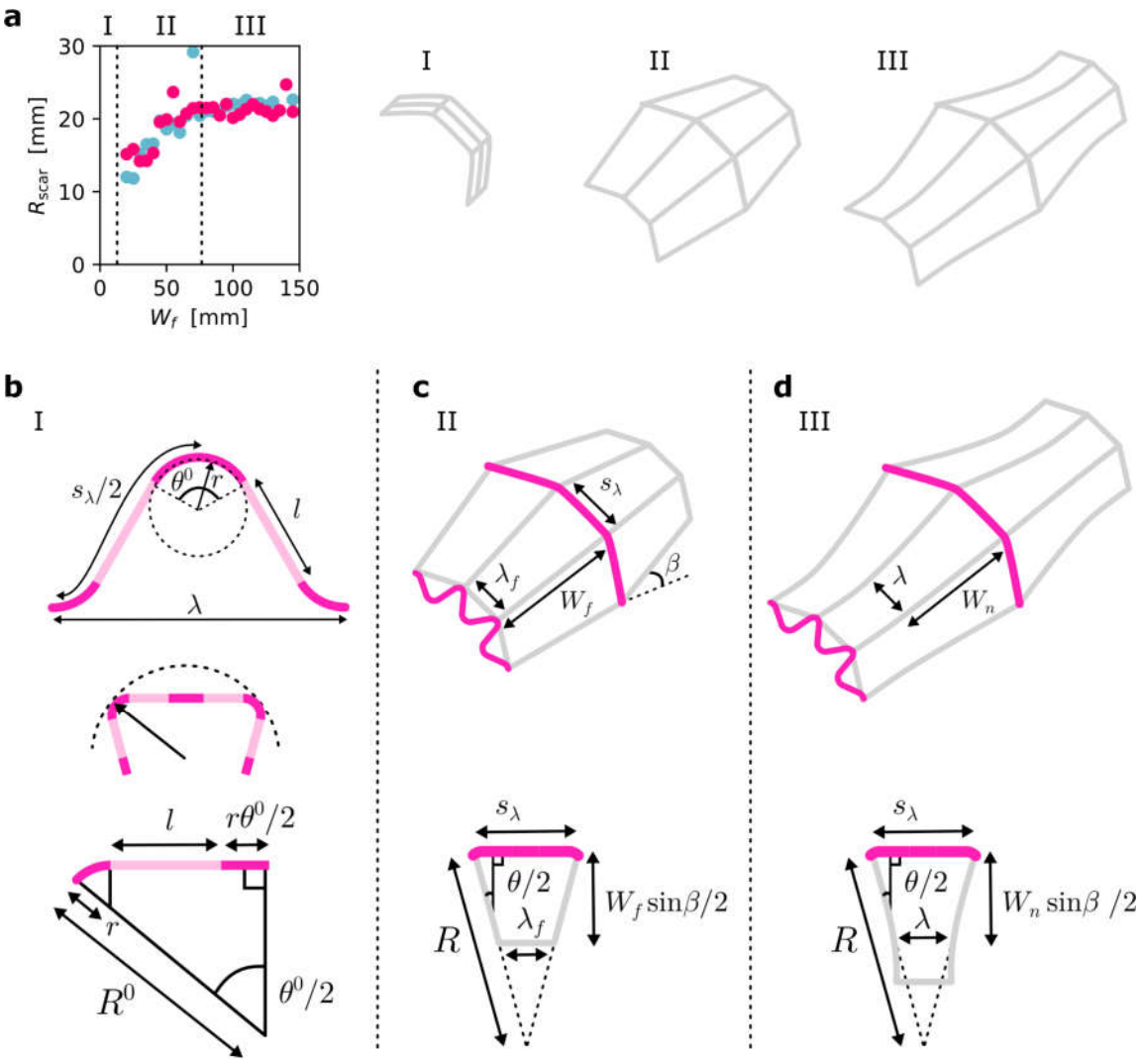

Fig. 5.41.: Variation of scar line curvature R with sheet edge width W_f. **a, b,** Top to bottom: A single groove has facet length l, radius of curvature r, and angle θ^0. Grooves have a resulting wavelength λ and arc length s_λ. A narrow strip near a scar line is deformed: the groove's valleys are flattened, while mountains retain heir original shape. The strip takes on a rolled shape with outer radius of curvature R^0. R^0 can be calculated from the flattened geometry (Eq. 5.33). **c,** Top: geometry of a rolled sheet at intermediate W_f, following the model in Fig. 5.39. Grooves between two mountain folds are flattened at the scar line to length s_λ, and relax over sheet width W_f to length λ_f. Straight grooves meet at the scar line at a small angle β. Bottom: the scar's radius of curvature, R, is calculated using the groove angle θ; under certain assumptions, R increases linearly with W_f (Eq. 5.34). **d,** In sheets with large W_f, grooves bend and relax to their initial wavelength λ over a fixed neutral width W_n. Increase in W_f does not lead to an increasing rolling radius R.

edge width in Fig. 5.41a. Our experiments show that the sheet's rolling radius R_{scar} has finite value at zero sheet width (regime I); initially increases linearly with W_f (regime II); and then plateaus (regime III). The behaviour in these three regimes can be understood, based on geometric considerations.

We start with regime I, where the rolling radius is finite as W_f goes to zero. In Fig. 5.41b, we consider a small strip of material around the scar line. The scar line consists of a chain of defects, created in the valleys of the grooves. Near the scar line, the defects are observed to flatten the valley folds. Assuming the mountains of the grooves remain undeformed, we can make an estimate of the rolling radius, disregarding the influence of the rest of the sheet. The groove is characterized by its arc length s_λ, radius of curvature r, and opening angle θ. Assuming that the folds are alternately flattened and at rest, we can define an outer rolling radius R^0:

$$R^0 = r + \frac{s_\lambda}{2 \sin \theta/2} \ . \tag{5.33}$$

For our sheets, we estimate $R^0 \approx 13$ mm and 8.5 mm for the deep- and shallow-grooved sheets, respectively, in fair agreement with our measurements (Fig. 5.40c,e).

In regime II, the increase of the rolling radius R with sheet edge width W_f can be understood via the geometric model presented earlier in Fig. 5.39, where the grooves of a sheet are modelled as trapezoidal folds. As we illustrate in Fig. 5.41c, we assume that valley folds are flattened near the scar to length s_λ, and that the angle β at which grooves meet at the scar remains constant as W_f is increased. Finally, assuming that the folds relax to their equilibrium configuration at the sheet's edges to a typical length λ, we find a geometric expression for the outer rolling radius as a function of W_f:

$$R(W_f) \approx \frac{s_\lambda}{s_\lambda - \lambda} \sin \frac{\beta}{2} W_f \ , \tag{5.34}$$

which shows that the rolling radius should increase approximately linearly with W_f. Estimating $\beta \approx 0.1$ rad, the slope of R as a function of W_f should lie between 0.2 and 0.3, which is in fair agreement with the experimentally observed slope $0.15 \ \pm 0.5$ in this intermediate regime. Finally, we suggest in Fig. 5.41d that the roll radius' plateau value at large W_f can be understood by assuming that at large widths, the folds relax to their equilibrium state at a fixed neutral axis $W_n < W_f$, resulting in a constant value for R. Thus, while the details of the roll radius' variation with W_f depend on the sheet's shape parameters, the initial value of R, its increase, and its plateau can be understood geometrically.

Finally, we explore why wide scarred sheets twist, while narrow sheets do not. We attribute the twisting transition to an energetic competition between elastic deformations at the scar line and in the sheet's wings. This idea is based on a simple elastic model, formulated in detail in appendix A.12, in which a twisting transition is observed for scarred sheets with a large width. The main results, in the form of equilibrium scarred sheet shapes and their corresponding shape parameters, are shown in Fig. 5.42. Though no saturation of the rolling radius is observed (which we attribute to the absence of groove bending deformations in our simple model), we see an otherwise fair agreement between the modelled and experimental shape measures: the order of magnitude for the rolling radius, groove angle, and twisting transition width correspond reasonably well (compare

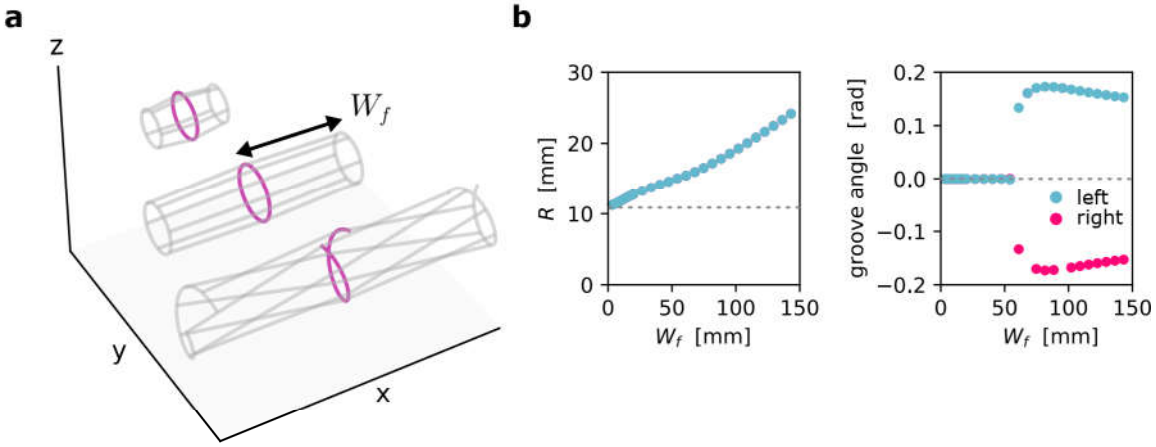

Fig. 5.42.: Twisting transition in a simple elastic model. a, Equilibrium configurations of the model at increasing edge width W_f. Scar line (pink) is either circular or helicoidal; grooves (grey lines) point away from the scar line at a small angle. See appendix A.12 for details. **b,** The scar rolling radius R increases from its initial value R_+ (Eq. 5.33, dashed line) with W_f. Initially, the sheet does not twist; at a critical value of W_f, a bifurcation to finite values of the groove angle is observed.

Fig. 5.40f).

In summary: sheets with single scar lines roll up into a cylindrical shape. The rolling can be understood by considering the geometry of a single groove. The rolled shape's details are set by an interplay of elastic bending and twisting energies. While the exact interplay is challenging to model exactly, experiments show three facts: first, the roll's radius of curvature is finite even for narrow sheets, and increases with sheet width before saturating to a plateau value; second, beyond a critical width, a symmetry-breaking transition causes the sheet's grooves to twist around the cylinder axis; and third, the critical twisting width depends on the groove geometry, with shallower grooves twisting at smaller sheet widths.

5.7.2. Combining scars

Above, we studied the shaping effect of a single scar line- but sheets can support more than one scar. Just a few scar lines can produce complex shapes, as we saw in Fig. 5.38. Can we connect single-scar reshaping to the much more complex multi-scar picture? We propose a simple framework, in which we limit ourselves to a small class of scar line configurations.

We consider only scar lines that are perpendicular to a sheet's grooves. These scar lines can be placed in *series* aligned in a chain, or in *parallel*, side by side. Recall that scar lines also have a parity: they can be made on the crests or in the valleys of grooves, and the two types of scar line yield line curvatures of opposite sign. Given these two options for our scar lines—series or parallel, positive or negative curvature—we can have four basic scar line configurations, which we explore in Fig. 5.43.

Recall the impact of a single scar line, shown in Fig. 5.43a: if made in the groove's valleys, the scar rolls up the sheet into a positive-curvature cylinder section. Fig. 5.43b

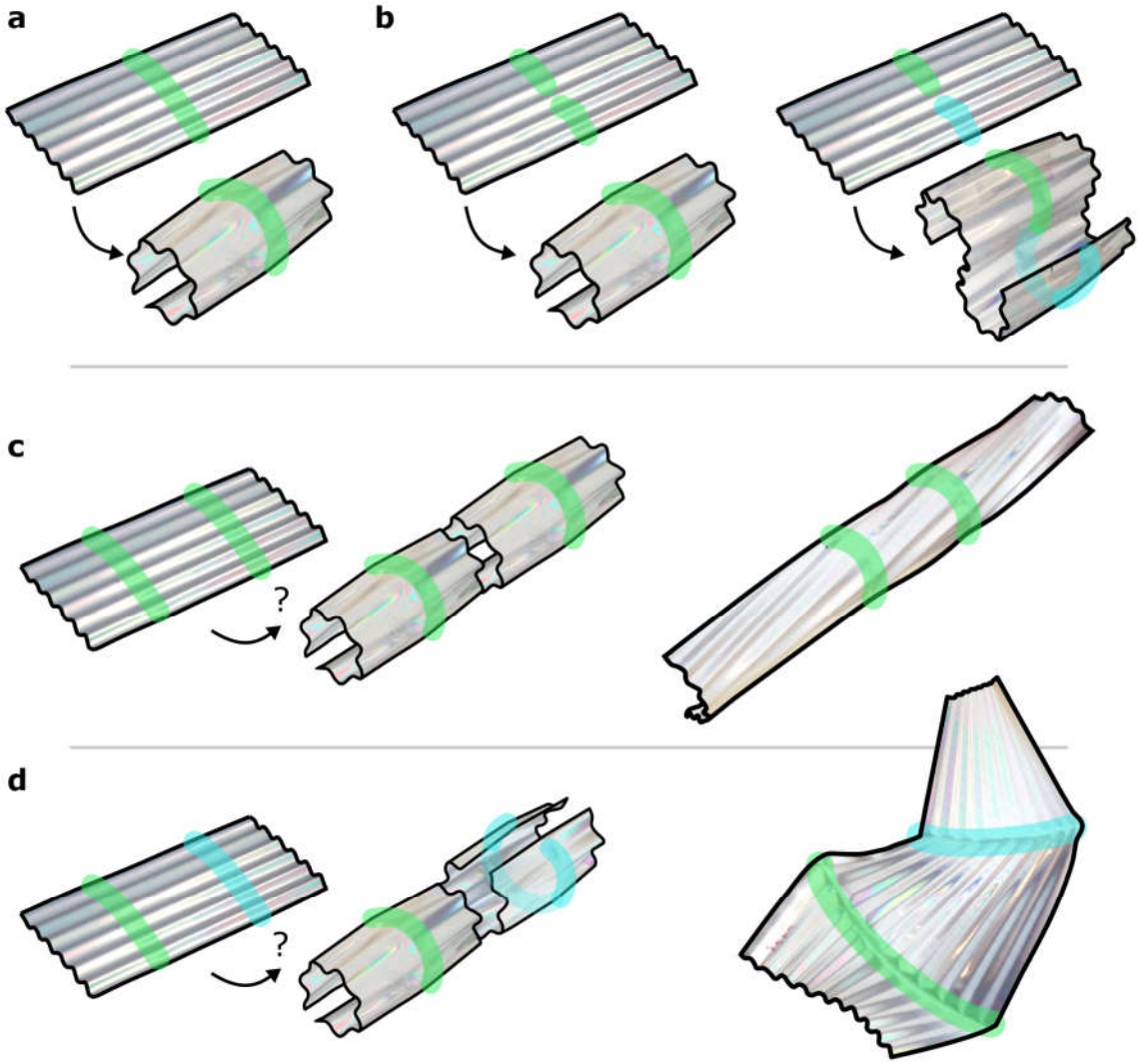

Fig. 5.43.: Combining scar lines. a, A scar line introduced in the crests of a groovy sheet (green line, top) produces a rolled shape (bottom). Groovy sheets shown are cropped and outlined photographs of real samples, viewed between crossed polarisers. **b,** Tiling scar lines in series. Two scar lines of equal parity (green lines) is geometrically equivalent to a single scar line: the sheet rolls up. Two scar lines of opposite parity, one in the sheet's crests (green) and one in the valleys (blue), lead to two rolls of opposite curvature, connected by a flat half-groove at their interface. **d,** Parallel scar lines form complex shapes. Two isolated equal-parity scar lines (green lines, left) form two rolls (middle). When connected, the sheet forms a rolled cylinder, its grooves always twisting around the cylinder's axis (right). **e,** Isolated opposite-parity scar lines (green and blue lines) form two rolls of opposite curvature. There is no simple geometric solution to connect the two rolls at their edges. Experimentally, the sheet section demarcated by the scar lines forms a helicoid; the free 'wings' twist and curve.

shows what happens when scar lines are placed in series. Evidently, two equal-parity scar lines are equivalent to a single scar line, and the sheet rolls up into a positive-curvature cylinder as before. Two opposite-parity scar lines in series (one scar in the grooves' crests, the other scar in their valleys) changes the sheet shape in an intuitive way. The two scar lines produce two cylinder sections, with opposite curvature, that must meet at their long edges. In practise, the two rolls are indeed connected together by a single (minimally-deformed) half-groove, into an S-shape. Thus, a purely geometric picture suffices to capture the shaping effect of scar lines in series: they produce sheets rolled into snake-like cylinder segments, whose sections have alternately positive or negative curvature, consistent with the scar parity. In short: scar lines in series form a stable route to complex shapes with a rolled geometry.

By contrast, geometry alone cannot tell us how scar lines in parallel reshape a sheet. This is illustrated in Fig. 5.43c, where two equal-parity scar lines are created side by side. Based on our simple geometric picture, the sheet should deform into two rolled sections, which must be connected at their lateral edges. It is not possible to create this connection without distorting the sheet: geometric frustration must arise. In practise, while the sheet does roll into a cylindrical shape, its grooves simultaneously twist around the rolling axis. Intriguingly, this twisting behaviour is universally observed across sheet sizes, groove shapes, and thicknesses. Here, both elasticity and geometry govern the sheet shape.

Opposite-parity scar lines in parallel, shown in Fig. 5.43d, are an even more egregious example of the importance of geometric frustration and resulting elastic deformation. The two scar lines now form two rolled sections that must be stitched together along edges with *opposite* curvature. A real sheet tackles this problem by forming a helicoidal surface, twisted around a straight central axis, allowing the scar lines to bend into helices of opposite curvature. While the geometric details vary, the helicoidal shape is present across a diversity of groovy sheets.

In conclusion: sheet shapes are geometrically predictable for scar lines that run in series. However, when scars lines are placed in parallel, elasticity and deformation play a crucial role. We explore this interplay between elasticity and geometry below.

5.7.3. Parallel scars

In this section, we investigate sheets with parallel scar lines. As illustrated previously in Fig. 5.43d-e, parallel scar lines produce complex sheet shapes that depend on the scars' parity. Below, we experimentally study sheet shapes for equal-parity and opposite-parity scars. As for single scars (section 5.7.1), we investigate the effect of the groove geometry on the final sheet shape by performing our experiments on two sheet types, with deep and with shallow grooves respectively (see Fig. 5.44). In addition, we quantify how sheet width and scar positioning affects the final shape. We present the shaping effect of two equal-parity scars in Fig. 5.45, and show there that sheets with two equal-parity parallel scar lines universally form cylindrical, slightly twisted rolls. By contrast, we show in Fig. 5.46 that sheets with opposite-parity scar lines form helicoid-like shapes. Our results show that parallel scar lines produce intricate but consistent rolling and helixing shapes, whose general attributes can be captured by simple shape measures across groove shapes, sheet widths, and scar positions.

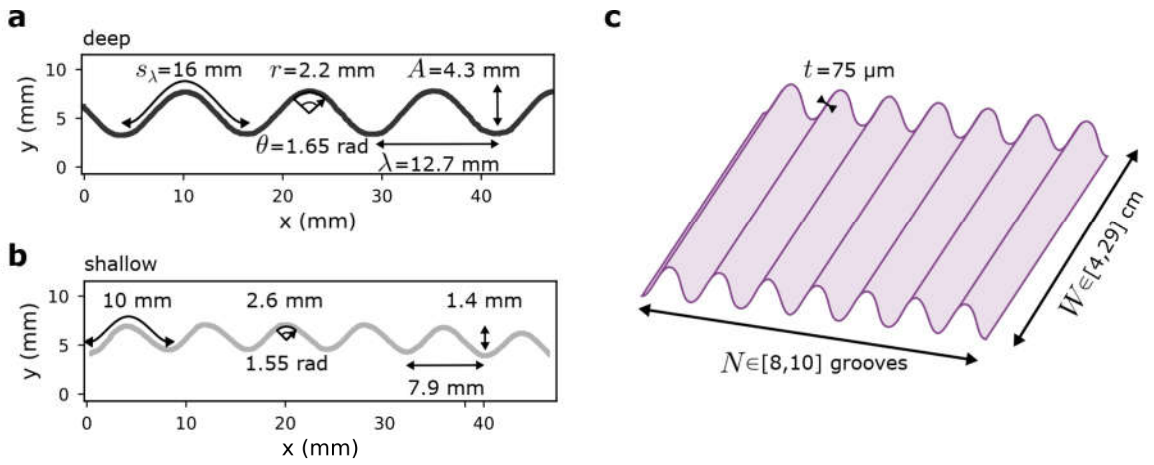

Fig. 5.44.: Geometry of sheets with deep and shallow grooves. **a,** Photography-derived profile of a sheet with deep grooves. Groove arc length s_λ, radius of curvature r, fold angle θ, wavelength λ and amplitude A are indicated; see section 5.7.1 for estimated errors. **b,** Profile of a shallow-grooved sheet with shape measures indicated as in **a.** **c,** Overall sheet size. We investigate sheets with fixed thickness $t = 75$ µm, variable width $W \in [4, 29]$ cm, and large number of grooves $N \in [8, 10]$.

Equal-parity scars

We start in Fig. 5.45 by experimentally measuring the shape of sheets with two equal-parity scar lines. As illustrated in Fig. 5.45a, the sheets have a fixed thickness $t = 75$ µm, $N = 10$ or 8 grooves, and a variable width W. The scar lines are placed symmetrically at a mutual distance D, each scar line at a distance $W_f = (W - D)/2$ to the nearest sheet edge (Fig. 5.45a). As first noted in Fig. 5.43c, we observe that sheets deform into cylindrical rolls, where the sheet's grooves consistently show a small amount of twisting around the rolling axis.

We first investigate the shape of a sheet with $N = 10$ deep grooves in Fig. 5.45b, where we show a typical example of a 3D-scanned, scarred sheet. Its cylindrical shape can be quantified via the roll's radius of curvature, which is maximal at the scar lines and decreases to R_{centre} in between the two scars. We use the central rolling radius, R_{centre}, to quantify rolling. The sheet's grooves consistently show a finite twisting around the rolling axis, which we quantify using the groove angle as before for single scar lines (recall Fig. 5.40b).

The rolling and twisting shape of deep-grooved sheets is measured for a variety of sheet widths $W \in [17, 29]$ cm and scar spacings $D \in [9, 21]$ cm. Note that the two scar lines are not stable if either $D \lesssim 7$ cm or $W_f \lesssim 3$ cm: in order not to unpop, the scar lines must be a sufficient distance away from each other and from the sheet's edge. The two shape measures—the central rolling radius and groove angle—are shown in Fig. 5.45c. We consider the rolling radius R_{centre} as a function of sheet width W. As for single scars, the rolling radius increases approximately linearly with the sheet width. Extrapolating this trend to small widths W, a finite rolling radius is expected even at vanishing sheet width. Generally, the order of magnitude of the rolling radius is comparable to the typical groove arc length s_λ. Both the finite (extrapolated) magnitude of R_{centre} at vanishing

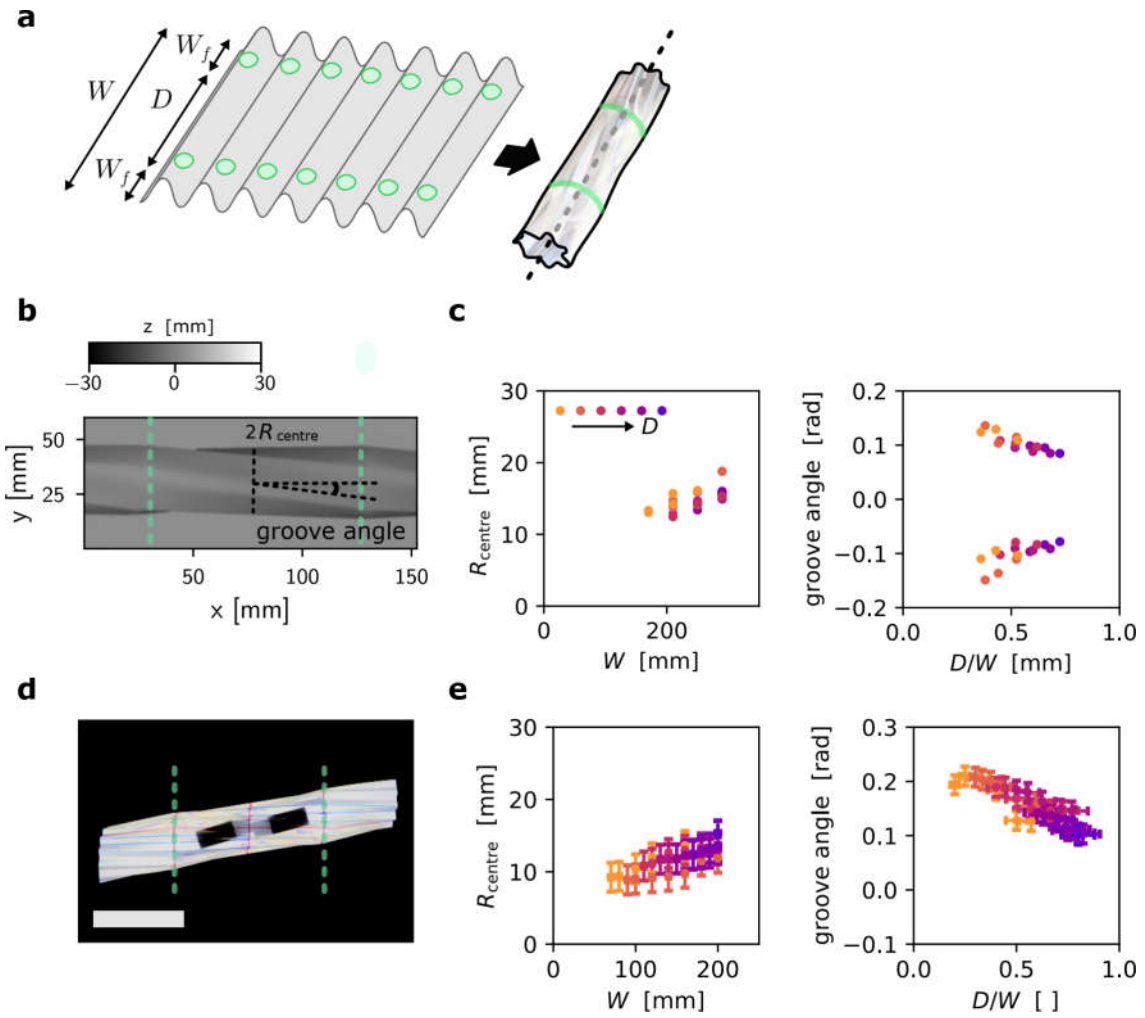

Fig. 5.45.: Shaping effect of equal-parity scar lines. a, Left: two parallel scar lines (green dots) are popped in a groovy sheet of width W at a mutual distance D. Each scar lies at distance W_f to its nearest free edge. Right: as a result, the sheet rolls up and twists around a straight axis (dashed line). **b,** 3D scan of a double-scarred sheet ($N = 10$ deep grooves), fabricated with static thermoforming. Here, $W_f = 4 \pm 0.5$ cm and $D = 9 \pm 0.5$ cm. The sheet's edges lie out of frame. Scar lines are indicated with green dashed lines. **c,** 3D shape measures of a scarred sheet. Left: radius of curvature measured at the middle of the sheet, R_{centre}, as a function of total length W. Right: angle between groove direction and rolling axis as a function of scar distance over total length D/W. Colours indicate constant value of D as a guide to the eye (inset). **d,** 2D photography of a shallow-grooved sheet of total width $W = 16 \pm 0.5$ cm with scars at mutual distance $D = 8 \pm 0.5$ cm and $N = 8$ grooves, fabricated with dynamic thermoforming. Dark rectangles are opaque supports; red marks on the sheet were used for alignment. Scale bar: 5 cm. **e,** 2D shape measures of a scarred sheet. Left: central radius of curvature R_{centre} for varying sheet width W, right: angle between groove direction and rolling axis.

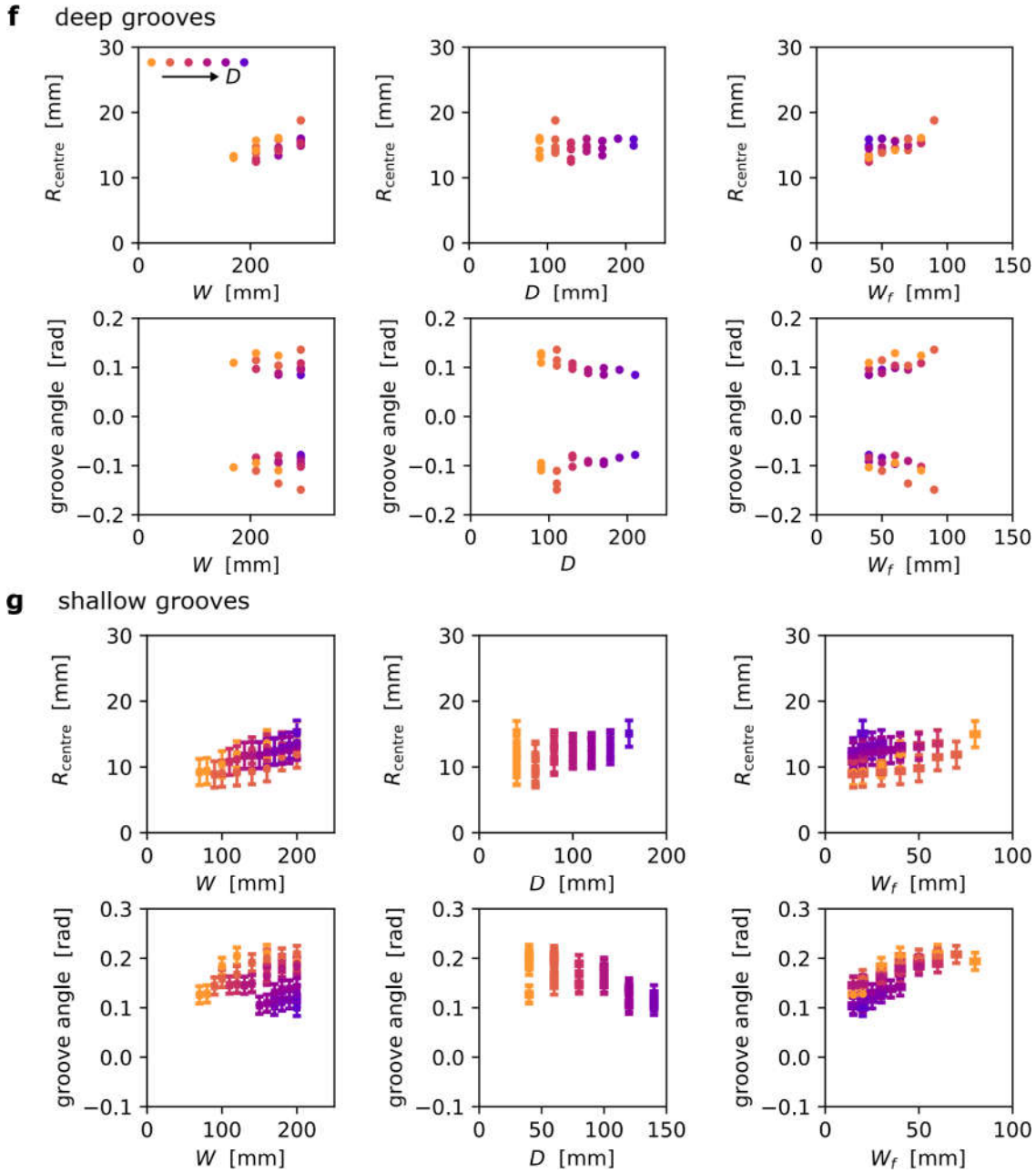

Fig. 5.45.: (continued) Shaping effect of equal-parity scar lines. f, Extended overview of the shape of sheets with deep grooves, corresponding to panels **b-c**. We show the central curvature radius R_{centre} and groove angle (rows) as a function of sheet size and scar positioning, quantified by sheet width W, scar line spacing D, and edge width W_f (columns). Colours correspond to the magnitude of D. **g,** Shape of sheets with shallow grooves, as in **d-e**. Rolling radius R_{centre} and groove angle (rows) are shown versus sheet width W, scar line spacing D, and edge width W_f (columns).

sheet width, as well as its linear increase, are consistent with the behaviour for a single scar explored in section 5.7.1. By contrast, the double-scarred sheet's twisting behaviour deviates from that of a single-scarred sheet. Fig. 5.45c reports the sheet's twist using the groove angle, which is shown as a function of scar separation relative to sheet width, D/W. The groove angle lies around 0.1 rad, similar to the groove angle for a single scar (recall Fig. 5.40c). The groove angle declines linearly as the ratio between scar spacing and sheet width grows; however, no twisting bifurcation is observed. That is, double-scarred sheets *always* twist.

Secondly, we explore the effect of groove geometry. We investigate the shape of scarred sheets with $N = 8$ shallow grooves, using 2D photography; a typical example is shown in Fig. 5.45d. The sheet's rolling and twisting shape measures, extracted using a custom Python script, are reported in Fig. 5.45e. Note that for these shallow-grooved sheets, scar lines must be more than $D \gtrsim 3$ cm away from each other, and $W_f \gtrsim 1.5$ cm away from the sheet edges; while the halving of these critical distances compared to those for deep-grooved sheets above is suggestive, we do not explore it further here. As before, the rolling radius R_{centre} is shown for shallow-grooved sheets in Fig. 5.45e (left) as a function of sheet width W. Consistent with previous results, the rolling radius is of the same order of magnitude as the typical groove arc length; it is, by extrapolation, finite at vanishing sheet width; and increases linearly with W. The sheet's groove angle is always finite, and lies near 0.2 rad for all probed ratios of scar spacing to sheet width, D/W. Note that the twisting angle for shallow grooves is about twice as large as the twist angle for deep grooves. While it is not clear where this difference in twisting magnitudes comes from, it is consistent with the twisting magnitude in the presence of a single scar line (recall Fig. 5.40c,e), which is twice larger for shallow grooves than for deep grooves.

For completeness, we show the rolling radius and the groove angle as a function of scar distance D, sheet width W, and edge width W_f for both deep- and shallow-grooved sheets in Fig. 5.45f–g. We observe the following two general trends. The rolling radius R_{centre} increases with W, but does not show a clear correlation with either D or W_f. In addition, the groove angle decreases with D, but shows an increase with W and W_f. Thus, while both shape measures vary to some degree with the scar and sheet widths, we propose that the sheet width W shows a good correlation with R_{centre}, while the scar-to-sheet-width ratio D/W (which metric unifies the groove angle's dependence on D and W) is a strong predictor for the groove angle.

In summary: sheets with two equal-parity scars always roll and twist. While the exact rolling and twisting magnitude depend on the groove geometry, the scar separation D, and the sheet width W, the typical twisted cylindrical shape is observed throughout.

Opposite-parity scars

We now move on to explore the shape of sheets with two *opposite*-parity scar lines in Fig. 5.46. Fig. 5.46a shows how we create two opposite-parity scar lines at mutual distance D in a sheet with width W; the scar lines are located at edge width $W_f = (W - D)/2$ to their nearest boundary. How the scarred sheet deforms is illustrated in Fig. 5.46a (right): the central portion of the sheet, between the scar lines, twists into a helicoidal shape (recall Fig. 5.43d). The sheet's central axis (around which the helicoid twists) remains straight, while the sheet's side lobes curve freely. Our experiments show that

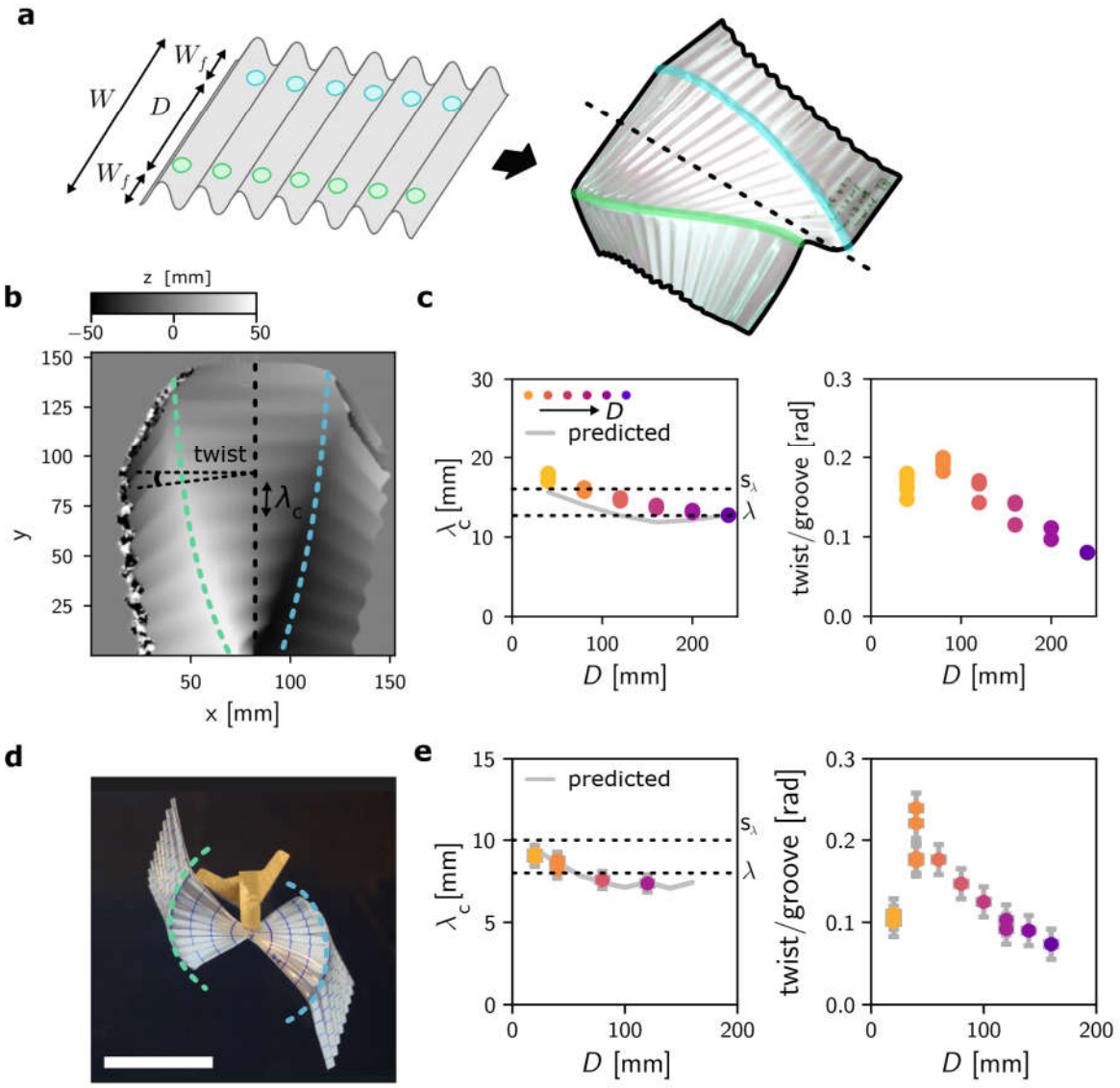

Fig. 5.46.: Shaping effect of opposite-parity scar lines. **a,** Left: two parallel, opposite-parity scar lines are popped into the top (green dots) and bottom(blue dots) of a groovy sheet of width W at a mutual distance D. Each scar lies at distance W_f to its nearest free edge. Right: the sheet's centre forms into a helicoidal shape, with curving side wings. The helicoid's central axis is shown (dashed line). **b,** 3D scan of a deep-grooved, double-scarred sheet ($N = 10$ grooves), fabricated with static thermoforming. Here, $W_f = 4.5 \pm 0.5$ cm and $D = 8 \pm 0.5$ cm. Twisting of the central sheet portion is quantified by the twisting angle per traversed groove; stretching of the axis is measured via the central groove wavelength λ_c, as indicated. **c,** 3D shape measures of a scarred sheet. Left: groove wavelength λ_c measured at sheet's central axis as a function of scar separation D, where dashed lines indicate the approximate resting and maximal wavelengths λ and s_λ. Average predicted values are shown (grey line, Eq.5.35). Right: twist angle per groove as a function of scar distance D. Colours correspond to constant values of D as a guide to the eye. **d,** Top-view photograph of a shallow-grooved sheet of total width $W = 14 \pm 0.5$ cm and $N = 9.5$ grooves with scars at mutual distance $D = 8 \pm 0.5$ cm. Dashed lines indicate scars. Orange block functions as sample support; markings on the sheet are used for alignment and calibration. Scale bar: 5 cm. **e,** 2D shape measures of a scarred sheet. Left: central axis wavelength for varying scar distance D (dashed lines are extremal wavelengths, solid line as in Eq.5.35), right: average twisting of grooves.

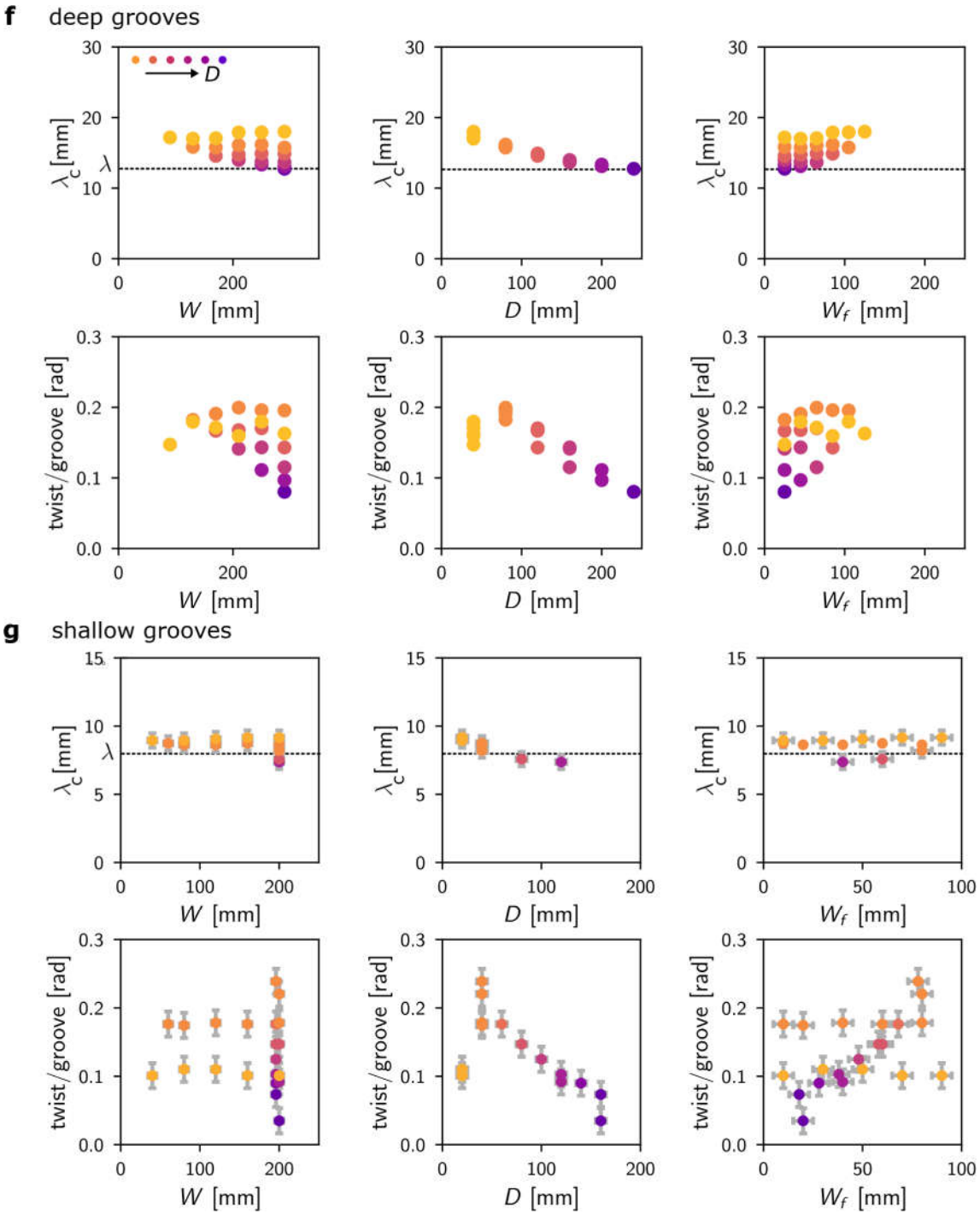

Fig. 5.46.: (continued) Shaping effect of opposite-parity scar lines. f, Extended overview of the shape of sheets with deep grooves, corresponding to panels **b-c**. We show the central axis' groove wavelength λ_c and twist angle per groove (rows) as a function of sheet size and scar positioning, quantified by sheet width W, scar line spacing D, and edge width W_f (columns). Colours correspond to the magnitude of D. Dashed lines correspond to the resting value of groove wavelength λ throughout. **g,** Shape of sheets with shallow grooves, as in **d-e**. Axial wavelength λ and twist per groove (rows) are shown versus sheet width W, scar line spacing D, and edge width W_f (columns).

the sheet between the two scar lines is well-approximated by a helicoid, as we will argue below.

Sheets with deep grooves are first studied via 3D scans (Fig. 5.46b). We study sheets with $N = 10$ grooves, variable width $W \in [9, 29]$ cm, and variable groove distance $D \in [4, 24]$ cm. Opposing scar lines are observed to be unstable if their mutual separation D is smaller than 3 cm, or when their edge distance W_f is smaller than about 2 cm. Opposite-parity scar lines thus have a larger range of stability than their equal-parity counterparts, which become unstable for $D \lesssim 7$ and $W_f \lesssim 3$ cm. Notably, the sheets show a consistent shape across the parameter space. Between the two scar lines, the sheet's folds remain approximately straight, but twist with respect to each other around the sheet's central axis to form a helicoidal surface (that is, the plane spanned by a double helix). Two shape measures characterize the helicoid: the average angular twist between two subsequent grooves, and the groove wavelength λ_c along the central axis.

Fig. 5.46c shows the central wavelength and the twisting per groove of the deformed sheet's helicoidal section. We first show the central wavelength as a function of scar line distance D. Note that the central wavelength may be longer or shorter than the resting length λ due to axial extension or compression of the sheet; it should not be larger than s_λ, which is the full arc length of a flattened groove. As shown in Fig. 5.46c (left), the central wavelength is maximal at small scar line separations. λ_c appears to lie above its maximal value of s_λ, which we tentatively attribute to image warping in our 3D-scanning procedure. As the scar lines are moved farther apart, λ_c decreases smoothly to approximately its equilibrium value λ. The measured data (21 data points) collapse with good accuracy to a single curve. Our data suggest that the sheet's central axis is nearly fully stretched at small scar separations, but relaxes to around its preferred length at large separations. Second, the average twisting angle per groove is shown in Fig. 5.46c (right) as a function of scar spacing D. We observe two regimes that cross over around $D \approx 8$ cm: the twisting angle initially grows when the scars are close together, but subsequently decreases as the scars are brought farther apart. The twisting angle lies around 0.1]radian, and is similar in magnitude to the groove angle reported for sheets with one or two equal-parity scars (Figs. 5.40c,e and 5.45c,e).

We now argue that the experimental data support that the sheet's central section is helicoidal. Bolstered by the success of our helix-based model in section 5.7.1, we assume that the two opposite-parity scar lines are helical. The two scars spiral around a cylinder of radius $D/2$. At the cylinder's axis, each groove has central wavelength λ_c; at the scar, a groove is stretched out to its maximal arc length s_λ. The relation between helix arc length and corresponding axis length is given by wavelength is given by $s_\lambda = \lambda_c \sqrt{1 + (\frac{D\zeta}{2\lambda_c})^2}$ for helices. Thus, if the sheet is helicoidal, the central wavelength λ_c may be calculated via the known scar separation D, average twist angle per groove ζ, and groove arc length s_λ via

$$\lambda_c = \sqrt{s_\lambda^2 - (\frac{D}{2}\zeta)^2)} \ . \tag{5.35}$$

The predicted central wavelength, based on the experimentally measured average twist per groove, is plotted in Fig. 5.46c. The prediction shows a reasonable quantitative agreement with experiments. Most importantly, the qualitative behaviour of the central

wavelength with varying D is reproduced: its initial maximal value s_λ at $D = 0$ decreases to a plateau value, around λ, for large scar separations. Thus, the sheet's central section is well-approximated by a helicoidal plane.

Secondly, we investigate the effect of groove shape in Fig. 5.46d, where the helicoidal shape of sheets with $N = 9.5$ shallow grooves is studied via photography. The sheet width and scar separation are varied between $W \in [4, 20]$ cm and scar separation $D \in [2, 16]$ cm. For these shallow-grooved sheets, opposite-parity scar lines are not stable if the scar separation or edge distance is too small: $D \lesssim 2$ cm or $D \lesssim 1$ cm, respectively. The sheet's total central length and total twisting angle are extracted manually from the photographs via graphical angle- and distance-measurement tools, and divided by the number of grooves to obtain the central wavelength λ_c and the average twisting angle per groove. The results are shown in Fig. 5.46e. First and foremost, we note that the trends in axial stretch and groove twist observed for deep-grooved sheets are reproduced here. Specifically, consider the sheet's central wavelength λ_c as a function of scar separation D. The central wavelength lies near its maximal value of s_λ at small D, and decreases to a plateau value around λ as the scars are moved farther apart. In addition, the average twist angle per groove is small for scars that are close together; however, the twisting increases to a peak value around $D \approx 4$cm, and subsequently decreases with D. The magnitude of the twisting per groove, around 0.1]radian, appears to be similar for both deep- and shallow-grooved sheets. Finally, the central wavelength predicted using the helicoid model in Eq. 5.35 is shown in Fig. 5.46e (left). The predicted and experimental values match both qualitatively and quantitatively. In conclusion: for shallow-grooved sheets, the sheet shape between the two scar lines is helicoidal.

Finally, we show the sheets' helicoidal shape parameters (centre wavelength λ_c and twisting per groove) as a function of scar distance D, sheet width W, and edge width W_f for both deep- and shallow-grooved sheets in Fig. 5.46f–g. Intriguingly, the scar spacing D is correlated most strongly with variations of the shape parameters. By contrast, neither the central wavelength nor the twisting appear to be significantly affected by either W or W_f. Thus, the scar spacing D is the strongest predictor for variations of the sheet shape.

Our findings above show that parallel scar lines produce distinct shapes, depending on their parity. Equal-parity scar lines consistently produce twisted, cylindrical rolls, while opposite-parity scar lines yield helicoidal sheet sections flanked by curving wings. The exact shape details—the amount of rolling, twisting, and helixing—depends on the sheet's size, the scar separation, and the groove geometry. However, the general shape of double-scarred sheets (a twisted roll; a helicoid) is retained throughout. We therefore envision a geometrical model, in which sheet sections flanked by scar lines can be seen as puzzle pieces. These puzzle pieces may be tiled and connected in series or in parallel as first illustrated in Fig. 5.43, based on rules of geometric compatibility and elastic deformation. Such a model could form a solid basis for future complex shape design of scarred groovy sheets.

5.7.4. Understanding sheet shapes: outlook

The experiments of the previous sections demonstrated that sheets with scar lines orthogonal to their grooves can roll, twist, and helix. Phenomenologically, the overall shape of the sheet depends mostly on its internal configuration of scar lines rather than its geometric details such as size and groove shape. This leads us to the question: *is there a way to model sheet shapes geometrically*?

We argue that there is. Our experiments show three important features of sheets with scars orthogonal to their grooves. First, their grooves are approximately straight, except very close to scar lines; second, scar lines have circular or helical shapes; and third, grooves appear to lie orthogonal to scar lines. There is a geometrical model for sheets with these properties: *ruled surfaces*. We previously used ruled surfaces to build an elastic model of sheets with a single scar line (recall section 5.7.1); here, we briefly review the basics of ruled surface geometry, and show that we can construct simple ruled surfaces whose shape closely mimics that of real groovy sheets.

Ruled surfaces are a subclass of geometrical surfaces that can be created as follows. The process starts with a base curve (or directrix) in 3D space, $\boldsymbol{g}$. The directrix has a local coordinate frame[108], the Serret-Frénet frame $(\hat{\boldsymbol{t}}, \hat{\boldsymbol{n}}, \hat{\boldsymbol{b}})$ (defined via the derivatives of $\boldsymbol{g}$) that describes how the curve bends and twists in space. Moving along the curve's arc length, straight lines (or rules) are drawn, starting from the curve and radiating out in space. Each rule can be described by its components along the local coordinate frame. Together, the directrix and rules form a surface in space.

Based on our observations, we propose to model our sheets as ruled surfaces under the following constraints. First, we assume that the scar line can be described as a helical directrix. Recall that we used the same assumption for our simple energetic model for single-scarred sheets in section 5.7.1. The helical scar line, g, is then given by

$$\boldsymbol{g}(t) = (R\cos s, R\sin s, Tt) \ , \tag{5.36}$$

where R is the helix' radius of curvature, and $2\pi T$ is the pitch along coordinate t over which the helix repeats itself. Note that the directrix is a simple circle if the pitch is zero. The directrix' coordinate frame is then given by:

$$\hat{\boldsymbol{t}} = \frac{1}{\sqrt{R^2+T^2}}(-R\sin t, R\cos t, T) \tag{5.37}$$

$$\hat{\boldsymbol{n}} = (-\cos t, -\sin t, 0) \tag{5.38}$$

$$\hat{\boldsymbol{b}} = \frac{1}{\sqrt{R^2+T^2}}(T\sin t, -T\cos t, R) \tag{5.39}$$

Secondly, we assume that groove facets can be modelled with straight rules. They lie orthogonal to the scar line: rules are linear combinations $\hat{\boldsymbol{r}} = \cos\beta\hat{\boldsymbol{b}} + \sin\beta\hat{\boldsymbol{n}}$ of the directrix' normal and binormal vectors. Lastly, given the periodicity of our sheets, we only consider rules that have fixed components along $\hat{\boldsymbol{n}}$ and $\hat{\boldsymbol{b}}$ across the entire directrix.

We illustrate in Fig. 5.47 how to use this constrained ruled-surface model to mimic sheet shapes with one or two scar lines. Fig. 5.47a shows a sheet with one central scar line with small width W, without any groove twisting. The scar line is modelled by

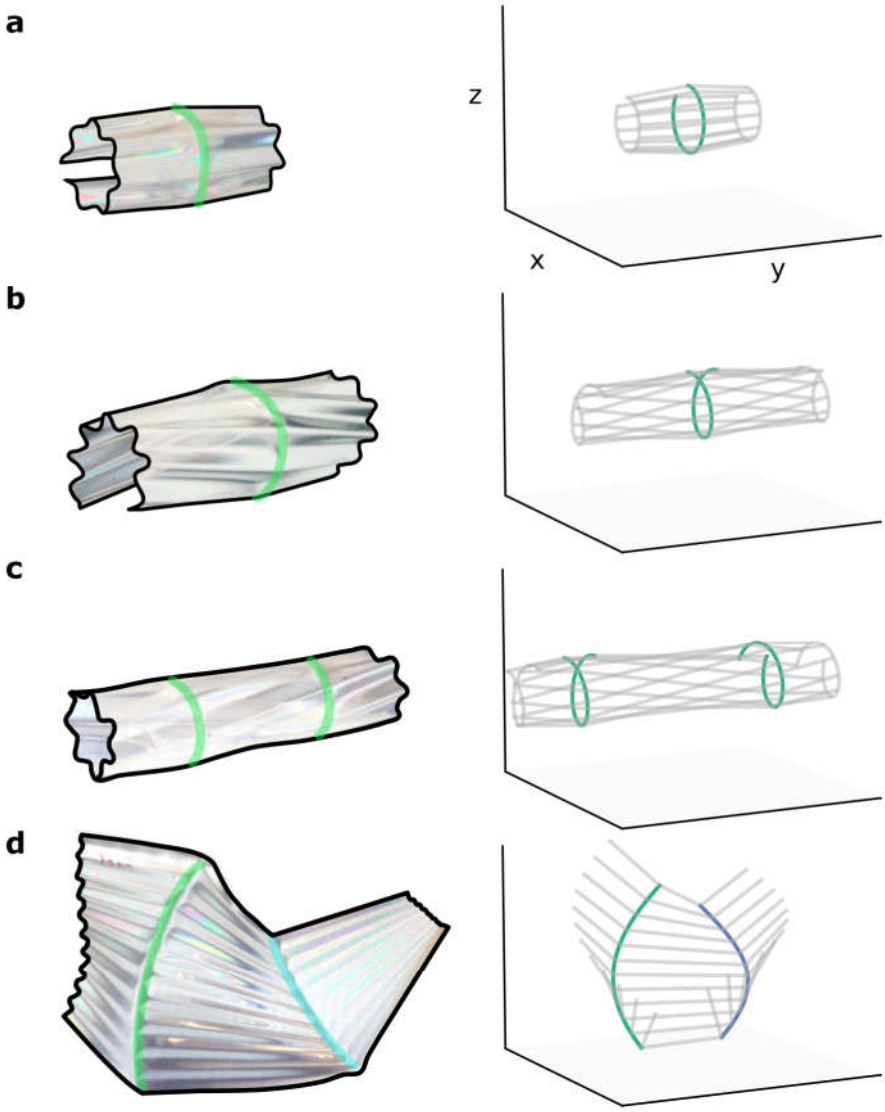

Fig. 5.47.: Groovy sheets look like ruled surfaces. a, A small sheet with a single central scar (left) is approximated by the ruled surface (right). The directrix (green) and rules (grey) corresponding to the scar line and groove facets are shown. The directrix is a circle with constant radius of curvature. Rules lie along a linear combination $\hat{\boldsymbol{r}} = \cos\beta\hat{\boldsymbol{b}} + \sin\beta\hat{\boldsymbol{n}}$ of the directrix' normal and binormal vectors $\hat{\boldsymbol{n}}, \hat{\boldsymbol{b}}$ at small $\beta = 0.1$. **b,** A wide sheet with a central scar rolls as well as twists. The scar line is modelled by a helical directrix with $T/R = 0.15$, while rules lie along the directrix' normal and binormal vector at a fixed ratio with $\beta = 0.1$. **c,** Rolling, twisting sheet with two equal-parity scar lines. Scar lines are helical ($T/R = 0.15$); rules lie along a fixed angle in the directrix' normal-binormal plane with $\beta = 0.1$ **d,** Helicoidal sheet with two opposite-parity scar lines (green, blue curves). Scar lines are helical (T/R=1) with a large pitch-to-curvature ratio. Rules between the scar lines are oriented along the directrix' normal vector; wing rules are chosen in the normal-binormal plane with $\beta = 0.5$

a circular directrix with zero twist T, while the groove facets are approximated with rules $\hat{\boldsymbol{r}} = \cos\beta\hat{\boldsymbol{b}} + \sin\beta\hat{\boldsymbol{n}}$ at a fixed normal-binormal ratio set by small values of β (see Fig. 5.47 for the values chosen to generate the illustrated surfaces). The resulting surface shape looks like two truncated cones, their bases aligned, similar to the real rolled sheet. Fig. 5.47b shows a sheet with larger width W that twists as well as rolls. We therefore model the scar line as a helical directrix with a small twist, $T/R \ll 1$. The rules can be

modelled, as before, to lie mostly along the local binormal with a small normal component. The model surface matches the real sheet's overall shape well. To show that our model can work for parallel scar lines, too, we consider a sheet with two equal-parity scar lines in Fig. 5.47c. Notably, the directrices and rules corresponding to the two scar lines and their connecting grooves can be modelled identically to those for a single scar line; the two scar lines do have a small phase offset due to their finite twist. As in the real sheet, the model surface has a rolled and twisted shape, where the radius of curvature of the roll decreases away from the scar lines. Finally, a sheet with two opposite-parity scars is illustrated in Fig. 5.47d. Here, the two directrices are identical helices with a twist comparable to the radius of curvature: $T/R \approx 1$. The directrices form a double helix, differing by a phase π, so that their mutual distance is constant at $2R$. The helices circle around the $\hat{\boldsymbol{z}}$-axis, while the rules that connect them lie perpendicular to $\hat{\boldsymbol{z}}$: the rules are oriented fully along the normal vector $\hat{\boldsymbol{n}}$. Rules in the surface's wings, that extend away from the central helicoidal surface, are chosen here to lie in the normal-binormal plane. The model surface's helicoidal section compares favourably to the real sheet.

Thus, groovy sheet shapes can be approximated as ruled surfaces. Specifically, we hypothesize that sheets with one or more scar lines may be modelled by surfaces generated from helicoidal base scars, where rules that mimic grooves point perpendicularly away from the scars. We envision an energetic extension to this purely geometric model that may be used to model groovy sheets more precisely, analogous to the simple model discussed in section 5.7.1. For example, it costs energy to open, close, and twist grooves in real sheets. This can be modelled by associating an energetic cost to deviations from parallelity of the surface's rules. In addition, scar lines appear to carry an intrinsic, constant curvature, which may be included in the surface model by penalizing deviations from this value. In short: we propose decorating our geometric model with elastic properties that mimic the mechanics of a real sheet. This strategy provides a clear avenue for predicting and designing the shapes of real groovy sheets.

5.8. Conclusions and outlook

In the preceding chapter, we showcased the unique shape-morphing capacities of groovy sheets. Several sheet fabrication methods were presented, including thermoforming plastic and spin-coating rubber, to create groovy sheets at the centimetre scale. We showed that elastic instabilities lie at the heart of groovy sheet's shape-shifting: each groove can support snap-through defects that locally change the structure's shape. We saw that snap-through defects are stable in sheets whose size lie in a goldilocks zone: they must be neither too narrow, nor too wide. Adjacent defects were shown to interact and attract at short range, resulting in their alignment into scar lines of contiguous defects. We explored and modelled the reshaping effect of individual scar lines, and argued that sheet shapes can be classified systematically according to their internal configuration of scar lines. Finally, we presented a novel approach for modelling groovy sheets with ruled surfaces- a strategy that proved successful for sheets with single scar lines.

Several avenues for deeper research present themselves now, and we discuss them briefly. First, the stability and interaction of defects in groovy sheets depends on the grooves' geometry. Preliminary experimental evidence shows that defect attraction is decreased in sheets with shallow grooves, which precludes the creation of stable scar lines. In such systems, staggered defect patterns rather than contiguous chains are observed. In short: tuning the interactions between defects could give rise to a host of new defect configurations besides scar lines, and corresponding exotic new shapes. Exploring the relation between geometry and defect interactions could thus provide a rich vein of new sheet shapes. Secondly, we have shown that the shape of scarred sheets can be captured successfully with ruled surfaces. Such ruled surfaces provide a convenient way to summarize sheet shape in a few parameters. However, quantitative models for sheets with multiple scars has yet to be developed; we envision that decorating ruled surfaces with energetic constraints, as we have done for sheets with single scars, will provide the means to predict and design complex sheet shapes.

What makes groovy sheets unique is their geometry-driven shape-morphing. In extant work, a variety of structural morphing strategies has been proposed: flat sheets can transform into complex 3D target shapes using patterns of folds, cuts, or regions that swell under mechanical forcing, heat or light. However, these strategies have their drawbacks. The resulting structures are only stable under sustained forcing, morph slowly or irreversibly, or need a distinct design for each desired target shape. By contrast, groovy sheets morph fast, via snap-through instabilities that occur on the order of the speed of sound in the underlying material. Groovy sheets morph elastically, since they are thin enough not to exceed plastic strains even under large deformations. And finally, groovy sheets morph into many different shapes with minimal programming. We propose that groovy sheets are one realization of a conceptual class of shape-morphing materials, whose reshaping properties come from their geometry, not their underlying material or size. We expect that our geometric approach can be extended to thin materials with different surface patterns, thus establishing a new paradigm for fast and reversibly shape-morphing sheets, with applications from stretchable electronics[167,168] to soft robotics[61–63].

Acknowledgements

This work is a testament to the importance of invention through play. Many thanks to Anika Jensenius, Oskar Jensenius, and Leonie Bisiot, for their discovery of the strange reshaping behaviour of groovy sheets during an errant craft project. Their findings brought forth this research.

We would like to thank Hadrien Bense, Lucie Domino, Théo Jules, Evgueni Filipov, Matthieu Labousse, Bas Overvelde and Albert Schenning for insightful discussions. We thank Klara Knupfer for seminal work on quantifying defect stability, and Daan van Velzen for developing a spin-coating method for corrugated rubber sheets. We are grateful to the precision manufacturing departments at AMOLF and Leiden University's Institute of Physics, especially Idsart Attema, Jan Verlinden, Marnix Verweij, and Mark Willemse, for developing and manufacturing the means to controllably thermoform plastic sheet material. We thank Dion Ursem and Jeroen Mesman-Vergeer for their ongoing technical support.